Department of Physics and Astronomy
University College London
University of London

Engineering the properties of magnetic molecules through the interaction with the surface

Ben Warner

Submitted in partial fulfilment of the requirements
for the degree of Doctor of Philosophy
at the University of London

July 2014

I declare that the work presented in this thesis is my own. Where information has been obtained from other sources, I declare this has been clearly indicated in the thesis.

Abstract

The drive to continue Moore's Law by shrinking electrical components down to the ultimate limit has led to a great deal of interest in atomic and molecular-scale electronics, in which individual atoms and molecules can be used as circuit elements. More recent proposals also seek to exploit the magnetic properties of these nanoscale objects in new applications in information technology and spintronics. In typical device geometries, the magnetic element is coupled to electrical leads, and these interactions can strongly affect the properties of the quantum system.

Using scanning tunneling microscopy and spectroscopy, we study the effects of interactions between individual magnetic atoms and molecules that are separated from an underlying metallic surface by a thin insulating layer of copper nitride (Cu_2N). By utilising the different growth phases of the Cu_2N, we show that the position of magnetic molecules can be controlled, and that the properties of a molecule can be controlled through the binding site.

For electrical transport through a junction containing an individual iron phthalocyanine (FePc) molecule on Cu_2N, we observe two novel magnetoresistance behaviours that arise from negative differential resistance (NDR) that shifts by unexpectedly large amounts in a magnetic field. Because voltage is dropped asymmetrically in this double barrier junction, the FePc can become transiently charged when its states are aligned with the Fermi energy of the Cu, resulting in the observed NDR effect. Furthermore, the asymmetric coupling magnifies the observed voltage sensitivity of the magnetic field dependence of the NDR, which inherently is on the scale of the Zeeman energy, by almost two orders of magnitude. These findings represent a new basis for making magnetoresistance devices at the single molecule scale. Furthermore, the enhancement of the energy scales created by asymmetric coupling of the junction can be used in conjunction with other multi-step tunnelling processes to allow for the investigation of phenomena that would otherwise be difficult to observe.

We also show that it is possible to interact with the f-shell magnetic moment when a bis(phthalocyaninato)Dy(III) complex ($DyPc_2$) is strongly coupled to the Cu(001) surface. $DyPc_2$ is a single molecule magnet, a type of molecule which may have applications in both spintronic and quantum computing applications. A Fano line

shape is observed at the Fermi energy, which is caused by the interference between tunnelling into the continuum and into a resonance created by the Kondo effect. By mapping the variance of the amplitude of the Fano line shape we are able to show that the ligand states create the continuum states and the 4f states create the Kondo resonance.

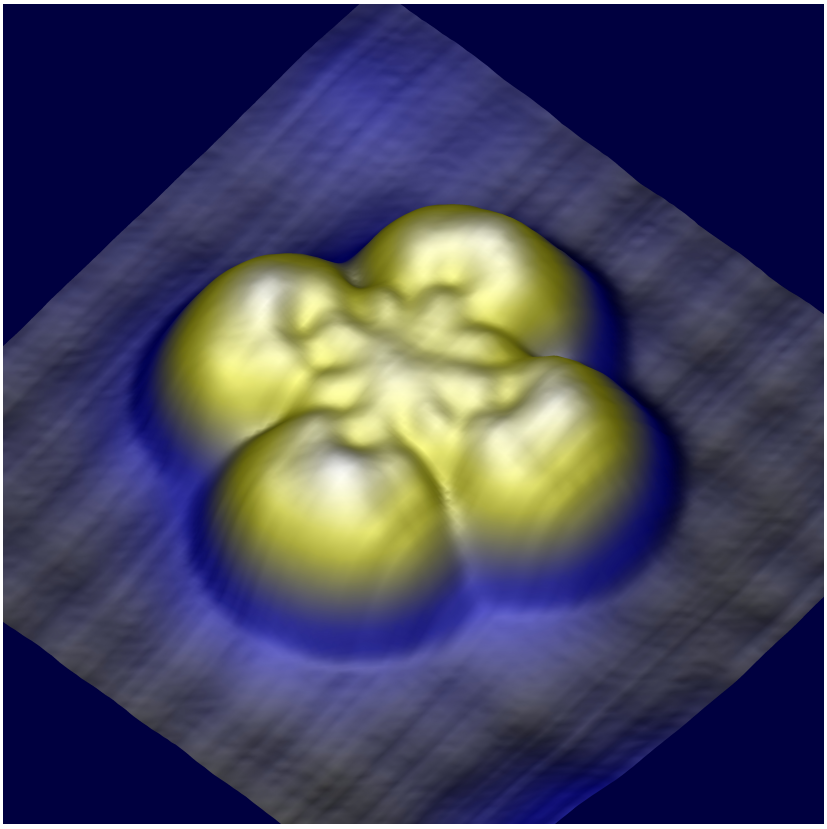

Acknowledgements

First and foremost, I would like to thank my advisor, Cyrus Hirjibehedin. I owe him a debt of gratitude for the skills his mentorship has developed.

This thesis is the end result of my fruitful partnership/friendship with Fadi. Though the work began with Fadi, without additional measurements with Henning, this thesis could have ended up on the bookshelf next to Grimms fairy tales. I am also thankful to Toby, Phil and Raz for their contributions to the analysis. I am indebted to Jenny, Reyes and all those already mentioned for their help fixing the STM. I would also like to thank my second supervisor, Andrew without his thoughtful advice, this thesis would be much poorer.

I am grateful to everyone in the STM group who have helped in various ways over the last five years : Steve, Neil, Phillip, Asif, Benjamin, Tingbin, Kitiphat, Adam, Manuel, Holly, Eric, Oscar and also the honorary, Kevin and Rob. I would also like to thank the groups I worked with from Berlin and Florence, these trips were amongst the highlights of my PhD.

That I have enjoyed the last years so much is mostly down to my friends. The friends I made throughout my Phd (inc. Team Southampton) have added greatly to my life. Whether teaching me to drink Coffee was a good idea, I thank all my LCN friends for making my PhD such an enjoyable experience.

Thanks to my Catz friends (Trev, Tom, Soph, Stote, Squire, Sena, Sab, Powell, Noddy, Magee, Manning, Leo, Kerry, Jdm, Greg, Deano, Bolton, plus Alan) who kept me happy when science was grey. I know the years ahead will create as many stories as the years gone by.

Finally I'd like to thank my family: Becki (I did try to get you into the science section), Marc (you made it), Carol for the shows, and my parents for their seemingly unlimited support. Thanks to my grandparents for the study centre over the years.

Contents

Chapter 1

Introduction

The flow of charge has been the driving force behind the industrialisation of the modern world. In the processors of modern computers, we are fast approaching the limits of current silicon based electronics both due to size-based physics and heat dissipation [1]. By utilising both the charge and spin of electrons, it may be possible to create a new device paradigm. This type of 'spintronic' device may allow for increased data processing speed and decreased electric power consumption as it follows the rules of quantum mechanics rather than those of classical physics [1].

The first generation of spintronic devices has been commercially realised through the giant magnetoresistance effect [1, 2]. Research aims to drive these devices down to the atomic scale, not only to replicate and produce smaller devices [3] but also to construct new devices based on effects that manifest on the atomic scale [4]. This would allow for increases in operating speed or data storage capacity [4]. Importantly, these devices might markedly reduce the heat costs involved in every data process, thereby vastly increasing energy efficiency. Currently 2% of global electricity is used in data centres; with this growing at a rate of approximately 12% annually, it is clear that devices of this type have both technological applications and potentially a significant environmental impact [5].

The local environment affects the properties of spins. This can be used to create advantageous properties or can be a hindrance, therefore controlling the local environment is of prime importance. One way this can be done repeatably is by in-

tegrating the spin into a molecule. This allows for the customisation of a repeatable local environment. However if a molecule is be used as an active component then it is likely that it will be necessary to place the molecules on a surface. For this reason it is essential to study how the surface interacts with and affects the properties of the molecule.

The electronic and magnetic properties of a single molecule can be studied using a scanning tunnelling microscope (STM). This device, for which the Nobel prize was awarded in 1986, allows for both the imaging of a surface at the atomic level and taking of spectroscopic data. This thesis concentrates on how STM measurements allow for an investigation of the properties of single magnetic molecules on surfaces and how the surface can be used to modify the properties of the molecule.

Chapter 2 of this thesis discusses the concept of how magnetic anisotropy arises from the effect of the local environment or from the orbital properties of the ion. Factors which affect the energy levels of the magnetic moment are discussed along with the differences between 3d and 4f magnetic ions.

There are three main techniques that have the capability to measure the properties of a single molecule: STM, XMCD and charge transport through nanoscale junctions. Each of these is introduced in Chap 3. The instruments on which the data was taken are discussed in Chap 4 and the preparation of the samples in Chap 5.

Chapter 6 includes an introduction to the phthalocyanine molecules studied in this thesis and a discussion of how Cu_2N can be used as a nanoscale template for controlling the adsorption of magnetic molecules on a surface. In Chap 7 it is shown that the magnetic properties of FePc are defined by the binding site of the central metal atom when the molecule is placed on a Cu_2N monolayer. This chapter also acts as a background for Chap 8 which describes an NDR effect observed for FePc on Cu_2N. This NDR effect is seen to shift with magnetic field by two orders of magnitude above the Zeeman effect.

In Chap 9, we investigate a single molecule magnet that has a single lanthanide atom at the centre. Here a Kondo effect is observed from the interaction with the 4f states of the lanthanide atom with the conduction electrons in the metal surface.

The thesis ends with a brief conclusion and a discussion on how this research could be expanded to investigate new areas.

Chapter 2

Magnetism

2.1 Introduction

The magnetic properties of an atom are set by its orbital properties and its interaction with the surrounding environment. Understanding how these combine to create the magnetic properties of an atom is important if we are to understand the effect of the interaction with the surface on molecules. Therefore in this chapter we discuss the simple rules which can be used to describe the magnetic properties of the atom. Next we discuss how magnetism created by 4f and 3d ions differs, and how these differences can be utilised in single molecule magnets. Then the spin Hamiltonian model is introduced which has been shown to be a good model for measurements of single atoms and molecules on a surface [6–8]. Finally we introduce the Kondo effect, which occurs when a magnetic moment interacts with the conduction electrons in a metal.

2.2 Hund's rules

The magnetic properties of an atom can be estimated via the use of Hund's rules. By utilising the rules, the energy of the system is minimised and therefore the ground state can be determined.

Rule 1: **S** is maximal

This minimises the coulomb repulsion between electrons, as the Pauli exclusion principle stops electrons with the same spin state sharing the same orbital.

Rule 2: **L** is maximal
This minimises the overall energy, as electrons in orbits rotating in the same direction optimally avoid each other, reducing the coulomb repulsion.

Rule 3:
J=|L-S| is minimal, for $n \leq 2l + 1$
J=L+S is maximal, for $n > 2l + 1$
This rule minimises the spin orbit interaction of the system. When the shell is less than half filled the total energy is minimised by the antiparallel alignment of the spin and orbital momentum. When the shell is more than half full, the energy is minimised by the parallel alignment of the spin and orbital momentum.

Examples

The rare earth ion, Dy^{3+} has a total of 9 electrons in its outer shell. f-shell states have $L = 3$, therefore there are 7 levels $(\pm 3, \pm 2, \pm 1, 0)$. To satisfy the first rule we need the maximum spin, therefore $S = \frac{5}{2}$ as there are 7 spin up and 2 spin down $(7 \times \frac{1}{2} - 2 \times \frac{1}{2})$. For the second rule it is necessary to maximise the value of L. Only the spin down electrons contribute and therefore $L = 3 + 2$. Finally as the shell of the Dy ion is greater than half full, $J = L + S$, therefore $J = 5 + \frac{5}{2} = \frac{15}{2}$.

In the case of Fe^{2+}, there are 6 electrons in the outer d shell, and therefore $S = 2$ as we have 5 spin up and 1 spin down. This results in a value of $L = 2$ and as the shell is more than half filled $J = 4$. However these rules are only estimates of the contribution of the various factors, and therefore when interactions with external factors occur, such as crystal field splitting, the ground state and spin of the system may change. In some cases this can be done reversibly [9].

2.3 3d and 4f magnetism

Studies of magnetism have concentrated on two types of ions, the 3d and 4f ions. The 3d ions are the first transition metals in the periodic table and include such well

known elements as iron, copper and zinc. The 4f ions are known as the lanthanides or 'rare earth' metals; though this name is somewhat of a misnomer given that cerium has an abundance similar to copper. The rare earth materials are utilised in many modern technologies, such as lasers, computer memory and batteries [10].

The uses of both these groups is inherently connected to the distance dependence and nature of the orbitals [11]. 4f orbitals are highly asymmetrical in shape, this results in them having an inherent anisotropy [11]. In Fig 2.1, the radial wave functions for Ce and Tm are shown [11]. 4f orbitals are tightly confined to the atom, resulting in them being shielded from the surroundings by the 6s and 5d states. The effect of this is that the crystal field splitting term in the Hamiltonian is small compared with the spin-orbit term and therefore the magnetic moment is defined by J [11]. Lanthanides mainly form +3 ions; this allows for different lanthanides to be switched in a material without greatly affecting the chemical properties.

In Fig 2.1, the Tm (Z=69) 4f orbitals are more tightly confined than those of Ce (Z=58). This contraction of the 4f orbitals as the lanthanide elements get heavier is caused by incomplete screening of the nuclear charge [11].

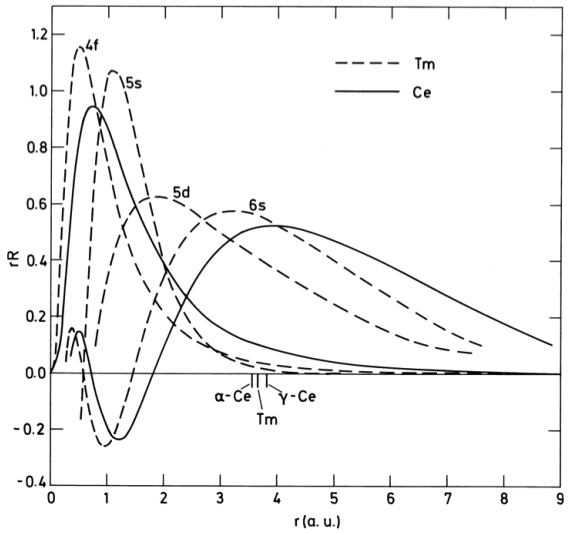

Figure 2.1: Radial component of atomic wave function for Ce and Tm. The 4f orbital is confined close to the atom, which reduces it's interaction with the surrounding environment [11].

3d orbitals are not as tightly confined as the 4f states and therefore interact with the surrounding environment to a greater degree. This results in the crystal field

splitting term being larger than the spin orbit term. Therefore the ground state of the ion is the one where L=0, rather than obeying Hund's third rule; this effect is called 'orbital quenching'. The magnetism of these systems can therefore be described by the spin Hamiltonian model featured later in this chapter. From this we can see that although a 3d ion in free space has no anisotropy, by controlling the crystal field splitting it is possible to create large anisotropies.

2.3.1 Single Molecule Magnets

An example where the anisotropy of an ion is exploited is in a single molecule magnet (SMM) [12]. A SMM is a molecule in which an excited spin relaxes slowly back to the ground state. These molecule may have applications in spintronics as well as quantum computing [4, 13].

For slow relaxation to occur the magnetic moment must have an easy axis anisotropy, i.e. the ground state is the high spin state. This is because although the ground state is degenerate, due to selection rules it is not possible for the spin to flip directly between the positive and negative high $\mid m_s\rangle$ spin states. This creates an energy barrier to the spin flip occurring. The size of this energy barrier is defined by the anisotropy of the system [12].

Initially work on SMMs concentrated on molecular transition metal compounds, such as the prototypical SMM Mn-12 [14]. Here a large barrier is created through a large number of interacting transition metal atoms experiencing an anisotropic crystal field effect. This can be modelled, using the giant spin approximation as a single spin S=10. In this way the ability to use the local environment to create magnetic anisotropy in a 3d system is exploited. The size of the barrier is given by $U = |D|S^2$ where D is the size of the axial anisotropy and S the total spin [12]. Initially efforts were directed towards maximising S. However calculations show that this approach is inherently limited by the link between S and D, in which D is shown to be inversely proportional to S^2 [15].

To create SMMs with longer spin relaxation times, work began to concentrate on maximising D, the anisotropy of the system. As 4f orbitals are inherently highly anisotropic [11], investigations began to look at molecules which contained lanthanide metals [16]. These molecules were seen to have longer spin relaxation times

than those based on transition metals [16, 17].

Scanning tunnelling microscopy studies of single molecule magnets were initially limited by the difficulty of placing the large molecules such as Mn-12 onto the surface cleanly, as it was found that these molecules break up when thermally sublimed. In recent work by Kahle et al., Mn-12 was placed onto the surface using a mass spectrometer allowing for STM studies of its magnetic properties [18]. It has also been placed on the surface through using a STM tip to transfer molecules [19]. Investigations of Ln-Pc_2 molecules are considerably easier as these molecules are stable when thermally sublimed [20].

2.4 Magnetic Interactions

In this section we will briefly introduce the spin Hamiltonian model. This will allow for an understanding of the effects that modify the energy levels of an isolated magnetic moment.

2.4.1 Spin matrices

The spin operator can be described by a spin matrix [21]. Acting S_z on the wave function gives the eigenvalues of S_z, m.

$$S_z|\Psi>=\hbar m|\Psi> \tag{2.1}$$

The operator S_z is therefore a matrix of dimensions equal to $2s+1$ with the values of m across the diagonal. Therefore for spin $\frac{1}{2}$ we get

$$S_z = \frac{1}{2}\begin{pmatrix} 1 & 0 \\ 0 & -1 \end{pmatrix} = \frac{1}{2}\sigma_z$$

We can get S_y and S_x by using the commutator relationships.

$$[S_x, S_y] = i\hbar S_z$$

$$[S_y, S_z] = i\hbar S_x$$

$$[S_z, S_x] = i\hbar S_y$$

This gives

$$S_x = \frac{1}{2}\begin{pmatrix} 0 & 1 \\ 1 & 0 \end{pmatrix} = \frac{1}{2}\sigma_x$$

$$S_y = \frac{1}{2}\begin{pmatrix} 0 & -i \\ i & 0 \end{pmatrix} = \frac{1}{2}\sigma_y$$

$\sigma_x, \sigma_y, \sigma_z$, are the Pauli matrices.

The spin matrices for S=1 are given as [21].

$$S_x = \begin{pmatrix} 0 & 1 & 0 \\ 1 & 0 & 1 \\ 0 & 1 & 0 \end{pmatrix}$$

$$S_y = \begin{pmatrix} 0 & -i & 0 \\ i & 0 & -i \\ 0 & i & 0 \end{pmatrix}$$

$$S_z = \begin{pmatrix} 1 & 0 & 0 \\ 0 & 0 & 0 \\ 0 & 0 & -1 \end{pmatrix}$$

The spin Hamiltonian model assumes that the orbital angular momentum terms are small. This is often true for transitional metals due to orbital quenching; however for 4f orbitals the angular momentum term is non-negligible [11, 22]. A magnetic centre with n unpaired electrons has a spin, $S = \frac{n}{2}$. It will have $2S + 1$ levels associated with this multiplet. The levels of the magnetic moment will split due to various effects. The interactions modelled in the spin Hamiltonian are the Zeeman effect, the crystal field effect and the exchange interaction. Only if these are the

dominant interactions is it possible to model the system using the spin Hamilton method.

2.4.2 Zeeman Effect

The Zeeman effect is the name given to the splitting of degenerate energy levels due to the interaction of the magnetic field with the spin moments. The splitting of the levels grow linearly as the magnetic field increases [12]. An energy diagram of this is shown in Fig 2.2. The splitting is given by,

$$\mathcal{H}_{ZE} = g\mu_B m_s B \tag{2.2}$$

where g is the electron spin g-factor, $\mu_B = 5.788 \times 10^{-2}$meV/T is the Bohr magneton, B the magnetic field and S the total spin of the atom. Knowledge of the energy of transitions between energy levels allows for g to be calculated. This is important as the g factor gives a picture of the chemical environment that the electron sees. Although g is a tensor, here we consider g to be a scalar quantity for simplicity.

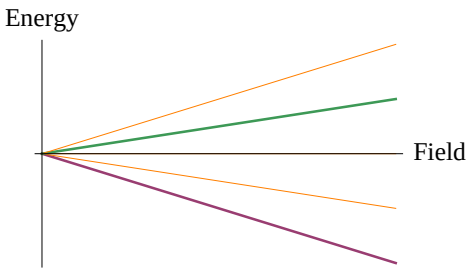

Figure 2.2: Zeeman splitting for a free atom, spin 2.

2.4.3 Crystal field effect

The crystal field effect effect arises from the splitting of spin levels by the electric field of neighbouring ions. As the d-orbitals have different angular distributions, orbitals which come close to the ions are repulsed and have a higher energy. Therefore the crystal field splits the degeneracy of the d-orbitals. Due to the spin-orbit coupling these changes affect the magnetic moment.

In the spin Hamiltonian method the complex behaviour is simplified into two terms, D and E [12]. The Hamiltonian of the crystal field effect can be approximated to be the quadratic form of the spin operators $H_{CF} = S.D.S$, where D is a real, symmetric tensor. By choosing the coordinate axes to be parallel with the eigenvectors of D, D is diagonal and therefore is given by

$$\mathcal{H}_{CF} = D_{xx}S_x^2 + D_{yy}S_y^2 + D_{zz}S_z^2 \tag{2.3}$$

Here S_x, S_y, S_z describe the spin in each axis direction. This equation can be simplified by using the property of Hamiltonians that adding or subtracting a constant has no effect. Therefore by subtracting the constant $(D_{xx} + D_{yy})(S_x^2 + S_y^2 + S_z^2) = \frac{1}{2}(D_{xx} + D_{yy})S(S+1)$ we obtain

$$\mathcal{H}_{CF} = DS_z^2 + E(S_x^2 - S_y^2) \tag{2.4}$$

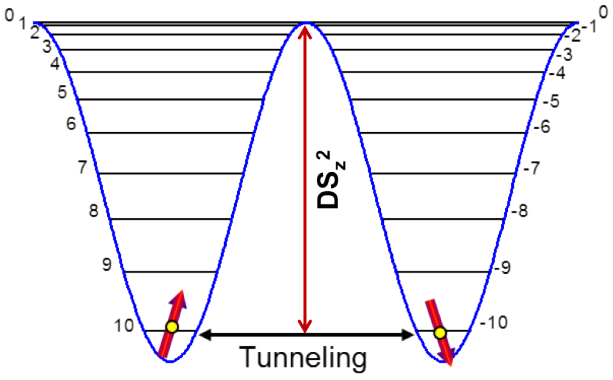

Figure 2.3: The double well potential of a S=10, D < 0, E=0 magnetic moment [12].

In this formula $D = D_{zz} - \frac{1}{2}(D_{xx} + D_{yy})$ and $E = D_{xx} - D_{yy}$. The D and E terms are important in our study of magnetic molecules. A double well of a $S = 10$, D < 0, $E = 0$ is shown in Fig 2.3. The double well is created from the S_z^2 term. Due to selection rules it is not possible to switch from $m_s = 10$ to $m_s = -10$ without going over the barrier, or tunnelling through the barrier [12]. The height of this barrier is described by the D term. The E term describes the mixing of the states; the mixing of states allows for the quantum 'tunnelling' through the barrier. For $D > 0$ the lowest absolute value of $|\, m_s\rangle$ forms the ground state. Therefore the z

component of the magnetic moment is minimised and so the spin aligns orthogonal to the principal symmetry axis; this is hard axis anisotropy. This situation is shown in Fig 2.4 a. For $D < 0$ the highest absolute value of $\mid m_s\rangle$ forms the ground state. The spin aligns along the principal symmetry axis and we have easy axis anisotropy. If the D term is negative then the highest $\mid m_s\rangle$ is the ground state. The means that although the ground state is energetically degenerate, selection rules stop the spin from flipping from positive to negative $\mid m_s\rangle$. This creates an energy barrier, and a bistable spin.

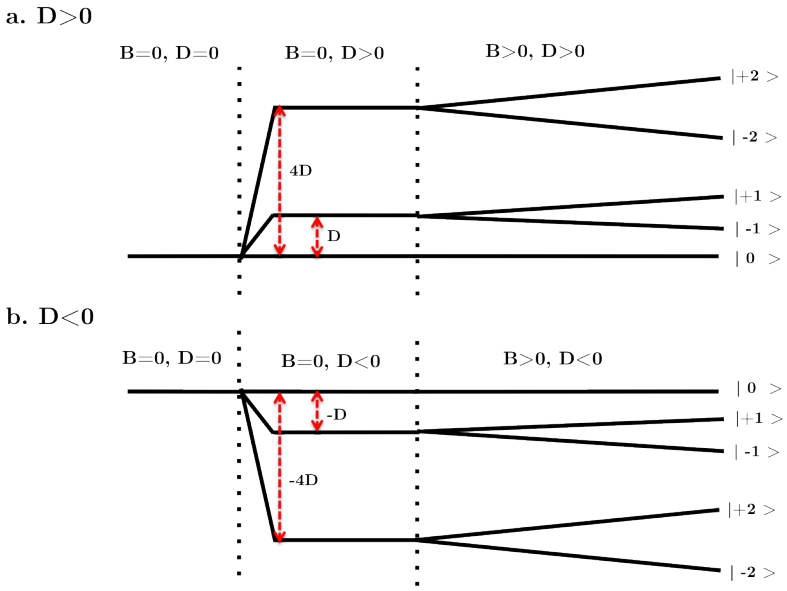

Figure 2.4: Splitting of an atom with spin 2 in a crystal field with axial symmetry. a) shows the case for $D > 0$, hard axis anisotropy. b) shows the case for $D < 0$, easy axis anisotropy.

2.4.4 Dipole interaction

The dipole interaction describes the strength of interaction between two magnetic moments through their magnetic field [23]. The energy of two magnetic moments separated by a distance R is given by

$$E = \frac{\mu_0}{4\pi r^3}[\vec{m_1}.\vec{m_2} - \frac{3}{r^2}(\vec{m_1}.\vec{r})(\vec{m_2}.\vec{r})] \tag{2.5}$$

Therefore the approximate magnitude of this interaction is given by

$$E = \frac{\mu_0}{4\pi} \frac{[\vec{m_1}.\vec{m_2}]}{R^3} \tag{2.6}$$

By setting $\vec{m_1} = \vec{m_2} = \mu_B$ and $R = da_B$, where $a_B \simeq 0.5$Å is the Bohr radius, we get

$$E = \frac{\mu_0.\mu_B^2}{\pi.d^3 a_B^3} \tag{2.7}$$

In CGS units this gives

$$E = \frac{\alpha^2 e^2}{d^3 a_B} \tag{2.8}$$

where $\alpha = \frac{e^2}{\hbar c}$

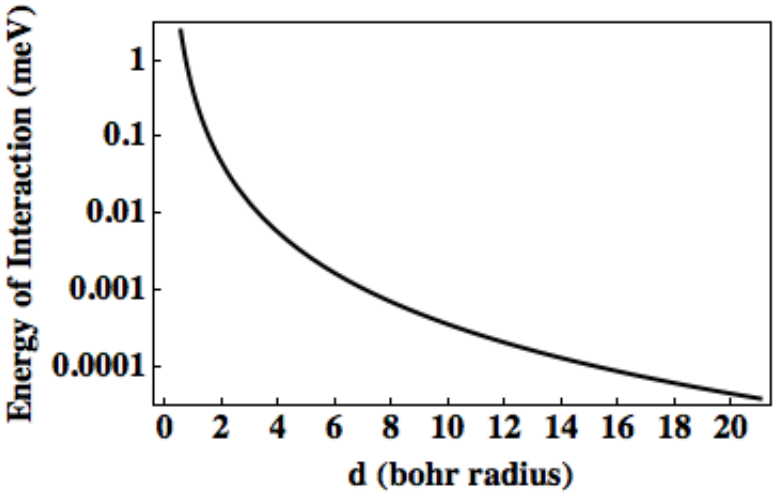

Figure 2.5: The Dipole interaction energy quickly drops off with distance.

Figure 2.5 shows how the energy of the dipole interaction drops off with distance. For two atoms sitting 1nm apart this gives a value for the energy interaction of approximately 0.01K.

2.4.5 Exchange interaction

The exchange interaction term describes the interaction between two spins. The effect originates from the Pauli exclusion principle; this states that no two particles can share the same state. As electrons are fermions they must have an antisymmetric wave function.

Two cases can occur. The spins can align and the spatial wave function is antisymmetric or the spins can be antiparallel and the wave function is symmetric. If the wave function is antisymmetric the electrons will have the same spin state and the electrons will be farther apart on average. This creates a ferromagnetic interaction, this situation is favoured if the two spins on the same atom as the repulsion energy is reduced as the electrons are further apart.

If the electrons are on different atoms, then the opposite case can occur. Here the wave function is symmetric and the spins are anti-aligned. This situation creates an anti-ferromagnet interaction. In the case of two atoms it is energetically favourable to form molecular orbitals across the two atoms, and a consequence of this is that spatially symmetric 'bonding' orbitals are at a lower energy, rather 'anitibonding' orbitals which are spatially asymmetric, due to the difference in the radius of curvature and hence kinetic energy.

The exchange interaction term therefore determines the energy of each state. An exact calculation of this effect is complex due the many body physics involved including the interaction of the electrons with the nuclei in addition to their interaction with each other. An approximation can be calculated by using the Heisenberg Hamiltonian [12],

$$\mathcal{H}_{Ex} = \frac{1}{2}\sum_{i,j} J_{ij}.S_i.S_j \tag{2.9}$$

where S_i is the total spin of all electrons bound to the atom i, S_j for atom j and J_{ij} is the spin coupling constant given by the formula.

$$J_{ij} = \int \phi_i^*(r_1)\phi_j^*(r_2)\frac{e^2}{|r_1 - r_2|}\phi_i(r_2)\phi(r_1)dr_1dr_2 \tag{2.10}$$

In this equation ϕ_i and ϕ_j are the wave functions of the respective electrons and r_1 and r_2 the position of each electron.

The actual coupling between electrons can occur in a variety of ways. Direct coupling is the process in which the electron orbitals overlap. Superexchange is when a non-magnetic atom acts as a link between the two magnetic spins. Finally Ruderman-Kittel-Kasuya-Yosida (RKKY) coupling occurs when the coupling occurs via two magnetic localised spins linked by conduction electrons in a metal [12].

2.5 Kondo Effect

The resistance of a metal at room temperature is dominated by electron-phonon scattering [24]. As the temperature is reduced the scattering drops and the resistance drops; in most cases this continues till the resistance saturates at a constant value, which is mainly set by impurities and structural defects [24]. However since the 1930s it has been seen that in some metals a rise in resistance occurs at low temperatures, as seen in Fig 2.6a. This was observed to be due to magnetic impurities present in the metal interacting with the conduction electrons.

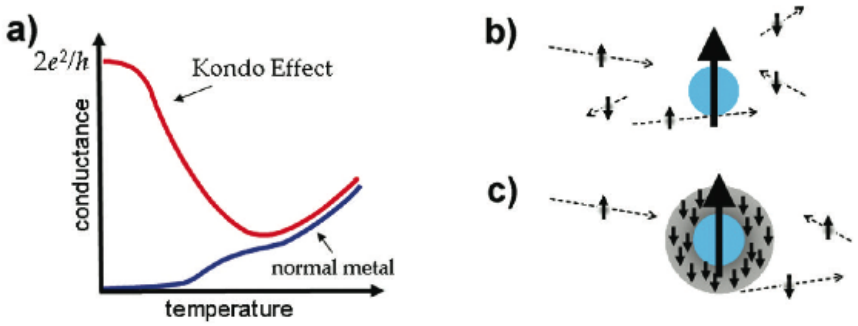

Figure 2.6: a) Conductance in a metal for which the Kondo effect is observed and for which it is not. b) Above the Kondo temperature the magnetic impurity is unscreened. c) Below the Kondo temperature the conduction electrons screen the junction [24].

In 1964 Kondo showed that this effect was due to the increase in effective scattering cross section of magnetic impurities [25]. Above the Kondo temperature the magnetic impurity is unscreened (Fig 2.6b). Below the Kondo temperature, a cloud of conduction electrons collectively screen the magnetic moment increasing its cross

section, as seen in Fig 2.6c. This increases the scattering and the resistance [24]. As temperature decreases the resistance increases as an electron in the Kondo screening cloud is less likely to be inelastically scattered by a conduction electron [43].

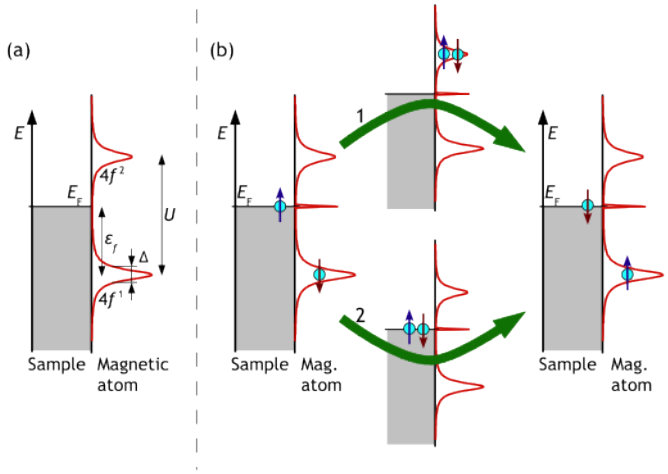

Figure 2.7: a) Anderson model is of a magnetic impurity with one 4f orbital, this can be single singularly occupied $4f^1$ or double occupied $4f^2$. b) The spin of the 4f orbital can be flipped via two processes, either the orbital is emptied then refilled or double occupied and then one decays back. These processes result in the Kondo resonance at the Fermi energy [26].

The Anderson model provides a physical picture of what is occurring [26]. The Anderson model describes a single magnetic impurity embedded in a non-magnetic metal. The magnetic impurity is assumed to have a single orbital, for example a 4f orbital. This orbital can be occupied by zero, one or two electrons. The schematic is shown in Fig 2.7 [26].

The singularly occupied state $4f^1$ has an energy ϵ_f below the Fermi energy, with the doubled occupied orbital $4f^2$ at an energy U above the $4f^1$ state, where U is the Coulomb repulsion between the two electrons. Due to the hybridisation with the magnetic orbital and the host metal the orbitals are broadened by Δ.

Spin exchange processes can occur in two ways, as detailed in Fig 2.7b. One way is for the electron residing in $4f^1$ orbital to jump to the host and then another electron jump into the $4f^1$ orbital. The second process is for an electron to jump into the $4f^2$ state and then one of the electron to jump out to the host. In both these processes there is no reason for the original spin state of the $4f^1$ orbital to be maintained and therefore this allows for a spin flip to occur. It is classically forbidden to remove

an electron from the orbital, or to add an electron to the orbital. However the uncertainty principle allows for these processes to occur as a virtual process on a timescale of $\frac{h}{|\epsilon_f|}$. Due to these processes occurring the energy spectrum is modified. When many of these processes occur, a new ground state results near the Fermi energy which is called the 'Kondo resonance' [26].

Chapter 3

Measuring magnetic moments at the nanoscale

3.1 Introduction

The study of single magnetic moments is of importance not simply for the interesting fundamental science but also for technological applications [27,28]. Studying a single moment requires very sensitive techniques. In this chapter we describe three of the most used techniques for investigating single atomic moments: STM, XMCD and nanoscale junctions. In this thesis both XMCD and STM have been utilised to gain insight on the influence of absorption on the surface, and both the techniques and relevant literature are discussed in this chapter. A brief description of nanoscale junctions is included for completeness.

3.2 Scanning tunnelling microscope

The scanning tunnelling microscope (STM) has allowed for the investigation of the properties of individual atoms and molecules on a surface. Its capability to measure both the topography and the local density of states allows for measurements of individual molecules and their local area. For a thorough review of STM see reference [29] and for the description of the mathematical theory see reference [30].

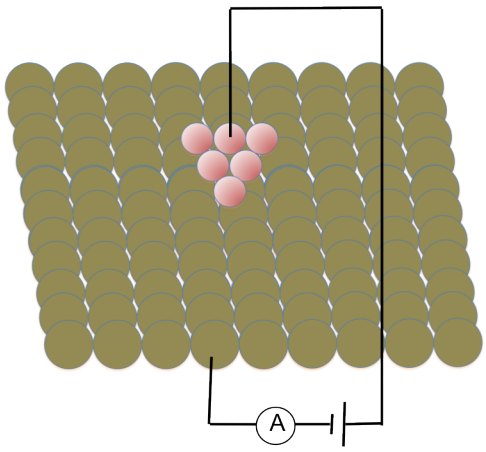

Figure 3.1: An illustration of an STM junction. The tip, shown in pink, is placed $<$ 1nm from the sample, and a voltage is applied between the tip and sample. By measuring the resulting tunnel current, the surface topography can be studied.

An STM can be modelled as a junction between a tip and a sample, with voltage placed across it. In Figure 3.1 the tip, represented by the pink 'atoms', is placed close to the surface and the current from electrons tunnelling across the junction is measured. By measuring the current and raster scanning the tip across the surface it is possible to build up an image of the surface.

Most measurements taken in an STM utilise elastic tunnelling. In this case, electrons tunnel across the junction without losing any energy; this is dealt with in section 3.2.1. In section 3.2.3 we will discuss inelastic tunnelling, where electrons lose energy during the tunnelling process, and the extra information that this provides.

3.2.1 Elastic Tunnelling

We can model an STM as a 1D barrier with energy U, as shown in figure 3.2 [29]. The tunnelling current decay can then be explained by solving the time independent Schrodinger equation

$$-\frac{\hbar^2}{2m}\frac{d^2\psi(z)}{dz^2} + U(z) = E\psi(z) \tag{3.1}$$

where $U = U_0$ and $U_0 < E$, the solution of Eq. 3.1 is

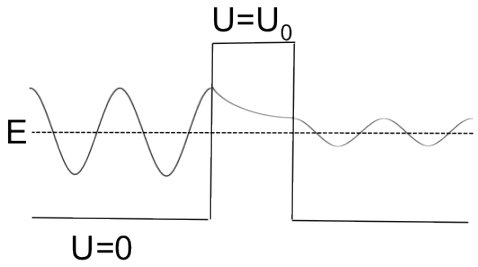

Figure 3.2: An electron with energy E can tunnel through a barrier with energy U_0 due to the wave function being non-zero on the other side of the barrier.

$$\psi(z) = \psi(0)e^{\pm ikz} \tag{3.2}$$

$$k = \frac{\sqrt{2m(E - U_0)}}{\hbar}$$

when $U = U_0$ and $U_0 > 0$, the solution of Eq. 3.1 is

$$\psi(z) = \psi(0)e^{-kz} \tag{3.3}$$

$$k = \frac{\sqrt{2m(U_0 - E)}}{\hbar}$$

There is a second solution, $\psi(z) = \psi(0)e^{kz}$, which describes electrons tunnelling in the opposite direction. The probability density of an electron penetrating across the barrier from left to right is given by

$$|\psi(z)|^2 \propto |\psi(0)|^2 e^{-2kz} \tag{3.4}$$

Using the work function of the metal as our reference point we can define the Fermi energy of the system, $E_F = -\phi$. In order for there to be a net tunnelling current it is necessary to bias one side of the junction with a voltage, V. However we will make the assumption that $eV << \phi$ as this means that the states that are important have an energy approximately equal to the Fermi level. The transmission coefficient describes the ratio of the intensity of the transmitted wave to that of the incident

Work Function of Metals	
Element	ϕ(eV)
Al	4.1
Au	5.4
Cu	4.6
Ir	5.6
Ni	5.2
Pt	5.7
Si	4.8
W	4.8

Table 3.1: A table showing the work functions of materials commonly used in STM experiments [29].

wave :

$$P(z) \equiv \frac{I(z)}{I(0)} = e^{-2kz} \tag{3.5}$$

$$k = \frac{\sqrt{2m(\phi_{avg})}}{\hbar}$$

where

$$\phi_{avg} = \frac{\phi_{tip} + \phi_{sample}}{2}$$

ϕ_t is the work function of the tip and ϕ_s is the work function of the sample. By taking an average of the these two values we get an approximation of the barrier height. For copper, $\phi = 4.6$eV, and therefore $k = 10.9\text{nm}^{-1}$ [29]. This results in the tunnelling current decaying by an order of magnitude for every 1Å increase in the distance between the tip and the sample [29]. It is due to this large change in current that the topography of the surface can be measured down to atomic length scales.

It is possible to calculate the total current across the junction. In this study we will, for reasons of simplicity, assume the tip and the sample are the same ideal, one dimensional metal. The junction we are describing is shown in the Fig 3.3a. Here the convention has been used that a positive voltage V_T applied to the sample with

respect to the tip causes particles with positive charge to tunnel from the sample to the tip.

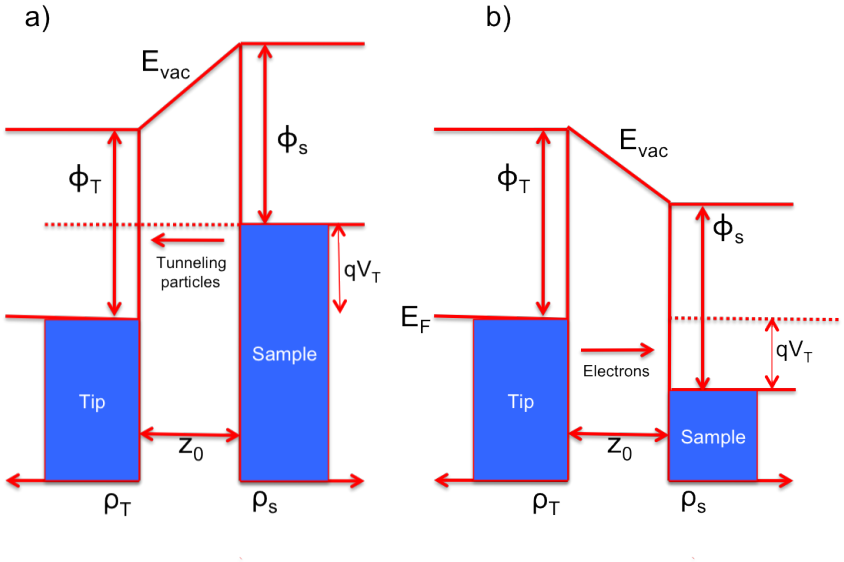

Figure 3.3: A tunnelling junction at T=0K. In both panels a positive bias has been applied to the sample; ρ_t and ρ_s refer to the local density of states in the tip and sample respectively; E_F is the Fermi energy; and ϕ_t and ϕ_s are the work functions of the tip and sample respectively; E_{vac} is the energy necessary to ionise the electrons. Panel a) corresponds to particles with a positive charge ($q > 0$) so the sample is at a higher potential than the tip. This means that the particles tunnel from the sample to the tip. Panel b) is for electrons, where q is negative, the sample is at a lower energy than the tip as qV_T is negative. This means that, for the convention of positive sample bias, electrons tunnel from the tip to the sample.

A point worthy of further discussion is that of negatively charged particles (e.g. electrons). The charge, q, is negative and therefore the physical picture is now that of Fig 3.3b. Due to q being negative, qV_T has a negative value and the Fermi level of the sample is below that of the tip. This means that the electrons tunnel from the tip to the sample. Throughout this discussion we will use the convention that q is positive unless explicitly stated.

To calculate the current across the junction it is necessary to first calculate the rate at which a single particle will tunnel through the barrier. The system's Hamiltonian, H, can be broken down into the time independent part H_0 and the time dependent part δH. As per perturbation theory, by assuming the time dependent part only results in small perturbations, we can assume that the eigenstates of H are the same

as H_0 [21]. We then calculate the probability at which a system in state ψ_a at time $\tau = t_0$ and energy = E_a will be in state ψ_b at time $\tau = t$ with energy = E_b. The final result, if t is assumed to be long [29], is given by Fermi's golden rule which gives the rate of transition from state a to state b as,

$$W_{ba} = \frac{2\pi}{\hbar}|M_{ba}|^2\delta(E_a - E_b) \tag{3.6}$$

Here the matrix element is given by $M_{ba} = \langle\psi_b \mid \delta H \mid \psi_a\rangle$. By using dimensional analysis it can be confirmed that the units of Fermi's golden rule are s^{-1}, a rate. In Fermi's golden rule the Dirac delta function maintains energy conservation.

Moving back to our simplified model of the STM junction, our initial state is that shown in Fig 3.3a. The final state is when a particle has transitioned across the junction. A particle can only tunnel from a filled state to a empty state; thus at $T = 0$K, and for $q > 0$, particles can only tunnel from the sample to the tip. However the simplification to $T = 0$K is unnecessary, and hides features that are important. Figure 3.4 shows the Fermi function for a positive sample bias at $T = 0$K and $T > 0$K. From Fig 3.4 we can see that for T> 0K it is possible for particles to transition both from the sample to the tip and the tip to the sample.

From Fermi's golden rule we can calculate the total rate of transitions from state a to state b and therefore the current. In the tunnelling junction we have two sets of transitions, one from the filled states in the sample to the empty states in the tip and one from the filled states in the tip to the empty states in the sample, as long as $T > 0$K. The total current is given by the difference between the two currents. For simplicity we will first calculate the current due to tunnelling from the sample to the tip.

Fermi's golden rule gives us the rate of transition for a particle with a specific energy and in a specific state. In order to calculate the current from the sample to the tip we must calculate the rate of transition from the sample to the tip for every possible energy and for every possible state.

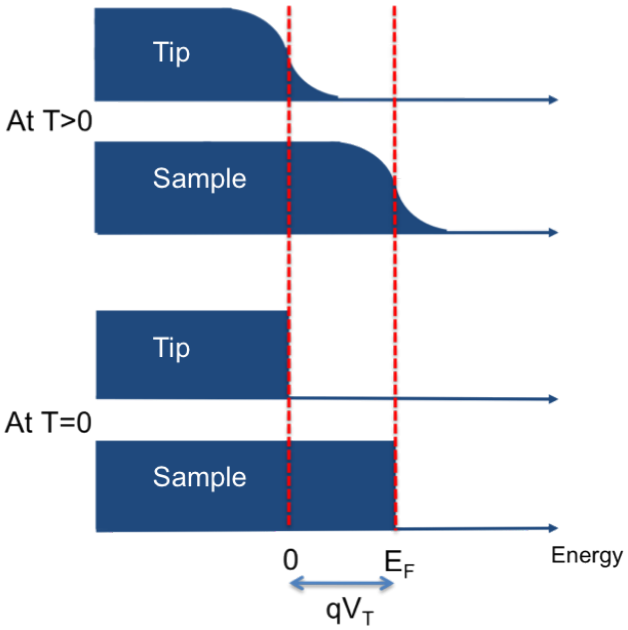

Figure 3.4: A junction at $T = 0$K and $T > 0$K. The effect of temperature can be seen on the Fermi surfaces. From the diagram it can be seen how at $T > 0$K there can be tunnelling both from the sample to the tip and from tip to the sample whereas at $T = 0$K tunnelling can only occur in one direction.

$$W_{s\to t} = \frac{(2)2\pi}{\hbar}\int_{-\infty}^{\infty} dE_t \int_{-\infty}^{\infty} dE_s \; f(E_s)(1-f(E_t))\rho_t(E_t)\rho_s(E_s)|M_{ts}|^2\delta(E_s-E_t+qV_T) \tag{3.7}$$

Here ρ_t and ρ_s, are the density of states of the tip and sample respectively, and $f(E) = 1/(e^{E/k_BT}+1)$ is the Fermi-Dirac distribution. The additional factor of 2 comes from electrons having two spin states, and therefore each level can hold two electrons without breaking Pauli's exclusion principle.

The next step is to integrate through by one of the energies. This results in the Dirac delta factor disappearing and a factor of $+qV_T$ moving into the density of states for the tip, and the Fermi Dirac function that describes the states in the tip. As a particle tunnelling from the sample at energy E must conserve energy, the sample is $+qV_T$ in energy above the the tip and therefore the electron will tunnel into the state $E + qV_T$ in the tip.

$$W_{s\to t} = \frac{4\pi}{\hbar}\int_{-\infty}^{\infty} dE\ f(E)(1-f(E+qV_T))\rho_t(E+qV_T)\rho_s(E)|M_{ts}|^2 \tag{3.8}$$

The current is simply the rate of transition multiplied by the charge,

$$I_{s\to t} = \frac{4\pi q}{\hbar}\int_{-\infty}^{\infty} dE\ f(E)(1-f(E+qV_T))\rho_t(E+qV_T)\rho_s(E)|M_{ts}|^2 \tag{3.9}$$

Equation 3.9 is the current caused by positive particles tunnelling across the barrier from the sample to the tip.

If we now consider electrons we must remember that the tip is higher in energy than the sample as the bias applied to the sample is $-eV_T$. Therefore an electron tunnelling out of the sample at energy E will tunnel into the state $E - eV_T$ in the tip. The only consequence of the change from positive charge to electrons is that the direction of tunnelling that contributes the majority of current switches. Equation 3.10 shows the current from the sample to tip for electrons.

$$I_{s\to t} = \frac{-4\pi e}{\hbar}\int_{-\infty}^{\infty} dE\ f(E)(1-f(E-eV_T))\rho_t(E-eV_T)\rho_s(E)|M_{ts}|^2 \tag{3.10}$$

The current from the tip to the sample can be calculated in the same way; the steps are shown below for completeness again with positive charge.

$$W_{t\to s}^{total} = \frac{(2)2\pi}{\hbar}\int_{-\infty}^{\infty} dE_t \int_{-\infty}^{\infty} dE_s\ f(E_t)(1-f(E_s))\rho_t(E_t)\rho_s(E_s)|M_{ts}|^2\delta(E_t-(E_s+qV_T))$$

$$= \frac{4\pi}{\hbar}\int_{-\infty}^{\infty} dE\ f(E+qV_T)(1-f(E))\rho_t(E+qV_T)\rho_s(E)|M_{ts}|^2 \tag{3.11}$$

$$I_{t\to s} = \frac{4\pi q}{\hbar}\int_{-\infty}^{\infty} dE\ f(E+qV_T)(1-f(E))\rho_t(E+qV_T)\rho_s(E)|M_{ts}|^2 \tag{3.12}$$

The total current is given by $I_T = I_{s\to t} - I_{t\to s}$:

$$I_T = \frac{4\pi q}{\hbar}\int_{-\infty}^{\infty}[f(E)(1-f(E+qV_T))-f(E+qV_T)(1-f(E))]\rho_t(E+qV_T)\rho_s(E)|M_{ts}|^2dE \tag{3.13}$$

We can now simplify this further through simple algebra

$$\begin{aligned} & f(E)(1-f(E+qV_T))-f(E+qV_T)(1-f(E)) \\ &= f(E)+f(E)f(E+qV_T)-f(E+qV_T)-f(E+qV_T)f(E) \\ &= f(E)-f(E+qV_T) \end{aligned} \tag{3.14}$$

Note that the cross terms cancel because the tunnelling from $s \to t$ and $t \to s$ is symmetric. Therefore our total current is given by

$$I_T = \frac{4\pi q}{\hbar}\int_{-\infty}^{\infty}[f(E)-f(E+qV_T)]\rho_t(E+qV_T)\rho_s(E)|M_{ts}|^2dE \tag{3.15}$$

This equation shows that the total elastic current is proportional to the difference in filled states between the sample and the tip, integrated over all energies.

An illuminating result can be attained by making the approximation that the density of states and matrix element are constant and also setting the temperature to 0K. When the temperature is set to zero it is clear from Fig 3.3 that the only possible tunnelling states are between 0 and qV_T. Therefore we can change our integral limits to 0 and qV_T. We now see that the current is directly proportional to the voltage and we therefore expect an ohmic junction.

$$I_T = \frac{4\pi q}{\hbar}\rho_t\rho_s|M_{ts}|^2\int_0^{qV_T}dE = \frac{4\pi q}{\hbar}\rho_t\rho_s|M_{ts}|^2V_T \tag{3.16}$$

Imaging

By rastering the tip across the surface at a constant height and measuring the current we can build up a picture of the sample. However if there is a protrusion

from the surface there is a possibility that the tip will hit it. Also if the sample has a large variance in height, then at the lowest points the tunnelling current will be very weak. In order to avoid these problems, topography is measured in constant current mode. Here the current is kept constant by moving the tip towards and away from the sample. The movement of the tip is then recorded. This has the additional advantage of directly supplying the topography of the surface if the local density of states (LDOS) on the surface is constant.

An early use of the capability of an STM to image the topography of a surface with atomic precision was in its use on the 7x7 reconstruction of silicon. Here the structure of the surface, as shown in Fig 3.5 was imaged for the first time [31]. This had proved to be very difficult to reconstruct structurally due to the large unit cell of 49 atoms.

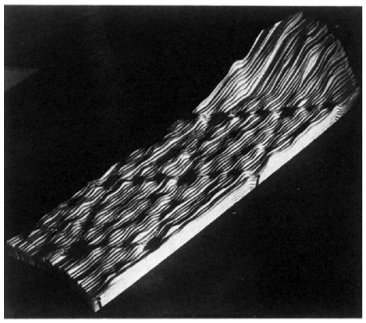

Figure 3.5: An STM image of the 7x7 reconstruction of silicon [31]

As the tunnelling current defines the height of the tip, changes in the LDOS will be observed in STM images. An example of this can be seen on Cu(111), where the STM tip probes the local density of states and images the standing waves caused by the scattering of the electron gas off defects and step edges [32]; this effect is seen in Fig 3.6.

A second example of the topographical image showing details of the LDOS is with a Mn atom in GaAs. On scanning at room temperature, an Mn atom is observed as a cross like shape [33]; an image of this is seen in Fig 3.7. This is caused by the anisotropy of the GaAs crystal structure.

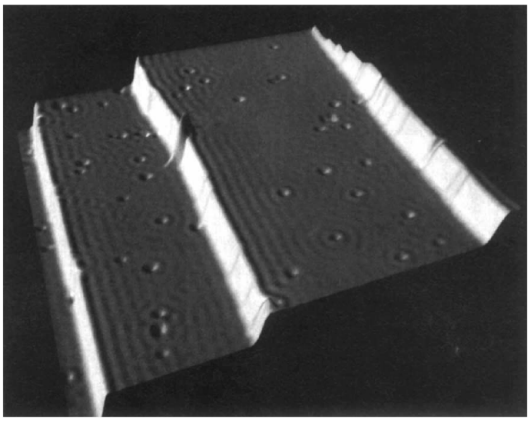

Figure 3.6: Standing waves on Cu(111). The standing waves have been caused by scattering off defects and step edges [32].

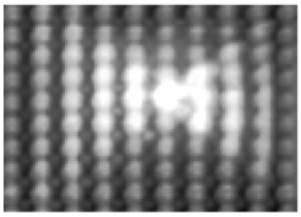

Figure 3.7: Mn in GaAs, the cross like shape observed is due to the anisotropy of the GaAs crystal structure [33].

3.2.2 Spectroscopy

We have seen that it is possible to use an STM to gain information about the LDOS of a system through imaging. This occurs due to the tunnelling current which defines the height of the tip being given by the integral of the density of states, however it is difficult at times to de-convolute the LDOS features from changes in topography. It is also possible to directly measure the LDOS with an STM. This is done by sweeping the bias while measuring the current and holding the tip in a stationary position above the sample. We will now go through the details of how this gives rise to a measurement of the LDOS. From the Eq. 3.15, assuming the matrix element is constant, the total current is given by

$$I_T = \frac{4\pi q|M_{ts}|^2}{\hbar}\int_{-\infty}^{\infty} dE[f(E) - f(E+qV_T)]\rho_t(E+qV_T)\rho_s(E) \tag{3.17}$$

Taking the derivative of the system with respect to V_T gives

$$\begin{aligned}\frac{\partial I_T}{\partial V_T} = \frac{4\pi q^2|M_{ts}|^2}{\hbar}\int_{-\infty}^{\infty} dE[f(E)\rho_t'(E+qV_T)\rho_s(E)) \\ -f'(E+qV_T)\rho_t(E+qV_T)\rho_s(E) - f(E+qV_T)\rho_t'(E+qV_T)\rho_s(E)]\end{aligned} \tag{3.18}$$

This can be simplified by making the assumption that the density of states in the tip is constant, giving $\rho_t'(E) = 0$. A further assumption that $T = 0K$ gives $f'(E)_{K_BT\to 0} = -\delta(E)$. Therefore only the second term remains and we get

$$\frac{\partial I_T}{\partial V_T} = \frac{-4\pi q^2\rho_t|M_{ts}|^2}{\hbar}\int_{-\infty}^{\infty} dE\rho_s(E)\delta(E+qV_T) = \frac{-4\pi q^2\rho_t|M_{ts}|^2}{\hbar}\rho_t\rho_s(qV_T) \tag{3.19}$$

Showing that $\frac{\partial I_T}{\partial V_T}$ is proportional to the LDOS.

However $\frac{\partial I_T}{\partial V_T}$ data is not taken at $T = 0$K; therefore it is necessary for us to look at how temperature effects our spectra. Taking Eq. 3.19, we make the approximation that both the matrix element and the tip density of states are constant. This therefore gives us

$$\frac{\partial I_T}{\partial V_T} = \frac{-4\pi q^2 |M_{ts}|^2}{\hbar} \rho_t \int_{-\infty}^{\infty} \rho_s(E) f'(E + qV_T) dE \tag{3.20}$$

The differential of the Fermi-Dirac function is given by

$$\frac{\partial f(E + V_T)}{\partial V} = \frac{-1}{4k_b T} \mathrm{sech}^2\left(\frac{E + qV_T}{2k_b T}\right) \tag{3.21}$$

giving us a temperature broadening of our spectra of

$$\frac{\partial I_T}{\partial V_T} = \frac{4\pi |M_{ts}|^2}{\hbar} \rho_t \int_{-\infty}^{\infty} \frac{\rho_s(E)}{4k_b T} \mathrm{sech}^2\left(\frac{E + qV_T}{2k_b T}\right) dE \tag{3.22}$$

From the equation it is not initially clear how this affects our spectra. One way to visualise this is to look at the effect on a flat LDOS with one infinitely sharp peak at energy E, as shown in Fig 3.8. The full width at half max (FWHM) of the peak of this function is $3.5k_bT$, however the value quoted is sometimes that of a fitted Gaussian which gives a width of $3.2k_bT$ [30].

$$\frac{\partial I_T}{\partial V_T} = \frac{4\pi |M_{ts}|^2 \rho_t}{\hbar} \int_{-\infty}^{\infty} \mathrm{sech}^2\left(\frac{E + qV_T}{2k_b T}\right) \delta(E) dE = \frac{4\pi |M_{ts}|^2 \rho_t}{\hbar} \mathrm{sech}^2\left(\frac{qV_T}{2k_b T}\right) \tag{3.23}$$

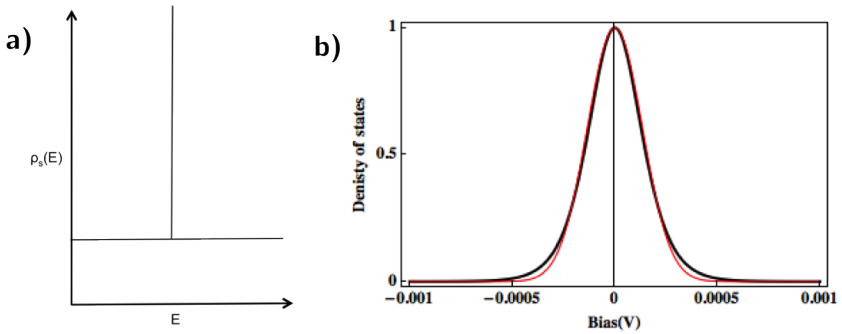

Figure 3.8: a) Idealised LDOS, an infinitely sharp peak with a flat background. b) Thick black line shows the line given by Eq. 3.23 giving a FWHM = $3.5k_bT$. The red line shows a fitted Gaussian; this gives a FWHM = $3.2k_bT$.

The LDOS of many materials has been measured with an STM, from semiconductors [34] to more exotic features in the local density of states such as superconducting

gaps and charge density waves [35, 36].

With STM it is possible to measure the variance of the LDOS with atomic precision. This allows for single magnetic atoms and molecules to be investigated, including Mn, Fe and Co single atoms and dimers on NiAl(110) [37]. Here spin-split resonances are observed in the unoccupied levels. Magnetic atoms have also been measured in GaAs [38]. The molecular levels of single molecules can be measured [39], even to a sub-molecular regime [40].

Kondo effect

Elastic spectroscopy measurements can be used to measure magnetic properties through the Kondo effect. The Kondo effect of a single magnetic atom was first observed for Co on Ag [41]. However a peak at the Fermi level in spectroscopy was not detected; instead a Fano line shape was observed. The Fano line shape was first defined for the inelastic decay of electrons in helium [42] where it describes a continuum coupled to a discrete state. It can therefore be used to describe STM tunnelling into a Kondo resonance.

The Fano line shape is calculated by first considering the effect of the resonance coupling to the continuum, producing a screened resonance. Next the coupling of the tunnelling electron is considered to each of the paths, the screened resonance and the unscreened continuum. The line shape is given by

$$|\langle\omega|\hat{T}|i\rangle|^2 = |\langle\Delta=\omega|\hat{T}|i\rangle|^2 \frac{q+\epsilon}{1+\epsilon^2}^2 \tag{3.24}$$

where

$$\epsilon = \frac{(\omega - E_k)}{\Gamma}$$

$$q = \frac{\langle\tilde{1}|\hat{T}|i\rangle}{\pi W(\omega)\langle\Delta=\omega|\hat{T}|i\rangle}$$

Here $|i\rangle$ is the initial state, in the specific case of an STM junction this is the tunnelling electron. $\langle\tilde{1}|$ is the screened discrete state, Δ the continuum and ω is the

energy of the state. In the case of a magnetic moment on a metal surface, Δ is the metal surface, and $\langle\tilde{1}|$ is the magnetic moment when screened by the interaction with the conduction electron. ω is the energy of the interacting particle, and therefore in STM is the voltage.

The amplitude of the the Fano line shape is proportional to the tunnelling into the unscreened continuum, Γ describes the coupling between the unscreened continuum and the screened resonance. The value q, often called the q factor, depends on the ratio of tunnelling into the screened resonance over the tunnelling into the unscreened continuum. Figure. 3.9 shows how the value of q modifies the Fano line shape. When $q = 0$, an anti-resonance is observed; in this case the tunnelling is all into the continuum; at $q = \infty$ it is a peak, and the tunnelling is into the resonance; finally when $q = 1$ and the ratio of tunnelling is roughly equal, an S shape is observed.

As shown in Fig 3.10, experimental $\frac{dI}{dV}$ data can be fitted by a Fano line shape,

$$\frac{dI}{dV} = C + \frac{A}{(1+q^2)}\frac{(q+\epsilon)^2}{(1+\epsilon^2)} \tag{3.25}$$

In this equation, C is the offset, A is the amplitude and q and ϵ are defined as above.

That the Fano line shape is caused by the Kondo effect can be shown by studying the effect of temperature or field on the line shape [7, 43]. The Kondo effect is affected by the surface, as seen in the studies on Co on both Cu(001) and Cu(111) [44]. T_K is seen to vary greatly between Cu(001), $T_K = 88$K, and Cu(111), $T_K = 54$K. This is due to Cu(001) having a higher electron density at the adatom because an atom in Cu(001) has four neighbouring copper atoms rather than the three that neighbour a Cu(111) atom.

STM has also been used to study the interaction of multiple Kondo impurities. The Kondo effect is seen to disappear when two Co atoms are brought within 6Å of each other, this is due to the reduced exchange coupling between gold conduction electrons and ferromagnetic cobalt dimers [45]. By placing one magnetic atom on the tip, and one on the sample, it is possible to tune the the interaction between the two atoms; this results in the ability to move from a Kondo screening to anti

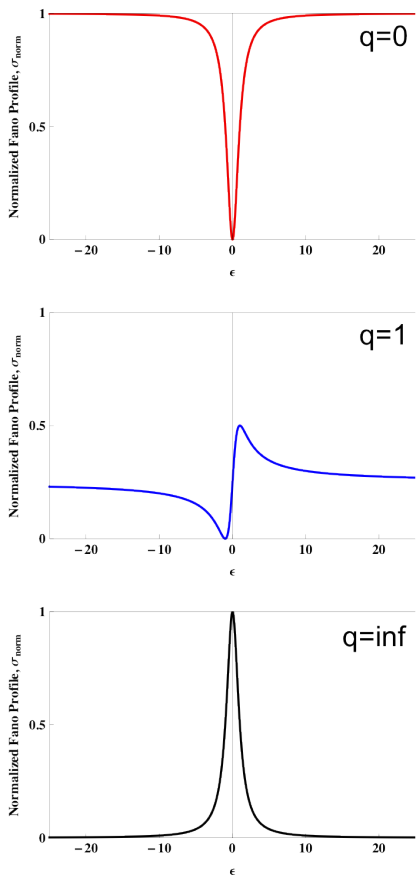

Figure 3.9: This figure shows the effect of q on the Fano line shape. When $q = 0$, as in the top graph, the line shape is a dip; when $q = 1$ it is an S shape; when $q = \infty$, as in the bottom graph, the line shape is a peak.

ferromagnetic coupling [46].

By investigating Co atoms with attached molecular ligands it is shown the local chemical environment plays a key role in the Kondo effect [47]. This is further shown by investigating a phthalocyanine molecule with Co in the centre (CoPc) adsorbed on to a Au(111) surface [48]. A Kondo effect is not observed over the pristine molecule, however on removing eight hydrogen atoms from the molecule a clear Kondo resonance is observed. FePc on Au(111) has been observed to show a Kondo resonance without any manipulation [49].

Kondo is not only observed in molecules due to magnetic moments created by metal atoms; electrons on organic molecules have also been shown to create Kondo [50,51]. Spectroscopic measurements on terbium double decker phthalocyanine, which has

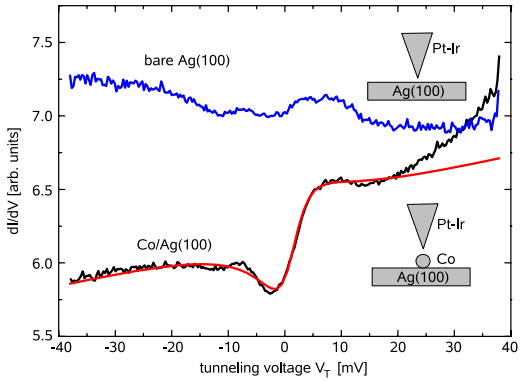

Figure 3.10: This figure shows the a fitted line Fano line shape due to the Kondo effect. This spectrum was taken with a Pt-Ir tip of Co on Ag(111) [30].

been seen to be an SMM in the bulk, show a Kondo effect when placed on a metal due to the delocalised electron on the ligand [52, 53].

Spin polarised STM

In spin polarised STM, the spin of the atom on the tip acts as a spin filter polarising the tunnelling electrons to the direction of the spin of the tip. These preferentially tunnel into states with a parallel spin, allowing for spin sensitive STM measurements [54]. The basic principle behind spin polarised STM is shown in Fig 3.11 [55]. When the spins are aligned, there are more states for the electron to tunnel into and therefore the current is high. When the spins are anti-aligned the number of states is smaller and therefore the current is reduced.

The variation of the spin appears in measurements of topography as in order to maintain a constant current set point, the tip moves closer to the surface when the spins in the tip and the sample are anti-aligned and moves back when the spins are aligned. This process was first shown to be possible with an STM by Wiesendanger *et al.* [54]. A ferromagnetic CrO_2 tip and a tungsten tip were used on Cr(001). The step size taken by the tungsten tip was compared to that taken by the CrO_2 tip. The CrO_2 tip data shows two alternating step heights that average to the step height recorded by a tungsten tip. As Cr(001) is known to have alternating spin-up and spin-down terraces, the data shows that the CrO_2 tip is measuring the spin of the sample as well as the topography.

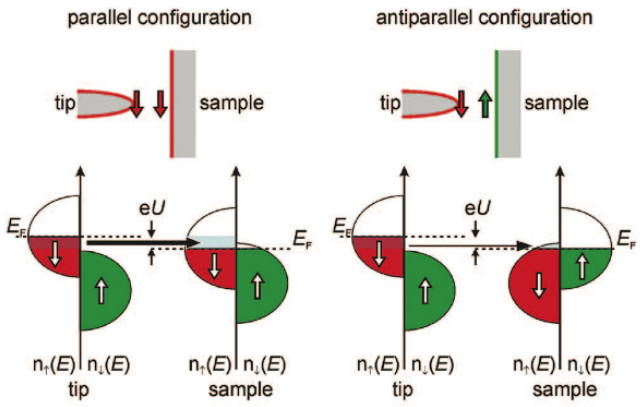

Figure 3.11: The spin polarised tunnelling current that flows between the tip and the sample depends on the alignment of spin between the tip and the sample [55]

A ferromagnetic tip is not the only technique for detecting spin with STM. Antiferromagnetic tips were used to investigate monolayers of Fe on W(110) [56]. The advantage of an antiferromagnetic tip is that it does not have its own stray magnetic field. As STM tunnelling is dependent on the last atom, a spin polarised STM tip can be created by picking up a magnetic atom from the surface [57]. Another method used is to place a modulation on the tip to rapidly change the magnetisation of the tip. By using different shaped tips it is possible to measure the magnetism in plane [58].

Spin polarised STM was used to detect single spins in antiferromagnetic layers, for example antiferromagnetic manganese films on tungsten [59]. It can also be used to measure the spin of individual Fe and Cr atoms adsorbed onto Co nano-islands. Spin polarised STM can be used to produce magnetization curves; this allows the spin of an individual cobalt atom on Pt(111) to be mapped [60] . It can also be used to look at CoPc to spatially resolve the spin states of a single molecule [61]. By imaging single Co atoms and manipulating these atoms on a Mn/W(110) surface it is shown it is possible to construct and analyse atomic level magnetic structures [62].

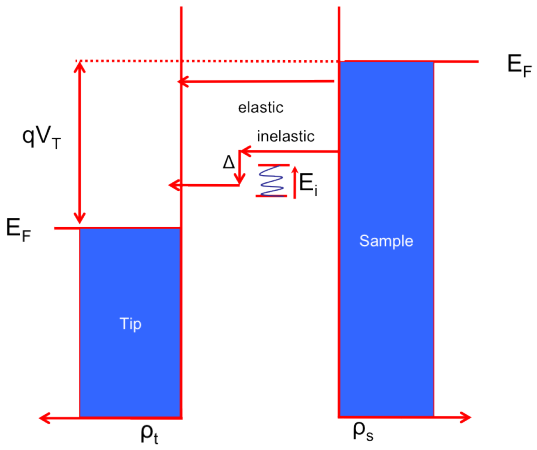

Figure 3.12: A tunnelling junction at T=0K, showing both the elastic and inelastic pathway for a positively charged particle. The inelastic pathway is shown where Δ is the energy lost in the transition and E_i is the excitation that is created. Due to energy conservation $E_i = \Delta$.

3.2.3 Inelastic Electron Tunnelling

Theory

Inelastic tunnelling occurs when an electron tunnels across the junction and in the process of tunnelling loses energy to an excitation, as shown in Figure 3.12. This process occurs only when the electron has enough energy to remain above the Fermi energy. Although the elastic and inelastic pathways are not completely independent, we may treat them as such and gain a good approximation in most cases [63]. When this process is possible a second pathway opens usually causing a rise in conductance.

The total current will be the sum of both the elastic and inelastic currents. An assumption made throughout this section is that the lifetime of the excited state is much smaller than that of the average time between two tunnelling occurrences. When this assumption is not true, spin pumping can occur [57].

The inelastic tunnelling current is found in the same way as the elastic tunnelling current. Fermi's golden rule gives the transition rate of a single electron in a single state, at a specific energy. On integrating over all possible states and energies the total rate of transition is found and then we multiple by the charge in order to get the current. The elastic and the inelastic currents differ in that it is necessary to

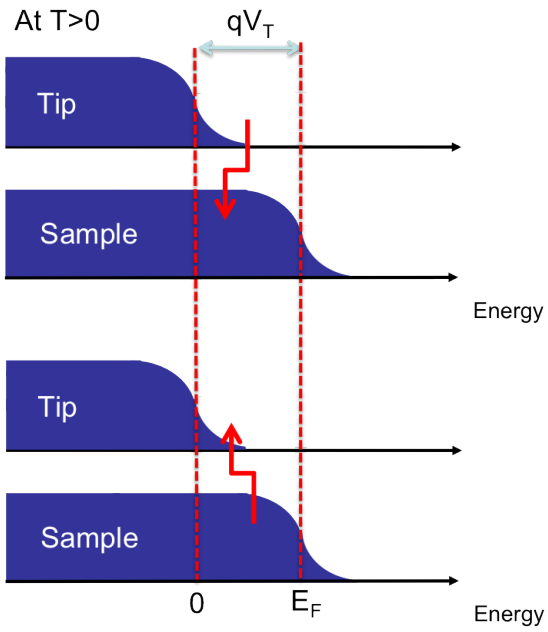

Figure 3.13: The tunnelling junction for $T > 0K$, The inelastic pathways in both direction are marked on the figure. Note that the arrows are not symmetrical but that the energy is lost in both cases.

account for the energy Δ lost in the inelastic tunnelling process.

In elastic tunnelling a positively charged particle tunnelling from the sample is $+qV_T$ in energy above the tip and therefore tunnels into the $E + qV_T$ state in the tip. For inelastic tunnelling the particle will lose energy Δ while tunnelling. This means that the particle will tunnel into the $E + qV_T - \Delta$ state in the tip. For tunnelling in the opposite direction the particle tunnels from a state $-qV_T$ below the energy of the sample. In tunnelling it loses energy of Δ. This results in it tunnelling into the sample at an energy of $E - qV_T - \Delta$.

The total rate of inelastic transition, from sample to tip, is given by

$$W_{s\to t} = \frac{(2)2\pi}{\hbar}\int_{-\infty}^{\infty} dE_t \int_{-\infty}^{\infty} dE_s \; f(E_s)(1-f(E_t))\rho_t(E_t)\rho_s(E_s)|M_{ts}|^2\delta(E_s-(E_t+qV_T-\Delta)) \tag{3.26}$$

$$= \frac{4\pi}{\hbar}\int_{-\infty}^{\infty} dE \; f(E)(1-f(E+qV_T-\Delta))\rho_t(E+qV_T-\Delta)\rho_s(E)|M_{ts}|^2$$

Therefore our total inelastic current from sample to tip is given by

$$I_{s\to t} = \frac{4\pi q}{\hbar}\int_{-\infty}^{\infty} dE\ f(E)(1-f(E+qV_T-\Delta))\rho_t(E+qV_T-\Delta)\rho_s(E)|M_{ts}|^2 \quad (3.27)$$

Comparing this to the elastic current for tunnelling from the sample to the tip, equation 3.9, it is clear that the only difference is the addition of the Δ due to the loss of energy in the tunnelling pathway.

The total rate of inelastic transition from tip to sample is given by

$$W_{t\to s} = \frac{(2)2\pi}{\hbar}\int_{-\infty}^{\infty} dE_t \int_{-\infty}^{\infty} dE_s\ f(E_t)(1-f(E_s))\rho_t(E_t)\rho_s(E_s)|M_{ts}|^2\delta(E_t-(E_s+qV_T+\Delta))$$

$$= \frac{4\pi}{\hbar}\int_{-\infty}^{\infty} dE\ f(E+qV_T+\Delta)(1-f(E))\rho_t(E+qV_T+\Delta)\rho_s(E)|M_{ts}|^2 \quad (3.28)$$

The total inelastic current, from tip to sample is then

$$I_{t\to s} = \frac{4\pi q}{\hbar}\int_{-\infty}^{\infty} dE\ f(E+qV_T+\Delta)(1-f(E))\rho_t(E+qV_T+\Delta)\rho_s(E)|M_{ts}|^2 \quad (3.29)$$

The total inelastic current is

$$I_{Inelastic}^{Total} = I_{t\to s} - I_{s\to t}$$

$$= \frac{4\pi q}{\hbar}\int_{-\infty}^{\infty} dE|M_{ts}|^2[f(E+qV_T+\Delta)(1-f(E))\rho_t(E+qV_T+\Delta)\rho_s(E)] \quad (3.30)$$
$$-[f(E)(1-f(E+qV_T-\Delta))\rho_t(E+qV_T-\Delta)\rho_s(E)]$$

In order to find the total current it is necessary to add the elastic current, given by Eq. 3.13. By comparing the formula for the elastic current (Eq. 3.15) with that for the inelastic the similarities are obvious. However due to the loss of energy Δ not

sharing the same sign for the two tunnelling directions it is not possible to cancel out the cross terms and so the formula for the inelastic current cannot be simplified further.

From this, the first and second differentials with respect to V can be calculated. These are shown in the papers by Kogan *et al.* [64] and Lambe and Jaklevic [65] respectively. Note the convention has been used that $q = -e$. A_e is a constant that represents the elastic current, A_i is the constant that gives the strength of the inelastic current.

The first differential with respect to voltage is given by

$$\frac{\partial I_T}{\partial V} = A_e + A_i(F(\frac{eV - \Delta}{k_b T}) + F(-\frac{eV - \Delta}{k_b T}) \tag{3.31}$$

where

$$F(x) = \frac{1 + (x-1)e^x}{(e^x - 1)^2} \tag{3.32}$$

Figure 3.14 shows the line shapes of the first differential for different energy regimes.

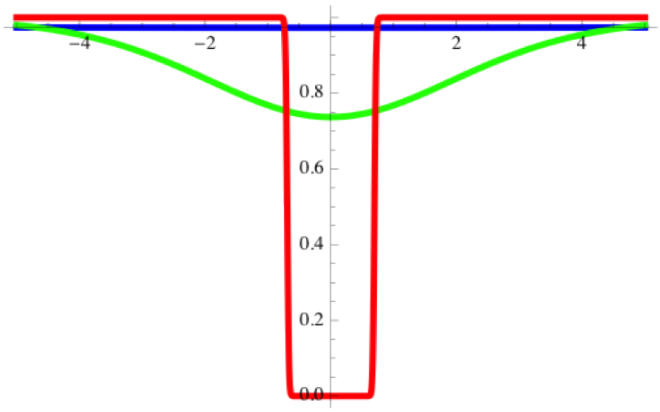

Figure 3.14: Line shape of first differential with respect to V. Shown are three line shapes each representing a different regime. The blue line shows that if $\Delta << T$ then it is very hard to see the effect of inelastic tunnelling. The green line shows that where $\Delta \approx T$ the spectra is broadened substantially but still seen. The red line shows that when $\Delta >> T$ then there is very little broadening and the influence of inelastic tunnelling is very clearly seen.

The line shape of the second differential with respect to voltage is shown in Fig 3.15.

The formula is,

$$\frac{\partial^2 I_T}{\partial V^2} = \frac{Ce^2}{k_b T}\left(\frac{e^x(x-2)+(x+2)}{(e^x-1)^2}\right) - \frac{Ce^2}{k_b T}\left(\frac{e^y(y-2)+(y+2)}{(e^y-1)^2}\right) \tag{3.33}$$

where

$$x = \frac{eV+\Delta}{k_b T}$$

$$y = \frac{\Delta - eV}{k_b T}$$

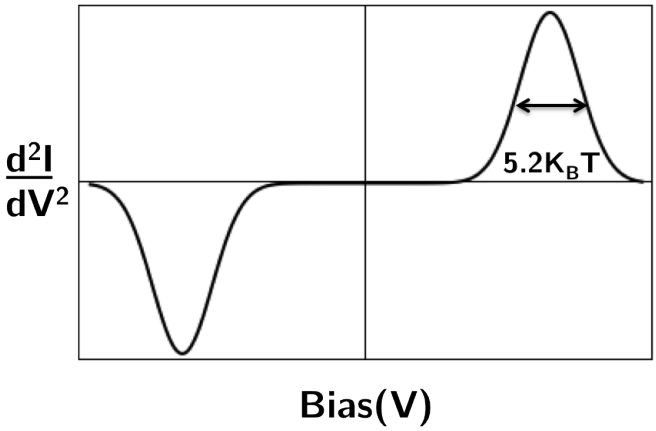

Figure 3.15: Line shape of second differential of the inelastic spectroscopy differential, the full width at half maximum of $5.2k_bT$ is shown.

From the second differential we can calculate the effect of temperature on the junction by calculating the full width at half maximum. The FWHM value is $5.2k_bT$. Throughout we have discussed broadening with respect to temperature, there are also other effects which also cause broadening. An example of this is the modulation voltage from a lock-in amplifier which can be used to directly measure the first differential with lower electrical noise than otherwise possible [66].

Experiments

Inelastic tunnelling was first observed by Lambe and Jaklevic in 1968 [65]. Here in studying electron tunnelling through a metal-oxide-metal boundary with molecules placed in the junction it was seen that there was a jump in conductance that coincides with the vibrational energy of the bonds in the molecule. The first use of

inelastic tunnelling in STM was carried out on a single acetylene molecule (C_2H_2) adsorbed on the Cu(001) [67]. A jump in conductance is seen at 358mV due to the excitation of the C-H stretch modes. This area of research has proved profitable with a large number of molecules studied using the same techniques [68].

The first work using IETS on a single spin looked at a single Mn atom on an Al_2O_3 thin insulator on NiAl [69]. Here IETS was used to measure the energy required to flip the spin of single adsorbed atoms. A magnetic field was used to spilt the degeneracy of the levels. At low bias the electrons do not have enough energy to excite the higher state and so all tunnelling is elastic. When the bias reaches the Zeeman splitting energy the electrons, when tunnelling, can flip the spin of the atom by transferring energy; this is the inelastic pathway. The Al_2O_3 layer acts as an insulator separating the manganese atom from the NiAl surface atoms. This means that the manganese atom can be considered to be independent. From this the g factor can be extracted, giving a value of $g = 1.88$. Figure 3.16 shows the conductance onset and how this only occurs on the manganese atom when it is isolated from the surface.

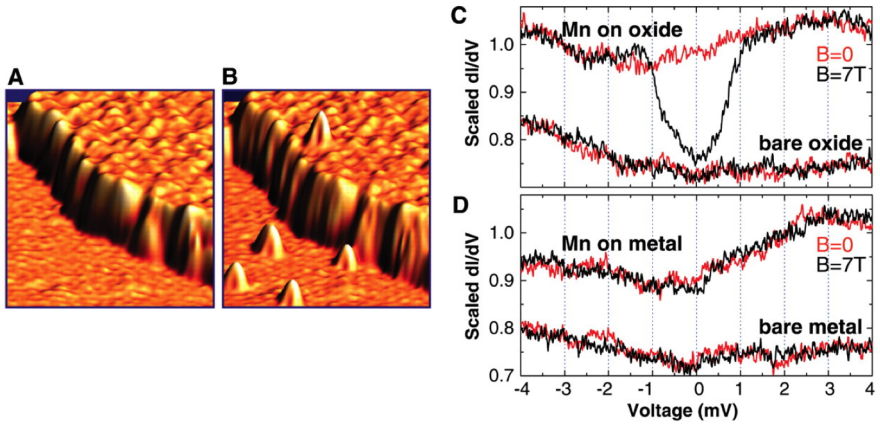

Figure 3.16: Single manganese atoms on a AlO_3 thin insulator on NiAl [69]. The increase in conductance above a voltage corresponding to the Zeeman splitting is clearly seen in the case where the Mn atom is on Al_2O_3.

IETS was used to investigate antiferromagnetic chains of Mn atoms which had been created by atomic manipulation. Here Cu_2N was used as an insulator. By using the Heisenberg open chain model the spin and anti ferromagnetic coupling were extracted from the IETS spectra [70].

Similar methods were used to measure individual Fe and Mn atoms on Cu_2N [6].

By modelling the system with a spin Hamiltonian, the orientation and strength of the magnetic anisotropies were calculated from the jumps in conductance recorded by IETS. Co and Ti single atoms were also studied [7]. It is seen that both show Kondo resonances on Cu_2N and can be modelled with a spin Hamiltonian with axial symmetry. It is also seen that the magnetic anisotropy of Co atoms changes depending on the binding site [71].

Dimers of Co and Fe on Cu_2N were studied as inhomogenous dimers [72]. It is observed that the Kondo resonance on the Co is split into two peaks. However by applying a magnetic field with the correct magnitude and direction the peak can be reconstituted. From modelling it is seen that the magnetic field results in a spin-level degeneracy in the dimer, thereby enabling the Kondo effect to occur.

Recently work has been conducted on Fe atoms in InSb [73] and on Cu(111) [74]. Here spin excitation steps were observed without the use of a thin insulator to decouple the spin from the interactions with the metal.

Spin excitation IETS has also been carried out on molecules. In the work by Chen *et al.* CoPc thin films were analysed with IETS [75]. In this work the first layer of molecules decouples the layers above from the interactions with the surface. These layers of molecules are seen to form one-dimensional antiferromagnetic chains through the film. It is also shown that a Kondo resonance can be seen in the second layer if the molecule is directly above the molecule in the first layer. However if the molecule is moved so that it is not seated directly above the lower molecule the Kondo resonance disappears. Further work has shown that it is possible to identify the charge state in this system [76].

For FePc on oxidised Cu(110) [8], zero-field splitting is only seen when the FePc is sitting on the oxide layer. The magnetic anisotropy of the FePc molecule varies depending on the binding angle of the molecule on the substrate. Further work on molecules was carried out to study the magnetic properties of Mn-12 acetate, a single molecule magnet in bulk crystals, using IETS [18].

Spin dynamic measurements

Recently it has been shown that it is possible to measure spin relaxation times using an STM, allowing for the measurement of the spin lifetimes of single atoms and

nano structures. By using a spin-polarised STM tip, and going to high currents, it is possible to spin pump an atom. This can be observed in spin excitation spectroscopy and the spin relaxation time can be calculated [57]. The spin relaxation time can also be calculated through the width of the spin excitation step in spectroscopy [74,77,78]. As long as the temperature does not dominate the linewidth, the width of the spin excitation is set by the uncertainty principle allowing for measurements of the spin excitations down to the femtoseconds [74]. Pump probe techniques allow for measurements of spin relaxation life times from nano seconds up to micro seconds [79]. Above micro seconds, spin relaxation times can be measured using simple telegraph measurements; the difficulty in these measurements is finding systems where the spin relaxation time is slow enough [80–82].

3.3 X-ray measurements

3.3.1 Introduction

X-ray absorption spectroscopy (XAS) and X-ray magnetic circular dichroism (XMCD) are chemically specific, and therefore can be used to measure both the electronic and spin structure in different elements in the sample [83]. Both XAS and XMCD are sensitive down to sub monolayer coverages, if the total electron yield (TEY) is measured. This allows for the characterisation of magnetic moments at the atomic scale. However the disadvantage of XAS and XMCD compared with STM is that with STM a single atom or molecule is measured and the local environment can be observed. In x-ray experiments the spot size is approximately 1mm^2 and therefore it is an average over many different molecules or atoms.

XAS

As XAS probes the valence shell occupation number, including the symmetry of the unoccupied electrons, it allows for the measurements of chemical state of the molecule. By selectively tuning the x-ray beam in energy it is possible to measure the absorption at each energy. However in these experiments the absorption is not directly measured; instead, total electron yield is measured. The reason for this is

that the 3d edges of transition metals have such a large cross section that samples would have to be 20nm thin to allow any beam through [83].

Absorption of x-rays results in the excitation of electrons from a core level to the unoccupied valence states. The core hole decays rapidly via either radiative transition with the emission of a photon or an Auger transition. In the Auger process the core hole is filled by an outer core electron and its energy is transferred to another electron which is emitted from the atom. This electron then scatters inelastically creating more electron-hole pairs, which leave the sample. By grounding the sample through an ammeter, the current can be measured to give the TEY. The mean free path of an electron is approximately 5 nm, resulting in XAS only being sensitive to the first 5 nm of the sample. Measurements for transition metals often occur at the L edge where a metal 2p electron is excited to the unfilled metal d-orbitals [83].

XMCD

As the intensity of x-ray absorption depends on the spin and orbital moment, relative to the x-ray polarisation, it is possible to gain magnetic sensitivity by comparing the difference between spectra taken with left handed circularly polarised light and right handed circularly polarised light [84]. From electron dipole selection rules it is seen that circularly polarised light can result in transitions of $\Delta m = \pm 1$ depending on the polarity (i.e left or right handed). Therefore by measuring the difference between polarisation it is possible to gain information on the the orbital and spin magnetic moment [84].

3.3.2 Measuring nanoscale magnetic moments

In TEY mode, only electrons from the first 5 nm of the sample can escape making XAS and XMCD inherently surface sensitive [83]. Coupled with the chemical sensitivity of the measurements this allows for the magnetic properties of sub-monolayer coverages of magnetic atoms and molecules to be measured [27,85]. XMCD measurements have been used to measure magnetic atoms and nanostructures on metals. It has shown how the orbital magnetic moments in transition metals are progressively quenched as clusters are formed [86]. It has also been used to observe ferromag-

netism in one dimensional chains [87], and a large magnetic anisotropy for Co on Pt(111).

XMCD can also be used for investigations of molecules [85]. A monolayer of CuPc has been measured where it is observed that the Cu moment survives deposition [88]. Measurements on Fe^4 have shown that its magnetic moment survives the deposition on a metal surface [89, 90] and also investigations of lanthanide based SMM's have occurred [91–94].

3.3.3 Spin Crossover molecules

Spin crossover molecules are an area which nicely illustrates where XMCD can provide more information than STM investigations. These molecules contain a transition metal, such as Fe, which can be reversibly switched between two distinct spins, a low spin state (LS) and a high spin state (HS) [9]. Due to an external factor varying the energy splitting of the atom, the ground state changes and this results in a change in the spin state. If the ligand field is smaller than the pairing energy then electrons will fill the higher levels before pairing up in the lower orbitals. However if the pairing energy is lower, then the electrons will prefer to pair up in the lower orbitals. As the electrons are paired when the ligand energy is higher, this will result in a lower spin state, as can be seen in Fig 3.17.

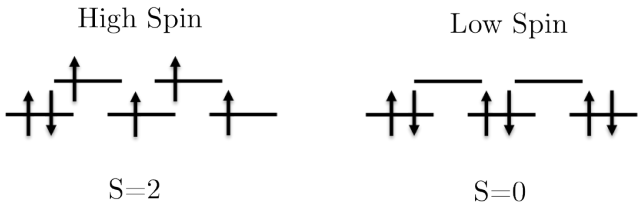

Figure 3.17: The levels of Fe(II) in an octahedral ligand field is displayed. Depending on the whether the ligand field is larger or smaller than the pairing energy the Fe atom can be in a high spin or low spin state.

In spin crossover molecules the ligand energy and the pairing energy are of a similar magnitude, and by manipulating one of these energies it is possible to move from the high spin state to the low spin state. This switching can be driven by a variety of external phenomena such as temperature, light, magnetic field, charge flow, and pressure. This behaviour has been measured in various systems including bulk, thick

films, and nano particles [9]. In STM measurements, voltage induced switching has been observed when the molecules are decoupled from the surface [95, 96]. However it has not been possible to directly measure the spin state of the molecule. When the molecules are coupled to a metallic surface no voltage switching is observed with STM.

Observing SCO in single molecules on a surface

By utilising XAS we show that it is possible to observe the transition from the high spin state to the low spin state induced through temperature and light in the single molecules of the complex [Fe(H_2B- (pz)$_2$)$_2$(bipy)] [97]. XAS on a sample formed by a single crystal rubbed onto a gold foil is shown in Fig 3.18. Here the $L_{2,3}$ edge spectra is shown for sample temperatures of 300K and 100K. A change in both the L_2 and L_3 edge is seen with temperature. Due to the spin crossover transition from an S=2, $t_{2g}^4 e_g^2$ configuration to a S=0, $t_{2g}^6 e_g^0$ configuration as the temperature lowers, the energy of transition changes and this is what causes the change seen in the XAS data.

The transition from S=0 to S=2 is not simply a temperature driven phenomenon, it can also be driven by laser irradiation. The samples were irradiated by laser at 10K (658nm). This causes the HS state to be populated by Light induced Excited Spin State Trapping (LIESST) [98]. The spectra taken at 10K after laser irradiation are shown in Fig 3.18. It is again easy to see the change in spectra due to the difference in populations.

Spectra for sub-monolayer coverage are shown in Fig 3.19. It was not possible to image these molecules with STM, this is likely due to the molecules being mobile at room temperature on the Au(111) substrate. Therefore evidence for the coverage being sub monolayer comes from the XAS data. By comparing the edge jump between the bulk and sub-monolayer we can gain an estimation of the coverage. For the bulk we see a jump of 247% and for the sub-monolayer we see an increase of 2.3%. This means that the jump for the sub monolayer is approximately 100 times less than the jump observed on the bulk sample. As the data were collected in TEY mode, it is only sensitive to the top 5nm; this is equivalent to approximately 4 layers of molecules [99]. Therefore the coverage on the sub-monolayer is approximately 4% of a monolayer.

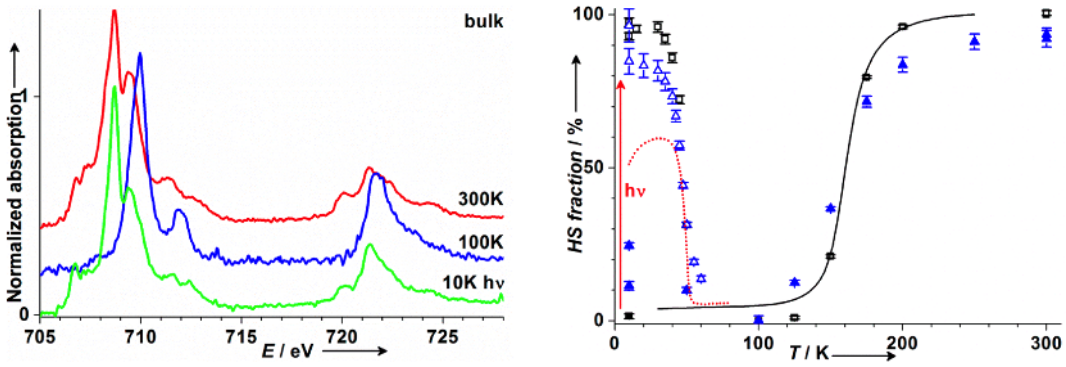

Figure 3.18: Left graph: Normalized spectra on bulk molecules (absorption at maximum) at 300 K (red line), 100 K (blue line) and 10 K (green line) after illumination (658 nm cw laser, 15 mW.cm^{-2}). Spectra are shifted vertically for clarity. Right graph: HS fraction versus temperature derived from the linear interpolation of the XAS spectra for the bulk compound before (filled black squares) and after illumination (empty black squares) and the 300 nm thick film before (filled blue triangles) and after illumination (empty blue triangles), compared to the magnetometric results on the bulk compound before (full line) and after illumination (red dotted line).

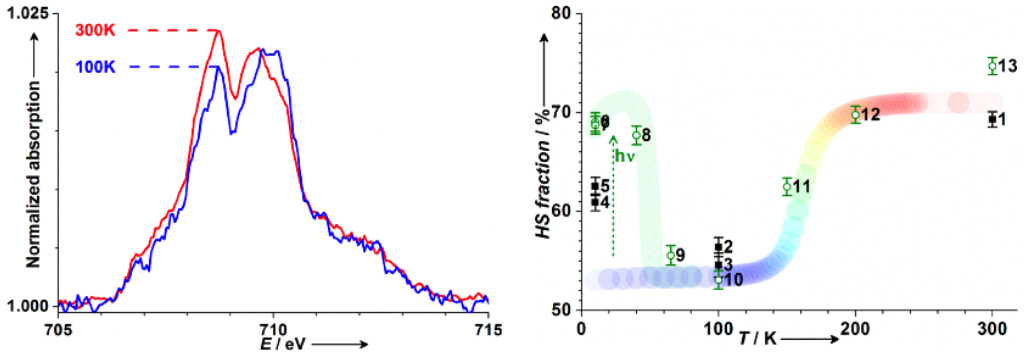

Figure 3.19: Left graph, Comparison of spectra at the L3 edge (705-715 eV) for the sub-monolayer sample at 300 K and 100 K (red and blue lines respectively). Right graph, HS fraction versus temperature derived from the linear interpolation of the XAS spectra for the sub-monolayer sample; filled squares are before laser irradiation, and green empty circles are after laser irradiation (numbers label the acquisition order). As a guide to the eye, the shifted and rescaled temperature dependence of the thermal- and photo induced HS fractions of the bulk specimen are drawn as faded bands. Note that the HS fraction scale ranges from 50 to 80% for clarity.

For the sub-monolayer coverage we again observe a change in the population when the temperature is lowered from 300K to 100K; however in this case we see a much smaller change. At 300K we see a HS/LS ratio of 69:31, and at 100K we observe a ratio of 56:44. This suggests that a large proportion of the molecules are pinned in one or the other of the spin states as has been observed previously [96]. This work shows that temperature- and light-induced spin crossover can occur on isolated molecules, which allows for the possibility of addressing their spin states through temperature or light in spintronic applications.

3.4 Nanoscale junctions

Another method which can be used in measuring single magnetic moments is via the use of nanoscale junctions. This method is not ultilised in this thesis, but a brief outline is included for completeness.

In nanoscale junctions, arrays of nanowires are formed on an insulating substrate through lithographic techniques. A dilute solution of molecules is then spread across the substrate. The nanowire array is then broken in a controlled way via one of two methods. One method is to mechanically break the wire. This can be done by placing a piezo stack under the substrate; the stack is then extended stretching the substrate until the nanowires crack. A second method is to place a gradually increasing current through the nano wires. This causes the nanowire to break at the thinnest point due to the power dissipation being largest here [24].

After deposition of molecules, a molecule is sometimes situated in the gap produced in the wire. This creates a gated device with the ends of the nanowires acting as source and drain with the substrate acting as a gate. The ability to gate is an inherent advantage of break junctions over STM [24]. In many break junctions a molecule is not present and it is necessary to study the transport characteristics across the junction in order to ascertain whether a molecule is present. In break junctions both electrodes are directly contacted by the molecule, in contrast to most scanning probe techniques [100]. The disadvantage of break junctions is that typically it is not possible to know the exact details of the junction or the geometry of the molecule [101].

Inelastic spectroscopy measurements can also be carried out on single molecules in nanoscale junctions [102]. Using this technique, the Kondo effect has been observed in single molecules [24,103]. It is also possible to tune the Kondo effect by varying the spacing of the electrodes using a mechanical break junction [101]; this method can also be used to modify the anisotropy of the spin by stretching the molecule [104]. By utilising a gate electrode is is possible to modify the spin state of the molecule [105]. Break junctions have also be used to investigate SMM's [106, 107].

Chapter 4

Experimental equipment

This chapter describes the two ultra high vacuum (UHV) STM systems on which the data in this thesis was taken. These are the Oxford STM and the Cryogenic STM; both of which are situated in the STM lab at the London Centre for Nanotechnology. The systems are operated at low temperatures and in UHV, where the pressure is lower than 1×10^{-9}mbar.

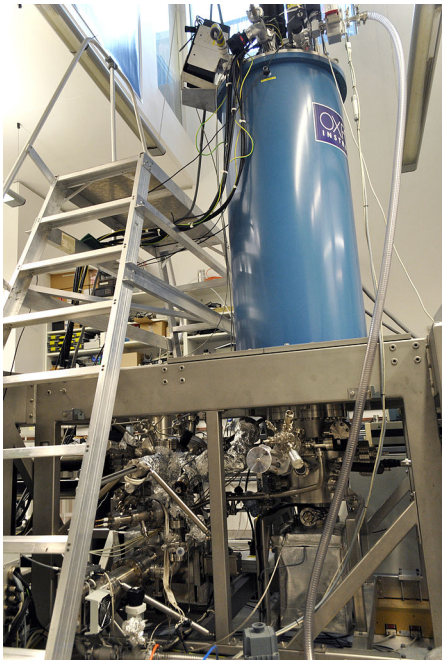

Figure 4.1: Picture of the Cryogenic STM, situated in the LCN.

4.1 UHV systems

4.1.1 Oxford STM system

This system consists of three chambers: analysis, preparation and molecular deposition chamber. The STM head sits in the analysis chamber which is connected to the preparation chamber, which is where most sample preparation occurs. Attached to the preparation chamber is a sputter gun and two leak valves for sputtering either Ar or N. Inside sits a sample stage on which the sample can be heated by radiative heating. Both the analysis and prep chambers are pumped by an ion pump and a titanium sublimation pump (TSP).

The third chamber is the molecular deposition chamber, where the molecular evaporator is situated. This chamber is connected to the prep chamber and is pumped via a turbo pump; additionally a TSP is connected to this chamber. Samples are loaded here and the chamber is baked before deposition of molecules. The pressure in all chambers is approximately 10^{-10}mbar. The STM head is cooled by a flow cryostat and has a base temperature of approximately 7K.

4.1.2 Cryogenic STM system

All measurements in this thesis are taken on Cryogenic STM System at 2.5K unless stated. The Cryogenic STM System was built in collaboration between Oxford Instruments and Omicron, which have since merged. A picture of the STM is shown in Fig 4.1. It is a pumped ^{4}He system with a base temperature for measurements of approximately 1.8K. It has a vectored magnetic field which has the capability of 6T perpendicular to the sample or 2T perpendicular to the sample and 1T parallel to the sample. It weighs approximately 1700kg (see Appendix).

The head of the Cryogenic STM is shown in Fig 4.2. It is constructed out of three sections with the sample stage and coarse positioning being in the lower half. The coarse positioning is in the z and x directions only. The upper section contains the tip stage and the fine positioning; in this system the bias is placed on the tip, however the control electronics read outs are all given in sample bias convention. Figure 4.3 shows the tip and sample stages. At the bottom the sapphire tube to which the

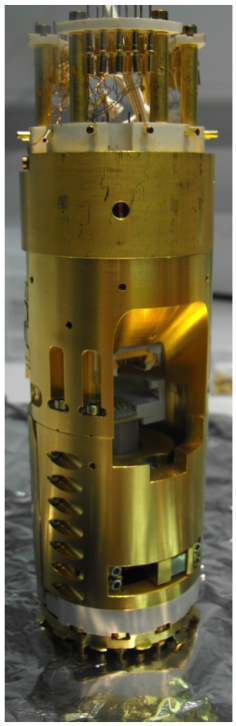

Figure 4.2: The head of the Cryogenic STM

ceramic sample stage is glued can be observed. The sample stage is constructed out of ceramic to allow for four contact measurements to take place. The four contacts can be seen in the centre, surrounded by Kapton wool. One of these contacts is grounded to the STM head.

The top reception stage is the tip stage, the construction of which can be seen in Fig 4.4. The separate tip and sample stage allow for the changing of the tip or the sample independently. A picture of a tip and sample plate is shown in Fig 4.5. The gap in the wall of the head between the two reception stages allows for line of sight access to the sample from the rear; this allows for the evaporation of metal on to a cold sample.

The STM head hangs via copper braids and springs from the helium pot, which can be pumped on to achieve a base temperature of 1.8K. Connecting the STM via spring provides damping and the copper braids increase thermal contact between the pot and the head. The pot is rigidly attached to a manipulator allowing the head to move from centre of the magnet to the analysis chamber for tip and sample exchange.

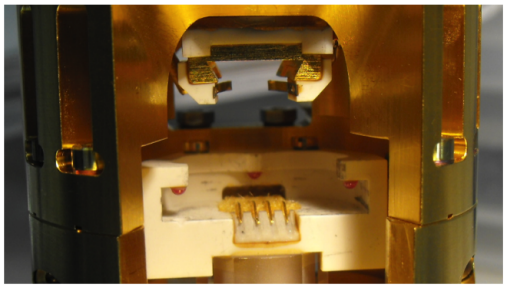

Figure 4.3: The sample and tip reception stage for the Cryogenic STM. The four metal prongs are contacts for the plate; for this reason the sample stage is made out of electrically insulating ceramic. One of these contacts is grounded to the STM. The hole in the back is to allow for metal evaporation straight onto the sample at low temperatures.

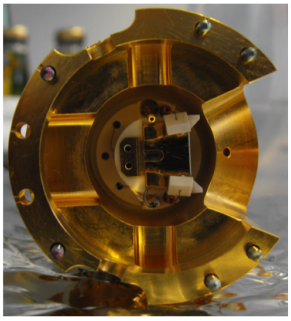

Figure 4.4: The bottom of the top half of the head. The bottom of the tip stage is clearly seen.

A diagram of the dewar is shown in Fig 4.6. The central insert sits in a UHV tube inside the dewar, inside the warm bore of the magnet cryostat. Between the warm bore and the helium dewar there is a small space, through which hot air flows during baking, allowing for the UHV tube to be heated. During measurements, cold helium gas is fed through this space to cool the UHV walls, reducing the heat load on the head. Surrounding this space is the helium can which contains the superconducting magnet. The helium dewar is surrounded by a nitrogen dewar. In order to reduce cryogen consumption, both dewars are maintained in a vacuum space.

The magnetic field is produced by three superconducting magnets; one solenoid which produces the perpendicular field, and two split coil magnets, to provide the field in the X and Y directions. As the cooling from the helium bath to the head can be controlled, this system has the capability to take data up to room temperature with the magnetic field on.

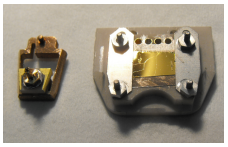

Figure 4.5: A tip and sample for the cryogenic STM in their respective holders.

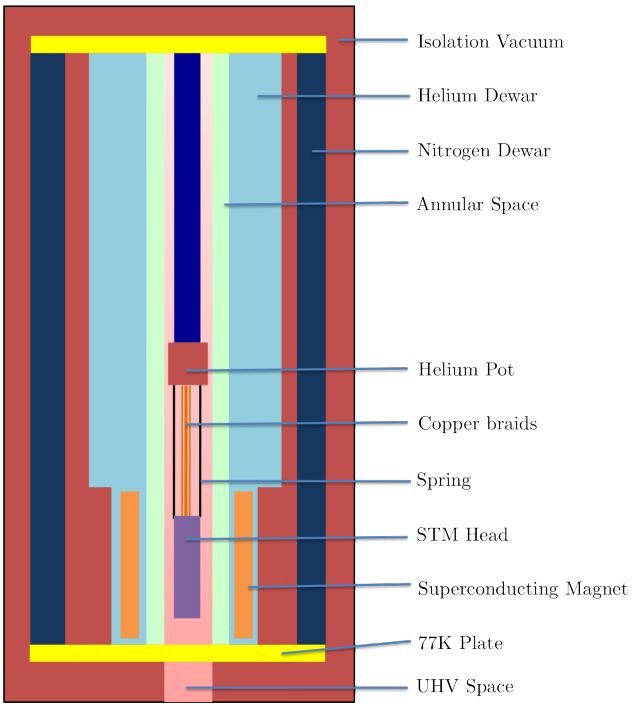

Figure 4.6: A diagram of the dewar of the cryogenic STM

Attached to the analysis chamber is a single source metal evaporator which has line of sight access to the head when it is in the sample transfer position. This allows for the evaporation of metal on to the sample sitting at approximately 30K. The evaporator is on a retraction package so that it can be valved off from the analysis chamber. This allows the metal in the evaporator to be switched without venting the entire system. Also present in the analysis chamber is a tip preparation stage.

On the prep chamber there is a large variety of instrumentation. An Auger spectrometer can be used to analyse the surface of the sample for impurities, and the residual gas analyser allows for the analysis of gases in the chamber. For preparation of a clean metal sample there is a sputter gun, and the transport arm includes the ability heat the sample both directly and indirectly. The transport arm also allows for the movement of the sample to both a hydrogen cracker and a three source metal

evaporator.

Molecules can be deposited in the load lock, which is baked after the venting of samples before deposition. The molecular evaporator (described further in Chap 5) is composed of a crucible in which the molecules sit, a thermocouple for measuring temperature, and a filament to heat the crucible.

Chapter 5

Sample Preparation

Preparation of atomically clean samples in UHV systems is of great importance if investigations at the atomic scale are to occur. In this chapter the techniques used to prepare samples are discussed. Finally the methodology of molecular evaporation is included.

5.1 Cu(001)

An atomically flat metal sample is prepared by cycles of sputtering and annealing. Sputtering is the process used to rid the sample of impurities. In sputtering atoms are ejected from a solid target material due to bombardment of the target by energetic ions. This process randomly removes the top layer of atoms, and therefore the impurities in the surface. This process is achieved by leaking argon gas into a sputter gun, where ions are created. These are accelerated towards the sample where the ions knock atoms out of the surface.

Annealing is the process of heating up a sample in order to rearrange its crystal structure. This is used to flatten the surface and also remove any argon which may be embedded from sputtering. A Pyrolytic Boron Nitride (PBN) heater is used to heat the sample indirectly; this consists of a filament wound through PBN insulator.

The STM is the primary mode of investigating the quality of the surface, however

this is a time consuming process. A faster process is to use Auger spectroscopy to check the state of the sample. Auger spectroscopy is a common technique used for the analysis of a sample as it allows you to quickly see the chemical makeup of the surface.

In Auger spectroscopy electrons are accelerated in an electron gun. These hit the atoms in the surface, knocking out inner shell electrons, creating a hole. Electrons in the outer shells drop down to fill this hole. In this process energy is released. This energy can couple to a second outer electron and if this is greater than the energy of the binding electron, a second electron is emitted. This is the Auger effect. As different elements emit electrons at distinct energies; by measuring the energy of the electrons emitted it is possible to determine the elements making up the surface layer. Figure 5.1 shows the spectrum of a Cu sample before and after the cleaning process. This data is taken via a Lock-in and therefore data shown is the differential. The additional peaks seen in the uncleaned sample (marked on the figure) are caused by sulfur, argon, carbon and oxygen respectively.

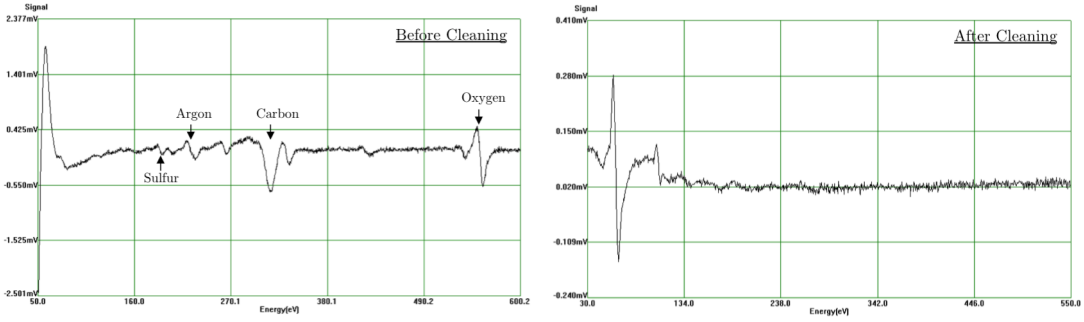

Figure 5.1: The spectrum of a Cu sample before and after cleaning of the surface. The left spectrum shows the surface before cleaning and has extra features due to impurities in the sample, each feature is labelled with the element responsible. The features at 60eV and 105eV are characteristic of Cu.

The experiments in this thesis were carried out on a Cu(001) sample purchased from Mateck. It is a single crystal with a purity of 99.999%; one side is polished to a roughness of less than 0.03 microns. The Cu(001) sample is aligned so that the |100| and |011| axes are parallel to the edges to an accuracy of better than 0.1°. Before preparing the copper surface it is heated overnight at 500°C to outgas the sample. To clean the sample, sputter/anneal cycles are carried out. The preparation chamber is filled with Ar to 6.0×10^{-6}mbar, and the sample sputtered for 15 minutes at 604V while the sample is annealed at approximately 500°C. The sample is then

annealed for a further 10 minutes after sputtering. This cycle is then repeated until the sample is presumed to be clean. For preparation of a Cu sample which has been in UHV, only one cycle is necessary.

An example of a clean Cu(001) surface is shown in Fig 5.2. There are few impurities on the surface and terraces up to 50nm wide can be seen.

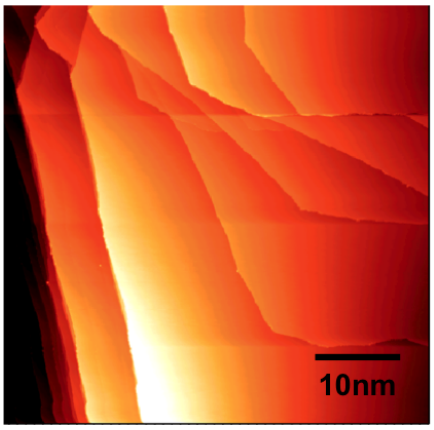

Figure 5.2: An STM image taken of Cu(001).

5.2 Copper nitride

The strong interaction between molecules and metallic substrates modifies the properties of a molecule [108], therefore in order to measure molecules which are closer to that of the free molecule with an STM, it is necessary to decouple the molecules. One method that has been used with great success is to decouple molecules from the surface using thin insulators. Various thin decoupling layers have been used including NaCl, Al_2O_3 and CuO; this has allowed for the measurement of sub molecular resolution imaging [40], vibronic states [109] and spin excitations respectively [8].

In this thesis we have used the thin insulator copper nitride (Cu_2N) as a decoupling layer. Copper nitride islands self assemble on Cu(001) [110,111] and monolayers can also be formed [80]. Cu_2N has been used for decoupling metal atoms from the surface [6, 72, 80] as well as templating molecules and metals [111–113]. One advantage of utilising Cu_2N is that the atomic structure of the Cu_2N is well understood [114] and therefore it may be possible to understand the binding of the molecule at the atomic scale.

The structure of the Cu_2N is shown in Fig 5.3. Nitrogen atoms absorb between every other copper atom. Cu_2N islands occur due to the lattice mismatch between Cu-N-Cu and Cu-Cu causing strain to be formed. This results in it becoming energetically favourable for an extra row of copper to form to release the strain, creating an island [115]. As the Cu_2N island is an insulator, it appears as a depression of 1.8Å in STM images of the surface at high bias voltage [110, 114].

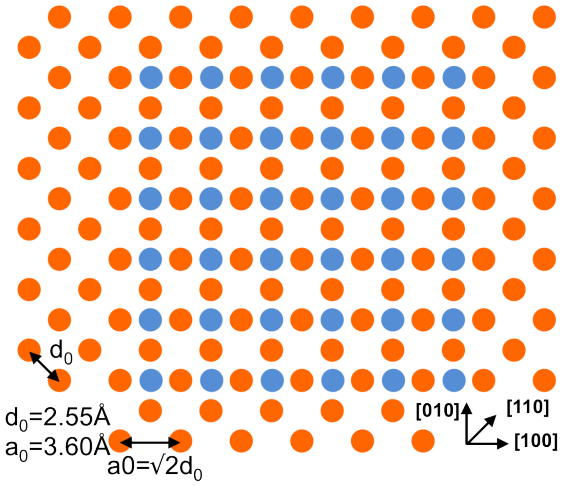

Figure 5.3: The copper nitride structure is shown, the nitrogen atoms (blue) insert between every other Cu atom (orange). An island forms to release the strain formed by the mismatch in the lattice constants of Cu-N-Cu and Cu-Cu

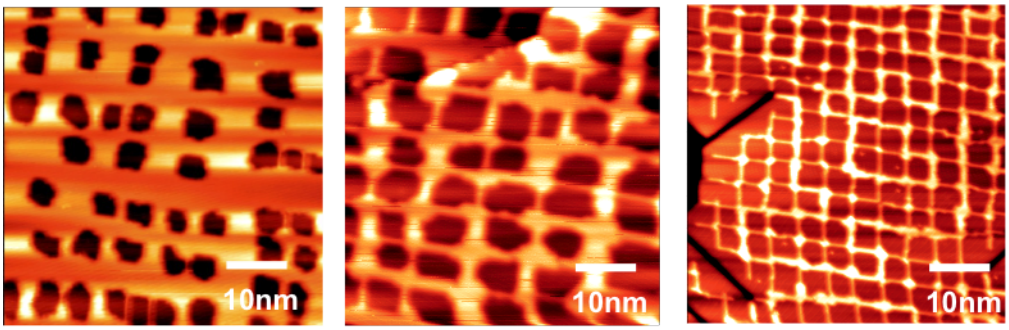

Figure 5.4: The coverage of Cu_2N can be varied by changing the sample preparation parameters. The pictures show the variation in island size and coverage that can be obtained. ($V_{set} = -1.0$V, $I_{set} = 50$pA)

A clean Cu surface is sputtered with N_2 to embed N atoms into the Cu. The sample is then annealed to a temperature of 300°C and sputtered for 5 min. By varying the pressure at which the nitrogen is sputtered, and the temperature and time period for which the sample is annealed for, the coverage of Cu_2N on the surface can be

controlled. Increasing the N pressure results in a greater coverage of the sample with Cu_2N. Increasing the anneal time and temperature of the anneal time results in larger, more regular islands. This variation can be seen in Fig 5.4.

5.3 Molecule evaporation

In order to allow for investigation of single molecules it is necessary to controllably place them onto surfaces without damage and without destroying the clean surface. Recently it has been shown that it is possible to use mass spectrometry to place large delicate molecules onto a surface cleanly [18]. However this requires a large investment of time, money and infrastructure. Molecules can also be placed on a surface by using the tip to transfer from a drop cast sample to a metal [19].

A simpler technique which has been used with great success is to sublime molecules onto the surface. The restriction with this technique is that it is limited to molecules which are thermally stable. In most setups the molecules are placed into a crucible which is heated by a filament. In Fig 5.5 the crucible is shown. Two cavities can be observed in the crucible. The top cavity forms a bowl into which the molecules are loaded, while the second cavity in the side allows for the insertion of a thermocouple. This ensures a good thermal contact, and therefore an accurate readout of the temperature. Also shown in Fig 5.5 is the heat shield which is placed around the filament and crucible to reduce the power lost to the surroundings.

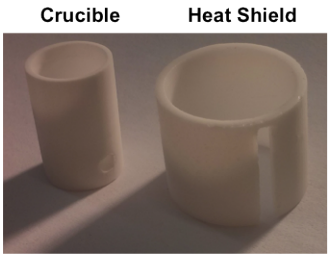

Figure 5.5: A photograph of the Crucible and Heat shield.

In Fig 5.6a the molecular evaporator without the crucible or heat shield is shown. It consists of two UHV feedthrough bars to which a filament is attached. The feedthroughs are large metal bars, as this allows them to act as support and to ensure that most of the current is dropped through the filament. The filament is

composed of a tungsten wire wrapped into a coil with the approximate diameter of the crucible. The crucible is then placed within this coil, as seen in the Fig 5.6b. In this picture, the thermocouple has also been inserted into the bottom of the crucible. Before the molecular evaporator is attached to the UHV chamber the molecules are loaded into the crucible and the heat shield is placed over the filament. The final configuration can be seen from above and from the side in Fig 5.6c and Fig 5.6d respectively.

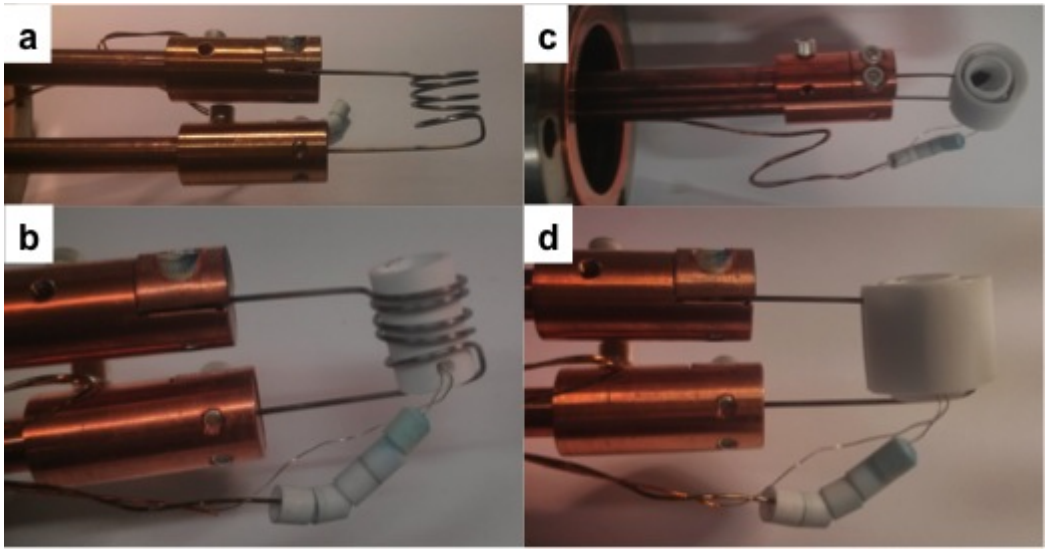

Figure 5.6: Molecule evaporator. a) shows the filament without the crucible, b) the crucible sitting inside the filament, with the thermocouple inserted into the bottom of the crucible (the heat shield has been removed). c) shows the fully assembled evaporator from the side and d) the evaporator from above.

In both the Cryogenic and Oxford STMs, the evaporation occurs in the load lock of the system to avoid contamination of the main chambers. In order to reduce the background pressure in the load lock, two changes are made to the usual method of operation. After the evaporator has been attached, the load lock is baked to 140°C (assuming this is not limited by the molecule sublimation temperature) to reduce the background pressure in the evaporator. The second change is that a TSP is added to the load lock to further reduce the background pressure. Before carrying out evaporations it is also necessary to degas the molecules. This removes impurities in the molecules and also heats up the surrounding surfaces, reducing the background pressure for future evaporations.

The exact degassing procedure varies depending on time constraints and whether it

is the first time the molecules are being used. A general procedure is to slowly (over the course of a couple of hours) bring the molecules up to approximately 25°C below the sublimation temperature, and then leave the molecules at this temperature for an hour or longer. The molecules are then heated to 10°C above the sublimation temperature for a short time ($\sim$ 5 minutes), before cooling the evaporator back down to room temperature. When carrying out an evaporation, the procedure is to quickly heat up the crucible as this reduces the temperature of surrounding areas, before stabilising the temperature and evaporating onto the sample.

Chapter 6

A Copper Nitride Nanotemplate for Individual Magnetic Molecules

6.1 Abstract

Magnetic molecules hint at a promising future in information technology applications because of their interesting quantum and magnetic bulk properties. If these molecules are to be useful for device applications, it may be necessary to place them on surfaces, and work has begun to concentrate in this area. However, the practical issues of isolating and accessing these molecules have yet to be resolved. Utilising nanoscale templates may provide a route to fulfilling these demands [116, 117]. In this chapter we show that Cu_2N islands can be used to template magnetic molecules on a surface and that the interaction with the island influences both the position and electronic properties of the molecule.

6.2 Introduction

It is important to study how the molecule interacts with the surface and how this modifies the electronic and magnetic properties of the molecule.

When a molecule is in the gas phase, it is characterised by discrete energy levels as seen in Fig 6.1a. When it couples to the surface the energy levels broaden; depending on the coupling to the surface, one of two regimes form. When the broadening of the level is below that of the energy gap of the molecule, the molecule is weakly coupled to the surface and is physisorbed. This case is seen in Fig 6.1b. The dominant force between the surface and the molecule is the van der Waals force. There is no charge transfer from the surface and the molecule is weakly bound to the surface.

In Fig 6.1c, the broadening of the levels is greater than the energy gap of the molecule and the molecule is chemically absorbed to the surface; this results in the molecular levels no longer being a good description [4]. The molecule is hybridised to the surface and therefore electrons are delocalized between the molecule and the surface, which can result in effects such as Kondo.

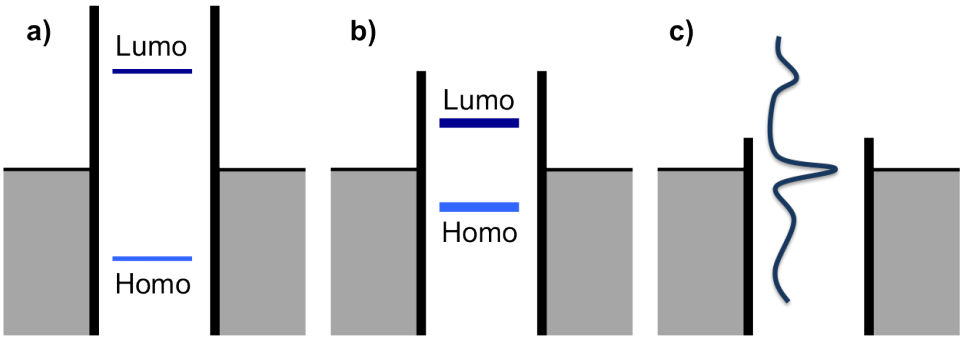

Figure 6.1: Cartoon of a molecule between two contacts. a) shows the molecule in gas phase with a distinct HOMO and LUMO, b) shows the molecule weakly coupled to the surface, and c) shows the case where the molecule is strongly coupled. [4]

In this chapter we include a brief discussion of the molecules that have been measured in this thesis (FePc and $DyPc_2$). Next, data is presented on these molecules absorbed on Cu(001) surface. Finally it is shown how magnetic molecules can be placed in a pseudo regular grid structure by utilising the Cu_2N island structure and how this affects the molecules.

6.3 Phthalocyanines

Phthalocyanine molecules are ubiquitous in modern society owing to their presence in almost 25% of organic dyes [118]. First discovered in 1907, this class of molecule

has attracted great interest due to its electronic and optical properties. Its structure is closely related to porphyrins which are biologically relevant molecules as they form the key components in many proteins. The phthalocyanine is a planar aromatic molecule, consisting of four isoindole units. The ability to place one of 70 different metal atoms in the centre allows the metal phthalocyanine molecules to have a large variety of properties [118]. Phthalocyanine molecules have been used as active components in electronic devices [118] and have even begun to be used in oncology [119]. MPc molecules may have applications in spintronic [120] and quantum computing applications [121].

Phthalocyanine molecules contain a ring of 16 alternating carbon and nitrogen atoms and two free nitrogen bonds. This results in a ring with 18 electrons delocalised over it and an overall charge of -2; in order to passivate the ring it is necessary to add a +2 charge to the centre. The simplest option is for the inner cavity bonds to bind to hydrogen forming H_2Pc. There is no reason for the H atoms to bond preferentially to one pair of nitrogen atoms and Hydrogen tautomerization has been observed with STM [122]. Alternatively a transition metal can be placed in the central cavity to bond with the Pc molecule. In the case of a 4f ion, where the ion has a 3+ state, two Pc molecules bind with the 4f ion forming a sandwich with a overall charge of -1. This results in a delocalised electron over the Pc rings in the molecule [123].

The high thermal stability of phthalocyanine molecules means that they are easily sublimed onto a surface. CuPc was amongst the first molecules to be observed individually by STM [124]: the molecule sits planar to the surface, allowing for STM measurements of the central metal atom. The structure of MPc molecules on the surface has been extensively studied [125, 126]. In this thesis we investigate two Pc molecules, the structures of which are seen in Fig 6.2: FePc, a single ring molecule where the Fe atom sits at the centre of the ring, and $DyPc_2$, where the Dy atom sits between the two Pc rings.

Iron Phthalocyanine

FePc is chemically similar to iron porphyrin, a key component in haemoglobin, and has an interesting $S = 1$ ground state. The central Fe^{2+} ion has a square planar ligand field. Calculations agree on an $S = 1$ spin state as the $d_{x^2-y^2}$ orbital is heavily disfavoured due to the N atoms in the Pc ring. However the ordering of the remaining

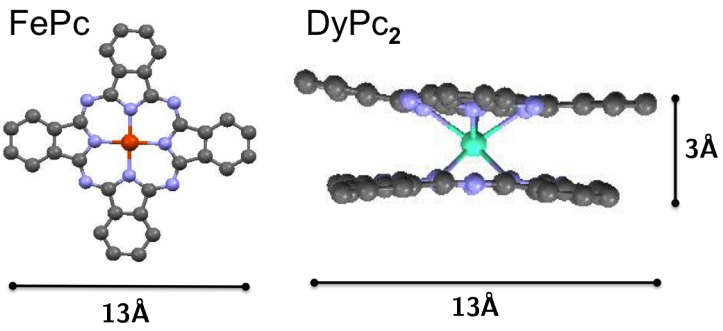

Figure 6.2: The chemical structure of FePc [127] and $DyPc_2$ [128], where dark grey atoms are C and blue atoms are N.

levels and therefore the ground state is still an open question [129–131].

When FePc is placed on Cu(111) it is seen to bind more strongly than on Au(111) [132]. FePc on Au(111) is seen to show a Fano line shape which is indicative of a Kondo effect [49, 52]. However, the Kondo temperatures stated in these papers is in disagreement. No Kondo feature was observed for FePc on Ag(001) [133].

FePc has been measured on the thin insulator CuO [8]; spin excitations measurements suggest FePc has a S=1 spin state, agreeing with other measurements [134]. It is also observed that the anisotropy of the spin is dependent on the binding angle of the molecule on the surface. The growth of FePc, when decoupled by NaCl [132,135] or on multiple layers [136, 137] has also been studied.

Bis(Phthalocyaninato) Dysprosium

$DyPc_2$ is a single molecule magnet due to the anisotropy of the 4f states [138]. The magnetic moment of the central Dy atom is J = 13/2 [139]. In the gas phase of the molecule there is a delocalised electron on the ring; investigations via STM show the molecule sitting planar to the surface [20]. Most STM investigations of lanthanide based double deckers ($LnPc_2$) molecules have concentrated on $TbPc_2$ as this has a greater anisotropy. As the 4f ions are similar, except for the contraction of the 4f states due to the increased nuclear charge, the results should be applicable to our investigations.

STM investigations of $TbPc_2$ and YPc_2 on Au(111) show a Kondo resonance due to the ligand spin [53]. When $TbPc_2$ is placed on Ir(111) it is seen that the upper

Pc ring can be induced to rotate in regards to the lower Pc ring, resulting in a chirality [140]. In all these measurements, due to the weak coupling between the surface and the molecule, there is little interaction between the surface and the 4f states [141]. Recently it has been shown that for $NdPc_2$ it is possible to interact with the 4f states when the molecule is placed on Cu(001) [142].

6.4 FePc on Cu(001)

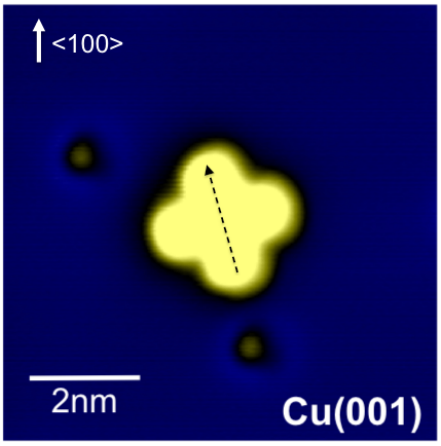

Figure 6.3: STM image of FePc on Cu(001) ($V_{set} = -1.0$V, $I_{set} = 0.1$nA).

Figure 6.3 shows an STM image of FePc on Cu(001). The sample was prepared by subliming the FePc at 350 °C onto a Cu(001) sample sitting at room temperature. It is observed that the FePc molecule binds at ±18° from the [100] azimuth (Fig 6.4) [143, 144]. The angle of the surface was calculated using the growth directions of Cu_2N island structures. The small distribution of angles suggests the molecule is strongly coupled to the surface. This is also shown by spectroscopy data taken over the centre of the FePc molecule on Cu(100) as seen in Fig 6.5; no clear features are observed in the LDOS, demonstrating that the molecular orbitals are hybridised with the surface.

Low bias spectra taken over the centre of a FePc molecule show a Fano line shape. This has been observed before for FePc on Au(111), and is indicative of the Kondo effect where the magnetic moment is screened by the conduction electrons [49, 52]. In this figure the spectra has been fitted with Fano line shape equation as detailed in Chap 3; the resonance has a width of 22mV. This is of a similar order to previous

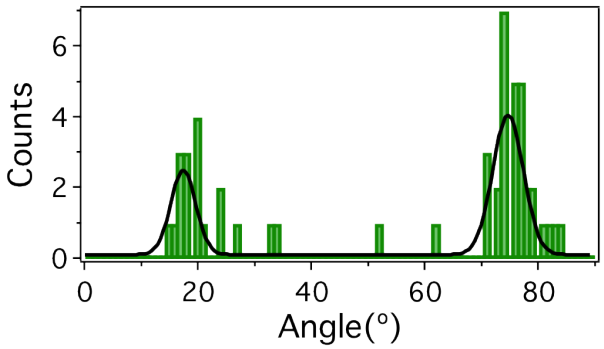

Figure 6.4: Histogram of the binding angle of FePc on Cu(001). The molecule is observed to bind at ±18° from the |100| crystal axis.

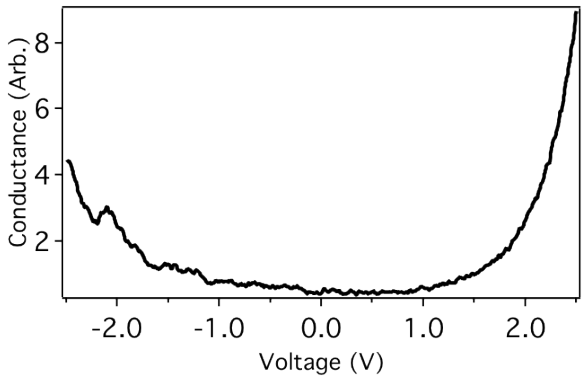

Figure 6.5: Spectrum taken over the centre of FePc. No distinct features are observed due to the interaction of the FePc with the Cu(001) surface. ($V_{set} = -2.5$V, $I_{set} = 0.5$nA)

measurements [49,52] on Au(111). Kondo is not observed on Ag(001), and this result is explained as being due to a stronger interaction with the substrate. A systematic study of Co on different substrates [145], shows a similar Kondo temperature for Au(111) and Cu(001), and a lower temperature for Ag(001). This result, which fits the trend observed for FePc, can be explained using a simplified Anderson model; the interaction with the surface modifies the d- level occupation and this results in the Kondo temperature following a parabolic dependence [145].

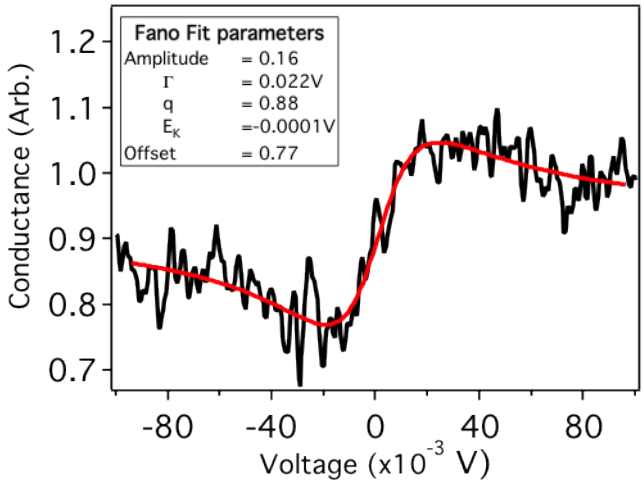

Figure 6.6: Spectrum over the centre of FePc on Cu(001). A Fano line shape has been fitted to the data. The width of the feature is similar to previous measurements on Au(111) [49, 52]. ($V_{set} = -0.1$V, $I_{set} = 1$nA)

6.5 $DyPc_2$ on Cu(001)

In Fig 6.7, an STM image of $DyPc_2$ on Cu(001) is shown. The $DyPc_2$ molecules were prepared by Michael Waters in the group of Joris van Slageren. The full details of their synthesis can be found in the appendix. $DyPc_2$ was evaporated at 350°C onto clean Cu(001) sitting at room temperature.

In topographic images of $DyPc_2$ on the Cu(001), an eight-lobe structure is observed as seen in Fig. 6.7. The close match of the image to the simulated free Pc molecule [141] suggests the upper Pc molecule is only weakly coupled to the surface. However as discussed in Chap 9, where the coupling of the 4f state to the metal surface is investigated, this simple picture turns out to be incorrect in this case.

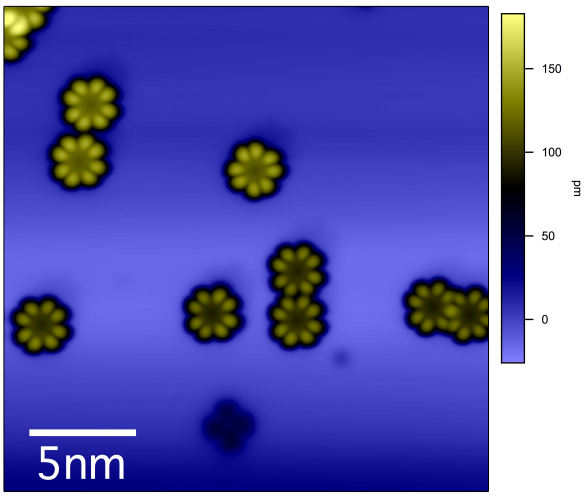

Figure 6.7: STM image of $DyPc_2$ molecules on Cu(001) (V_{set}=-0.7V, I_{set}=0.1nA).

A cross-structure is sometimes observed due to $DyPc_2$ degrading during the evaporation process. The number of crosses is very low; for some sample preparations no crosses are observed. The crosses could be one of many configurations; a Dy atom sitting above, in or below the Pc ring, or a Pc ring without a Dy atom. Voltage dependent images of the crosses are shown in Fig 6.8, where it can be seen that the molecule appears to have a bright spot at the centre at low bias and a depression at high bias. This makes identification of the type of cross difficult.

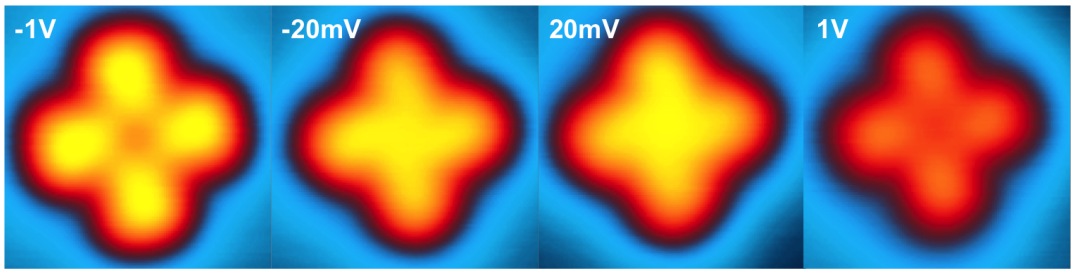

Figure 6.8: Bias dependent images of a single ring Pc molecule (I_{set} = 100 pA).

In Fig 6.9 data for a single pthalocyanine cross is shown. Both the dI/dV slice and the dI/dV spectroscopy clearly show that the Fano line shape is only present at the centre of the cross, and is not present in the ligands of the molecule. Similar behaviour has been observed for TbPc on Au(111) and is due to the 4f states in Tb interacting directly with the conduction electrons [20], suggesting this cross retains the Dy ion.

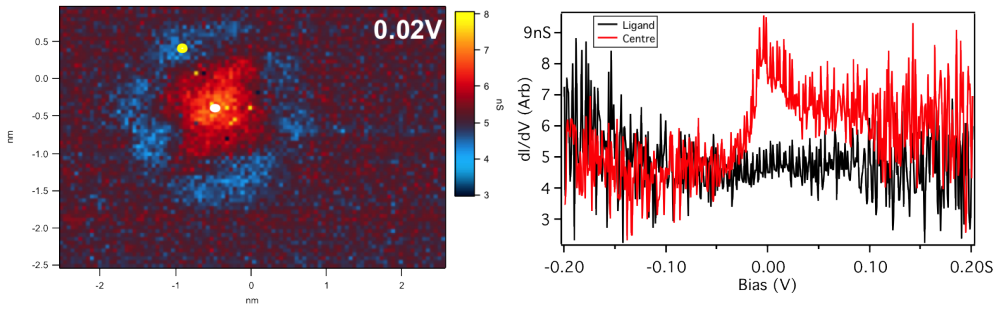

Figure 6.9: dI/dV slice at 0.02V over a single Pc cross. At the centre a Fano line shape is observed, which is not present on the ligand. Dots on dI/dV slice show position of spectra. ($V_{set} = -0.1$V, $I_{set} = 1$nA)

6.6 Templating by using Cu_2N Island structure

Copper nitride islands have been used to template both porphyrin (Fig 6.10) [112] and fullerene [113] molecules, as well as atomic iron and copper [111].

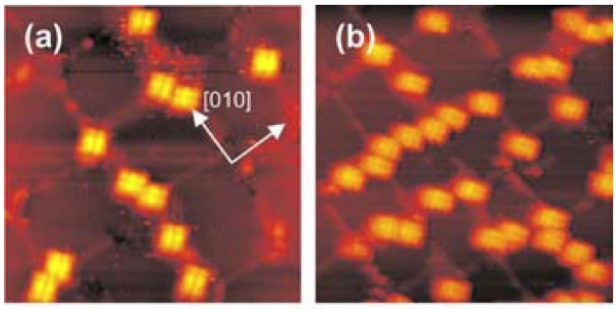

Figure 6.10: Porphyrin molecules evaporated onto the copper nitride structure. The molecules stick preferentially to the copper over the nitride [116].

Figure 6.11 shows FePc and $DyPc_2$ on a $Cu_2N \times Cu(001)$ lattice when the molecules are sublimed onto a room temperature substrate. It can be clearly seen that the molecules sit only at the intersection of the Cu lines. Due to the quasi-regular size of the islands this creates a large scale array of magnetic molecules on the surface. As seen in Fig 6.12 we observe a binding angle of $\pm 18°$, suggesting the molecule binds to the surface in a similar way as to the bare Cu surface.

Why the molecules sit only at the intersection of the copper lines is an open question. In the work by Ecija *et.al.* it is suggested that the molecules bind due to van der Waal's forces, and there are stronger van der Waal's forces between copper and

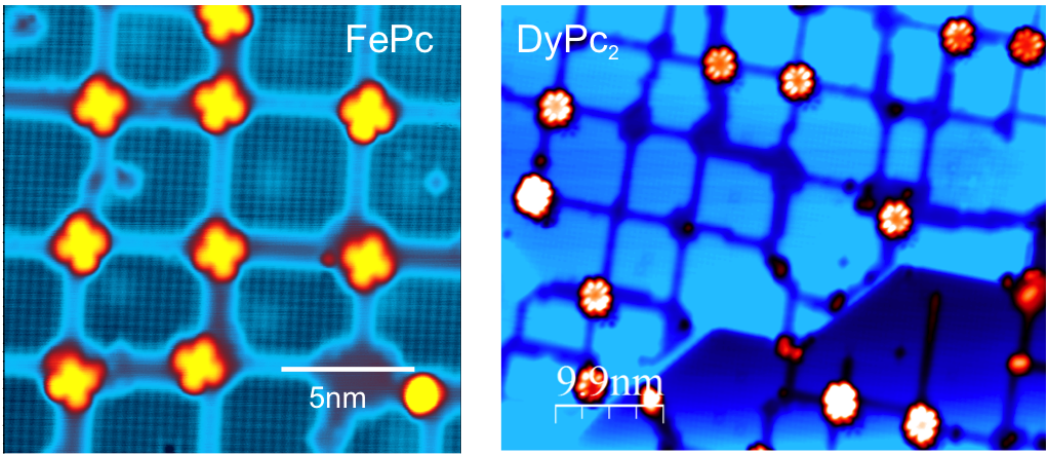

Figure 6.11: STM images showing how the molecules sit at the intersections of the copper lines on the $Cu_2N \times Cu(001)$ lattice. (STM image V_{set}=-1V, I_{set}=0.1nA)

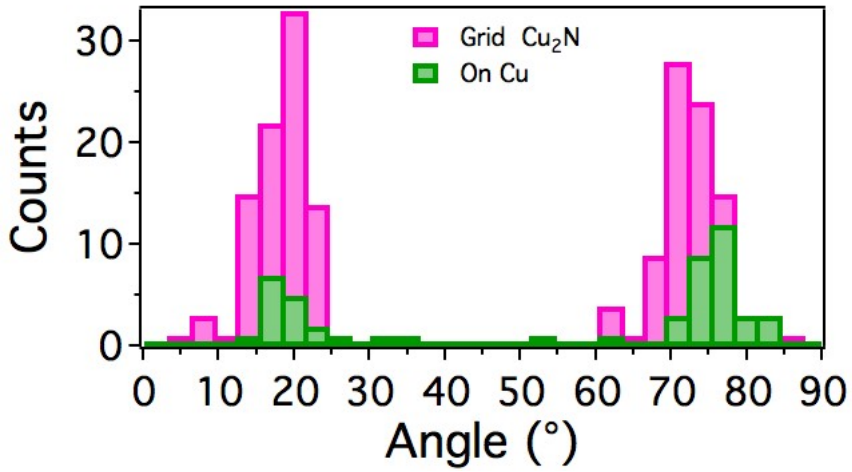

Figure 6.12: Histogram showing the distribution of binding angles for FePc molecules on the $Cu_2N \times Cu(001)$ lattice with respect to the |100| axis. The molecule is observed to bind at $\pm 18°$, which is the same as on bare Cu(001).

porphyrin than between copper nitride and porphyrin [112]. On a surface with a low coverage of islands as shown in Fig 6.13, the $DyPc_2$ sits at the corners of the Cu_2N islands even when large areas of copper are present. This suggests that the molecules preferentially stick to the corners of the Cu_2N islands.

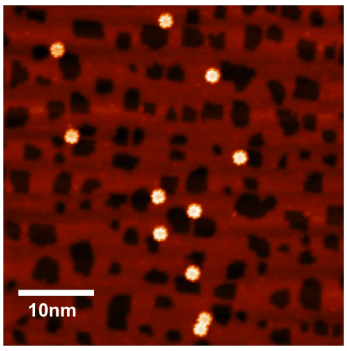

Figure 6.13: When the coverage of Cu_2N islands is reduced it is seen that all the $DyPc_2$ molecules stick at the corners of the Cu_2N islands (V_{set}=-2.0V, I_{set}=0.1nA).

One explanation as to why the molecules stick to the edges of the Cu_2N islands is that it is due to the difference in work function between the Cu_2N and the Cu [117]. Using I(z) the work function over copper is measured to be 4.6eV and over Cu_2N 5.5eV [146]. Therefore the electric field between Cu and Cu_2N likely polarises the molecules causing them to stick to the edges.

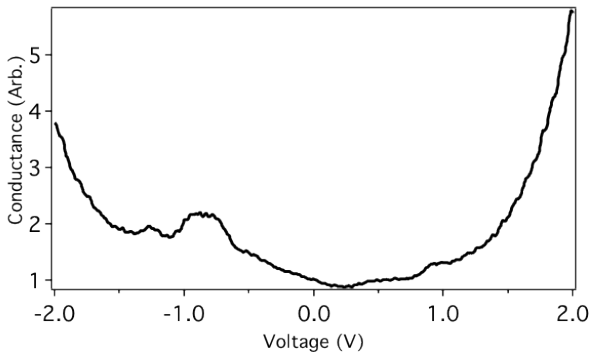

Figure 6.14: Spectroscopy measurement of a FePc molecule at the intersections of Cu_2N island; more features in the spectroscopy are observed than for FePc on bare Cu(001) (V_{set}=-2V, I_{set}=0.5nA).

Spectroscopy measurements on FePc molecules sitting at the edges of the Cu_2N show features at both positive and negative bias; this suggests FePc at the edges of the Cu_2N are less coupled than on Cu. This is surprising as FePc binds at the same

angles as on Cu(001), suggesting the coupling to the surface is similar. This result shows that the Cu_2N islands not only affect the position of the molecules but also their electronic structure.

6.7 Conclusion

In this chapter we demonstrated that magnetic molecules can be placed in a pseudo-grid array through the use of Cu_2N islands. This spatial separation restrains any potential dipolar or exchange interaction between the molecules, and it allows for individual, independent spins to be addressed. The molecules preferentially stick to the corners of the islands, suggesting that there is an electric field on the edge of the islands which polarises the molecules. FePc molecules next to the Cu_2N, compared to bare Cu(001), show more distinct features in their density of states. This suggests that although the molecules appear to bind in a similar manner to the Cu, the interaction with the edges decouple the molecules in comparison to Cu.

6.8 Future work

Detailed low bias spectroscopy on the differences between FePc on Cu and at the corners of Cu_2N may yield information on whether the magnetic properties of the molecule are also affected.

We would like to be able to conclusively show why the molecules stick at the corners of the Cu_2N. One possibility is to carry out DFT calculations. Although it would not be possible for a calculation to include a molecule, modelling a single boundary of Cu_2N and Cu may show what the surface potential looks like.

An experimental answer might be provided using AFM. One experiment we have tried with AFM is to map out the the force field that the tip experiences above the surface [147]. The AFM was operated in frequency modulation mode, which is the method of choice in experiments which measure forces at the atomic scale [148]. Here the cantilever is oscillated at its resonant frequency [149] and the force gradient is detected as shifts in the frequency of the cantilever.

Figure 6.15 shows a map of the potential energy experienced by a tip over the corner of a Cu_2N island [150]. Here it is observed that the tip interacts with the Cu_2N less than the Cu. Drawing definitive conclusions from this data is proving difficult as there are many competing effects at this scale.

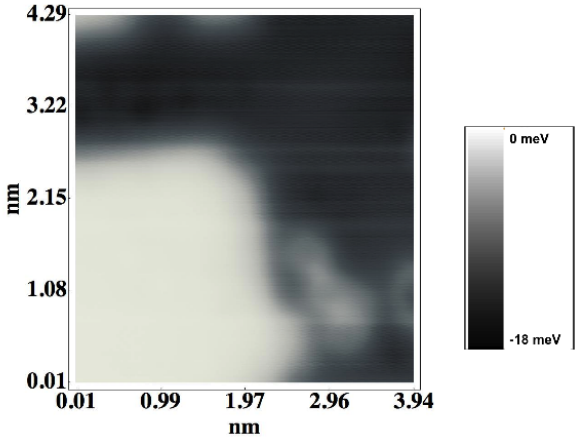

Figure 6.15: Potential map of the corner of a Cu_2N island on Cu(001); the potential energy between tip and Cu_2N is lower than the potential energy over Cu. [150]

With AFM it has been shown that it is possible to measure the force required to move an atom laterally on a surface [151]. In our experiment it was not possible manipulate to the FePc molecule on the surface. However it may be possible to use either a metal atom or CO molecule as a probe and see if there is an asymmetry in the force required to move the atom or molecule when bound next to a Cu_2N island.

Chapter 7

Controlling the properties of a magnetic molecule through the local atomic environment

7.1 Abstract

The inevitable march towards atomic scale devices will likely include the use of the functional molecules as replacements for conventional electronic components. Including a spin on the molecule through a metal atom or an organic radical may allow for the creation of spintronic devices. Work has mainly concentrated on the finding molecules with appropriate properties; however it may be necessary to electrically contact these molecules and the effect of this is not well understood. Therefore it is of key importance to understand the influence of the contacts on both the electronic and magnetic properties of the molecule.

Here we show that the local atomic environment plays a defining role for both the electronic and magnetic properties of the molecule. For FePc on a copper nitride monolayer the coupling is defined by the binding site and this affects the density of states of the molecules. The difference is observed in both imaging and spectroscopy data. Data is also shown which provides evidence that the coupling of the spin to the surface is also controlled by the binding site. This work demonstrates the importance of the understanding the atomic scale geometry of contacts with molecules if viable

devices are to be created.

7.2 Introduction

If molecules are to be used to create atomic scale devices, then it may be necessary to decouple them from the surface interactions. Previous work on single molecules has shown that this allows for the measurement of the molecular structure, vibronic states, and spin excitations [8, 40, 109]. Molecules can be decoupled from surface interactions due to inter molecular binding with other molecules [136, 152]. Another method is to sublime multiple layers, where the first layer can act as a decoupling layer [75]. Thin insulators, such as NaCl [40] and CuO [8], have also been used to decouple molecules. In this thesis Cu_2N is used to decouple the molecules as it has a simple atomic structure [114] and has been used previously to decouple metal atoms [6]. A Cu(001) sample was prepared as detailed in Chap 5. A Cu_2N monolayer was prepared on top of clean Cu(001) samples by sputtering with N_2 and annealing to 350°C. FePc molecules were sublimated for 20s at 350°C onto a room-temperature sample.

7.3 Effect of binding geometry

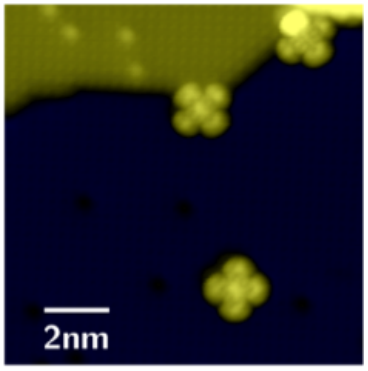

Figure 7.1: FePc molecules on a Cu_2N monolayer ($V_{set} = -2$V, $I_{set} = 0.1$nA).

Figure 7.1 shows an STM image of FePc on a Cu_2N monolayer. FePc is observed to bind at $\pm 18\,^\circ$, $0\,^\circ$ and $45\,^\circ$, this is different to Cu(001) where only $\pm 18\,^\circ$ was observed. As seen in Fig 7.2 the distribution of angles is much greater than that seen on the

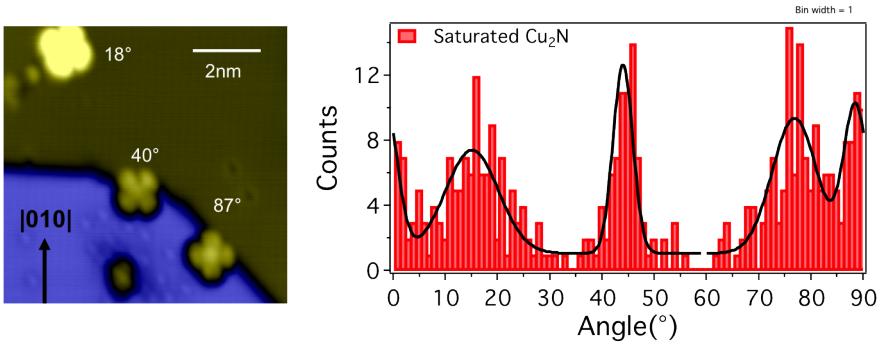

Figure 7.2: Binding angle of FePc on Cu_2N. Peaks are seen at $\pm 18\,^\circ$, $0\,^\circ$ and $\pm 45\,^\circ$ (STM image, $V_{set} = -2$V, $I_{set} = 0.1$nA).

Cu(001) surface (Fig 6.4). This suggests that the molecules are coupled more weakly to the surface. DFT calculations on FePc molecules on the Cu_2N monolayer show that there is little difference in the binding energy between different binding angles (see Appendix).

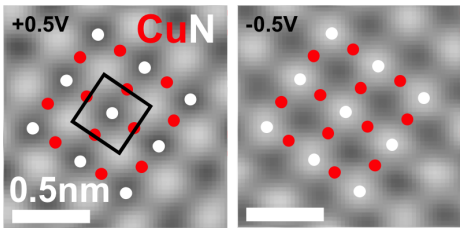

Figure 7.3: The atomic lattice of Cu_2N can be resolved in STM measurements. At +0.5V the hollow sites appear bright, whereas the nitrogen sites are bright at -0.5V. [114]

Previous work on Cu_2N has shown that it is possible to resolve the atomic lattice of the surface [114]. As seen in Fig 7.3, at +0.5V the hollow sites are bright and at -0.5V the nitrogen sites are observed to be bright. This allows for the binding site of a molecule or atom to be assigned. As shown in Fig 7.4, molecules are observed to bind on Cu and N sites; no molecules are observed to bind to the hollow site. We do not see a difference in binding angle between Cu and N site molecules (Fig 7.5).

Spectroscopy over two molecules is shown in Fig 7.6, one for each binding site. In both the high bias range (-2.5V $\rightarrow$ 2.5V) and low bias range (-0.05V $\rightarrow$ 0.05V), a difference is observed in spectra acquired over the centre of the molecules on the two binding sites. Molecules on a N site show inelastic steps in low bias spectroscopy

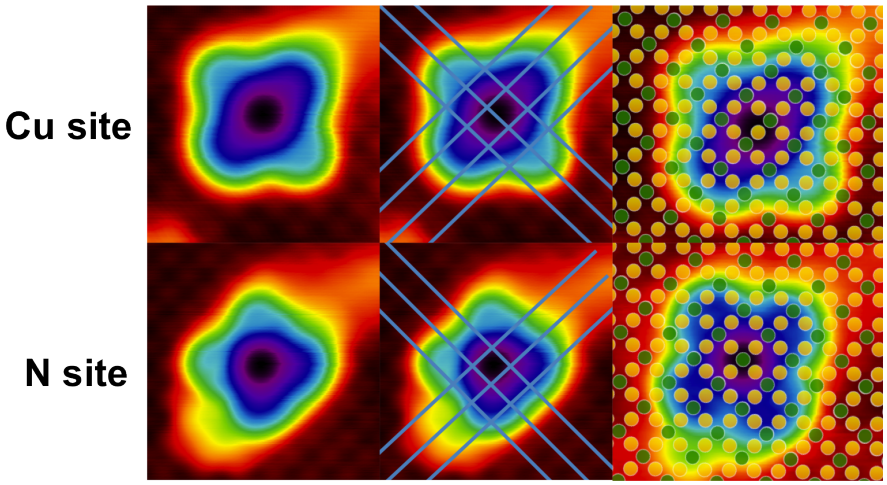

Figure 7.4: FePc is observed to bind over the nitrogen and Cu site. Here the assignment is shown through overlaying a lattice and drawing lines through hollow sites ($V_{set} = 0.5V$, $I_{set} = 1nA$).

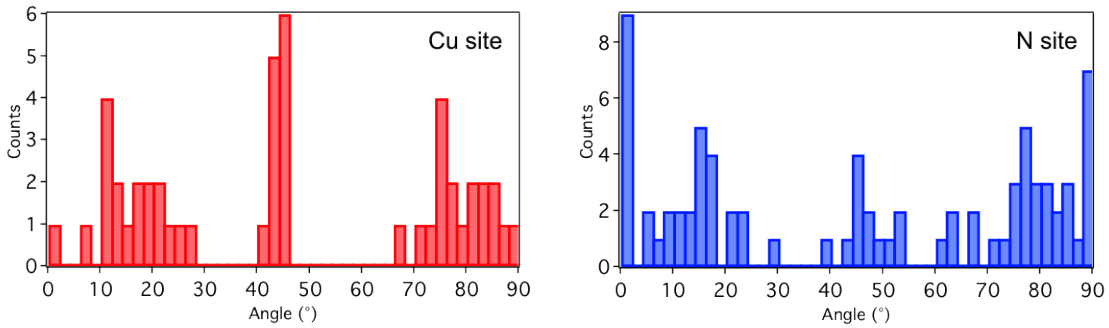

Figure 7.5: FePc binding angle by binding site. We observe molecules at all four binding angles for both Cu and N sites.

and peaks in high bias spectroscopy. Molecules on a Cu site show a Fano-like feature at the Fermi energy spectroscopy and less well defined peaks in high bias spectroscopy.

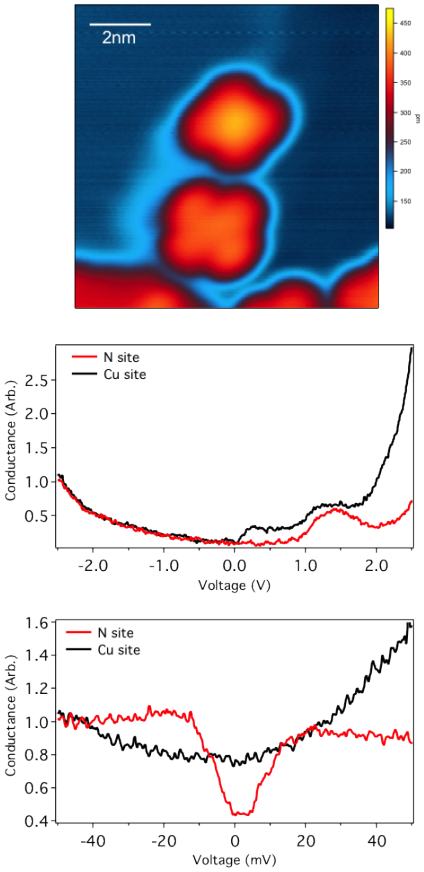

Figure 7.6: Spectroscopy measurements taken on molecules shown in STM image ($V_{set} = -2.5$V, $I_{set} = 0.1$nA). The lower molecule in the STM image is on a copper site and the upper molecule on a nitrogen site. On the Cu site (black), a Fano line shape and less well defined features in LDOS are observed suggesting it is coupled to the surface. On the N site (red), we observe spin excitation steps suggesting it is decoupled from the surface (HV spectra $V_{set} = -2.5$V, $I_{set} = 0.1$nA; LV Spectra $V_{set} = 0.1$V, $I_{set} = 1$nA).

Inelastic spectroscopy typically is only observed on decoupled molecules, and a Fano-like line shape is indicative of Kondo screening, which is a sign of strong coupling. This suggests the level of degree of decoupling varies depending on binding site on the Cu_2N; this has not been observed in previous works for molecules on thin insulators [8, 40, 109, 132, 153].

Within both classes of molecules there is substantial variation in the measured spec-

tra as seen in Fig 7.7 and 7.8. This may be due to the atomic environment on which each molecule sits i.e step edges and defects. Alternatively it could be due to a variation in coupling across the Cu_2N monolayer [154].

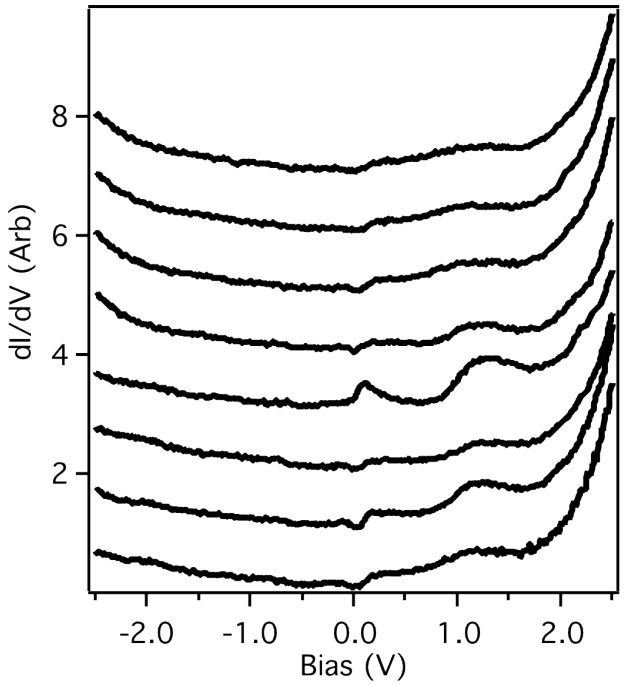

Figure 7.7: High voltage spectroscopy on different FePc on Cu sites. For FePc on a Cu site, we observe a Fano line shape at 0V, however there is a variation between molecules. Spectra have been offset for clarity ($V_{set} = -2.5$V, $I_{set} = 0.5$nA).

A difference in topographic images is observed between FePc molecules on a Cu site and on a N site. For N site molecules, although each molecule images slightly differently, no change is observed between ± 0.5V. For Cu sites a distinct change is observed between ± 0.5V, and at negative bias an asymmetry is observed.

Fig 7.11 shows topography of FePc on Cu sites bound at 45 °, 0 °, and 18 ° at negative bias. For 0 °, 45 °, the molecules are roughly symmetric. For 18 °, a chirality is observed. This behaviour is similar to that observed for CuPc on Ag(001) [108]. In that work it is observed that the charge transfer from the surface to the molecule is asymmetric due to the molecules binding at ± 18 °. This produces chirality in negative bias image, but does not effect the positive bias image.

This suggests that for FePc molecules bound to the Cu site, the molecule is hybridised with surface. For molecules bound at 0 ° and 45 °, the interaction is close

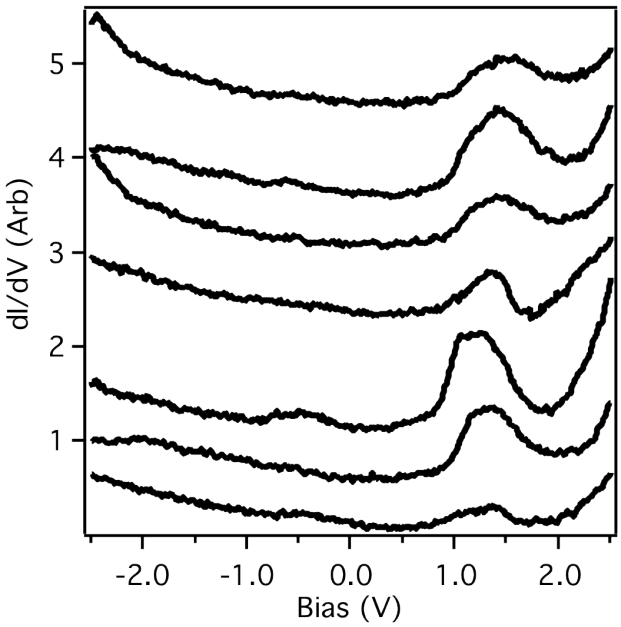

Figure 7.8: A comparison of high voltage spectroscopy taken over the centre of different FePc on N sites. Spectra have been offset for clarity ($V_{set} = -2.5$V, $I_{set} = 0.5$nA).

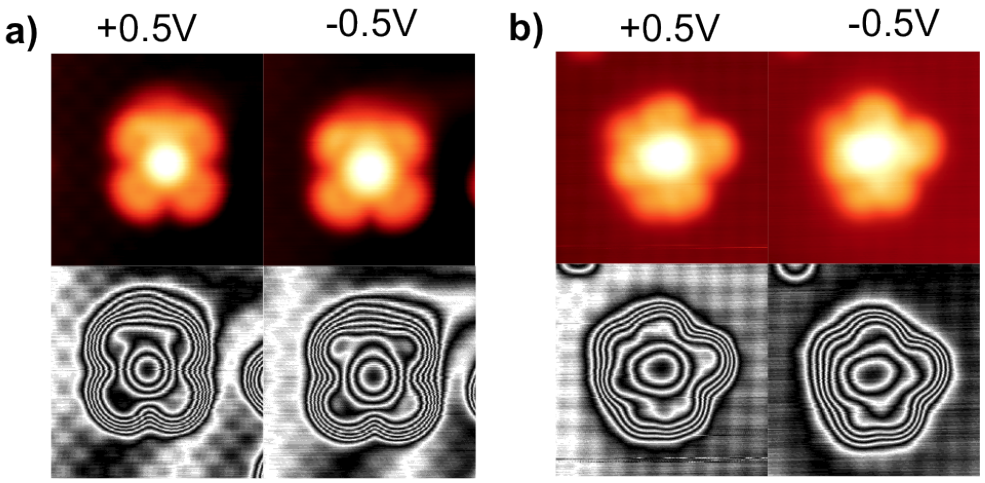

Figure 7.9: STM images of Nitrogen site at both positive and negative bias. Although both molecule a) and b) image differently no great change is observed between the two images (a) $I_{set} = 0.5$nA, b) $I_{set} = 1$nA).

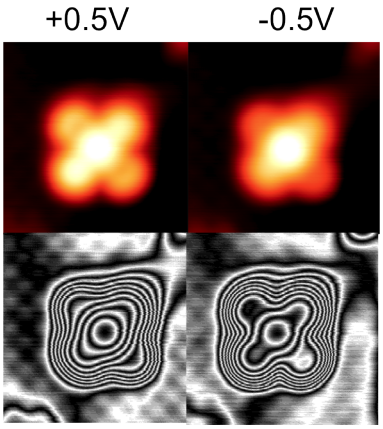

Figure 7.10: STM images of Cu sites. A difference is observed between positive and negative bias ($V_{set} = -0.5$V, $I_{set} = 0.5$nA).

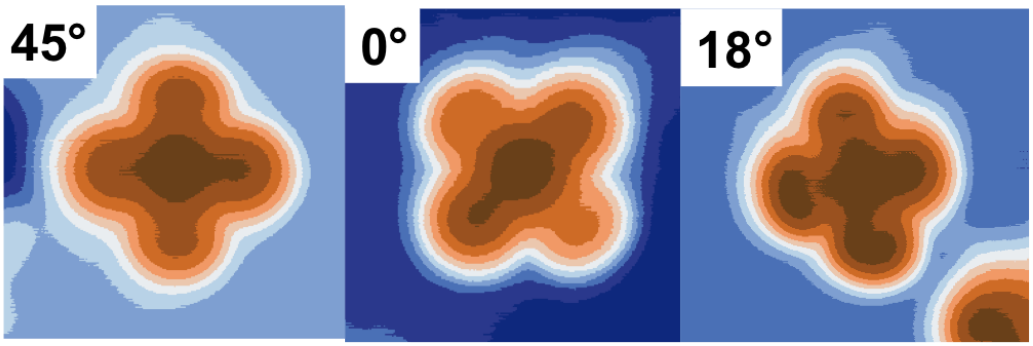

Figure 7.11: FePc on Cu sites at 45 °, 0 °, and 18 ° at negative bias. An asymmetry is observed for 18 ° ($V_{set} = -0.5$V; left and right $I_{set} = 1$nA, centre $I_{set} = 1$nA).

to symmetric and therefore the change in electronic structure is observed but the symmetry is not broken. For molecules bound at 18 °, the symmetry is broken by the binding angle and this creates the asymmetry observed at negative bias. This suggests that the FePc molecule on a Cu site is coupled to the surface more strongly than when FePc is situated over a N site.

As seen in Fig 7.12, low voltage spectroscopy measurements for FePc on Cu show a sharp rise in conductance close to the Fermi energy, which we ascribe to a Fano line shape created by the Kondo effect. That Kondo is observed for FePc bound over a Cu site shows that the Fe spin is coupled to the surface.

It is difficult to conclusively show that the line shape is due to a Kondo resonance as the energy scale is too high to show the expected increased broadening of the line width with temperature and we observe no change in the spectra when a magnetic field is applied. The width $\Gamma = 120$mV is higher than that observed for FePc on Cu(001) (see Fig 6.6). This is a surprising result, given that Cu_2N is considered a thin insulator. The energy of the Kondo resonance is $E_k = 77$mV, which is much larger than observed for FePc on Au(111) [49, 52]. We are currently working with collaborators to either provide further evidence of the Kondo effect, or to provide an alternative explanation for the line shape.

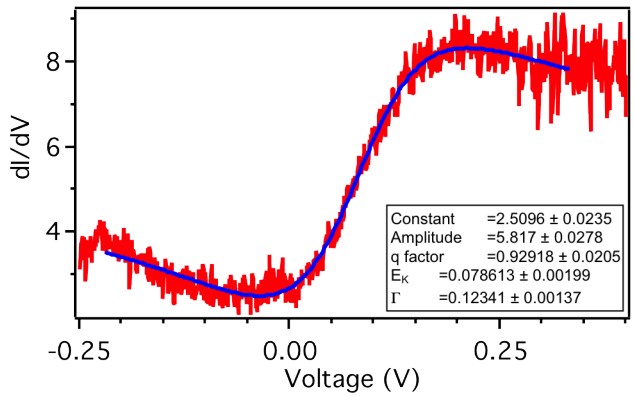

Figure 7.12: Spectroscopy over on FePc over a Cu site. A Fano line shape has been fitted to the data ($V_{set} = 0.4$V, $I_{set} = 0.75$nA).

For FePc molecules bound over a Cu site, it appears that the molecule is not decoupled but strongly interacting with the substrate. The effect of this interaction is observed in high voltage spectroscopy where the levels are broad and features less distinct. It is also observed in negative bias imaging, where an asymmetry is

created through the binding angle. This demonstrates that although the binding site dominates the overall properties of the molecule, the interaction of the ligands with the substrate also plays a role. That a Fano line shape is observed is indicative that the magnetic moment is interacting with the substrate.

From DFT calculations, shown in Fig 7.13, it is not immediately obvious why the binding site plays the defining role. One notable difference between the two binding sites is that for FePc over the Cu site the Fe atom is at the centre of the molecule, but over the N site the Fe atom is pulled downwards. The effect of this change is not yet fully understood.

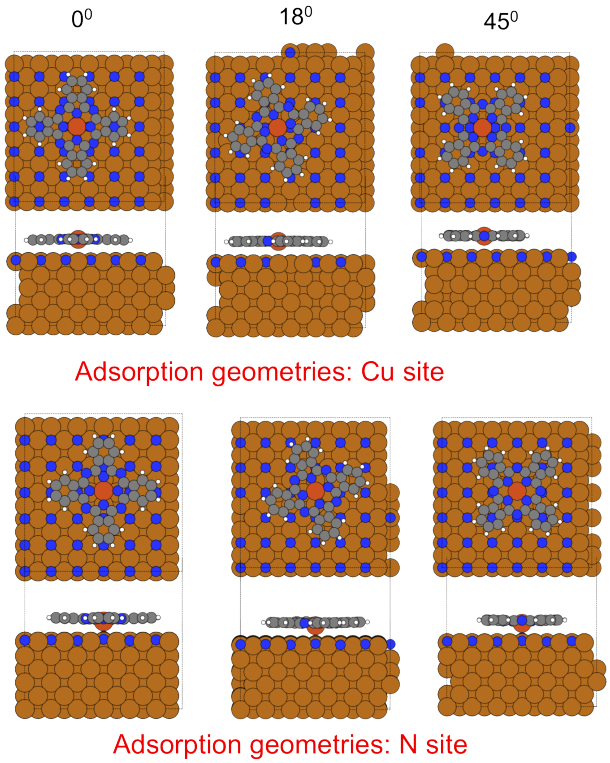

Figure 7.13: DFT calculations for Cu and N binding sites for FePc for the binding angles $\pm 0\,^{\circ}$, $18\,^{\circ}$, and $\pm 45\,^{\circ}$. For N binding sites the Fe atom is seen to be pulled down towards the Cu_2N surface. Details of the calculations are included in the Appendix.

7.4 Magnetic properties

As seen in Fig 7.14, molecules bound on a nitrogen site show inelastic steps. In other systems these steps have been shown to have been caused by spin, rotational or vibrational excitations [67, 69, 155, 156]. For FePc on CuO, spin excitations are observed [8]. In spin excitation spectroscopy, the tunnelling electrons excite the spin from the ground state to an excited state (unless spin pumping occurs [57]), losing energy in the process.

Spin excitations can only occur between states which differ by $m_s = \pm 1$ due to selection rules. FePc is calculated to have S=1 [129–131]. For an S=1 spin, with no transverse anisotropy ($E = 0$) and B=0T, we would expect only one step (for $D > 0$, $0 \rightarrow \pm 1$; while for $D < 0$, $\pm 1 \rightarrow 0$). If transverse anisotropy is added ($E > 0$), this mixes the states and therefore a 2nd step can occur. Two steps are observed for FePc on CuO, suggesting S=1 with transverse anisotropy, the size of which was affected by binding angle.

Figure 7.14 shows measurements on different FePc molecules on the Cu_2N monolayer; spectra showing one, two and three steps are all observed. The number of steps and energy of the steps is not seen to depend on binding angle. The presence of a third step, if a spin excitation, suggests that the magnetic properties of FePc on Cu_2N vary significantly from CuO, as three steps can not be explained using a S=1 model.

In Fig 7.15, field dependent measurements are shown for two molecules which show two steps and three steps respectively. The first and second step are observed to move with field, demonstrating that these are spin excitations. It is not possible to distinguish whether or not the third step shifts with field.

Spectroscopy measurements were taken across the 'three' step molecule in order to look at the spatial variance. In Fig 7.17a, three spectra are shown, over the centre, over the arm and halfway between. As we move from the centre to the edge, the intensity of each step becomes less, but the energy of the step remains constant. The intensity of each step is plotted in Fig 7.17b. We observe that each step shows the same spatial variance. This suggests that all three steps are a result of the same process, suggesting the third step is a spin excitation.

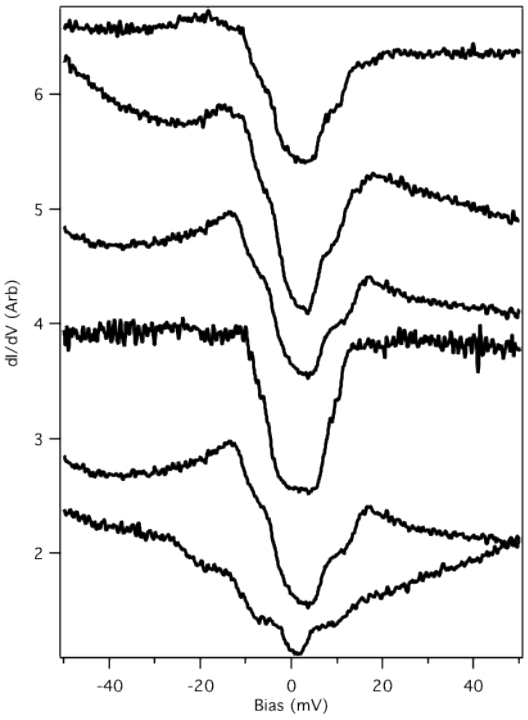

Figure 7.14: Spin excitation measurements on different FePc molecules on Cu_2N. The spectra have been offset for clarity. A large degree of variation both in the number of steps and in the energy at which the steps occur is observed. (V_{set} = 50mV, I_{set} = 1nA)

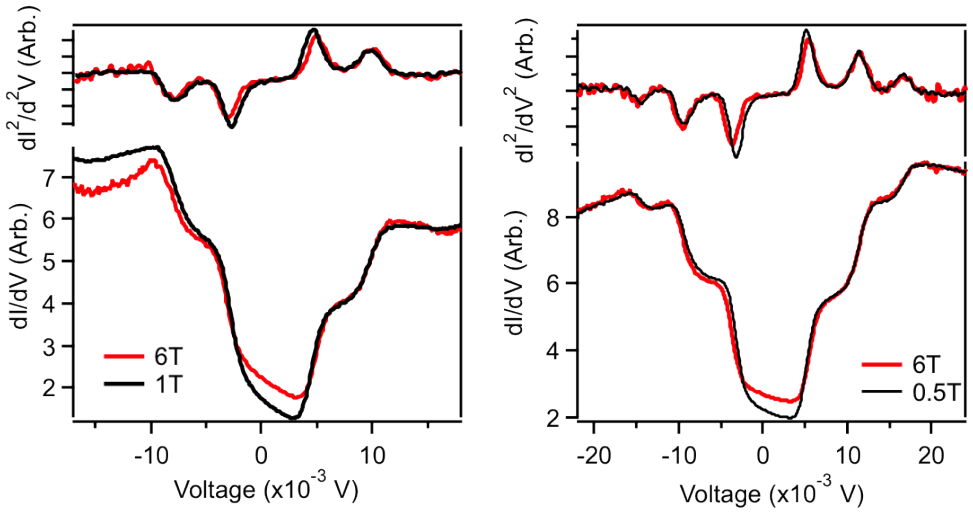

Figure 7.15: Spin excitation measurement on FePc at different magnetic fields. Two molecules are shown, one in which two steps are observed, the other three steps. For both molecules the first two steps are seen to move with field (left, V_{set} = 17.5mV, I_{set} = 0.75nA; right, V_{set} = 22.5mV, I_{set} = 2nA).

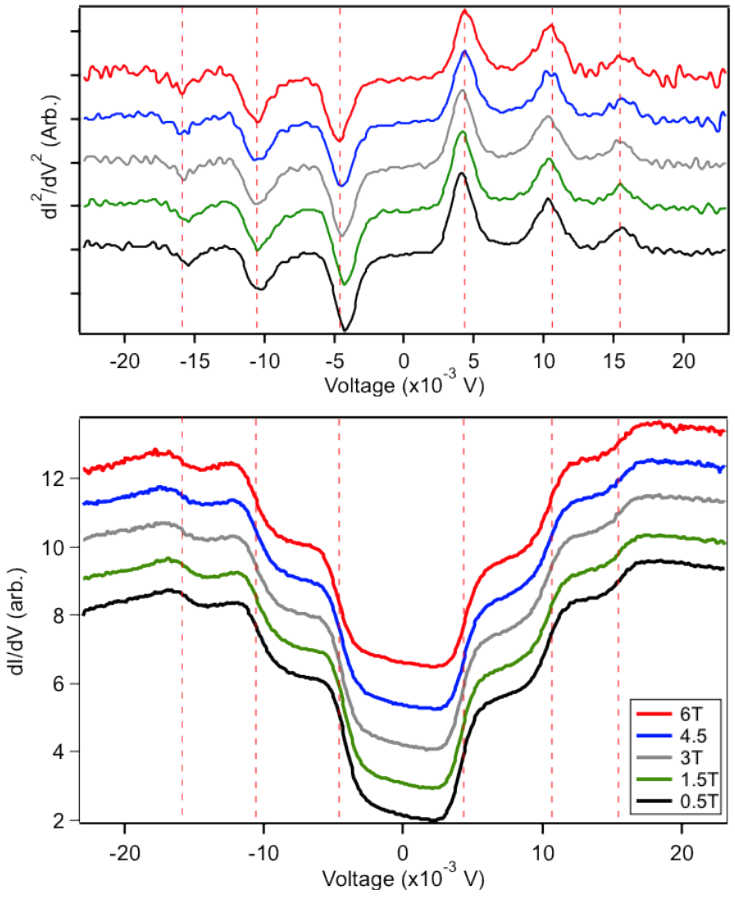

Figure 7.16: Full field dependence of 'three' step molecule. The top graph shows numerically differentiated dI^2dV^2, the bottom graph shows dI/dV spectra, (V_{set} = 22.5mV, I_{set} = 2nA).

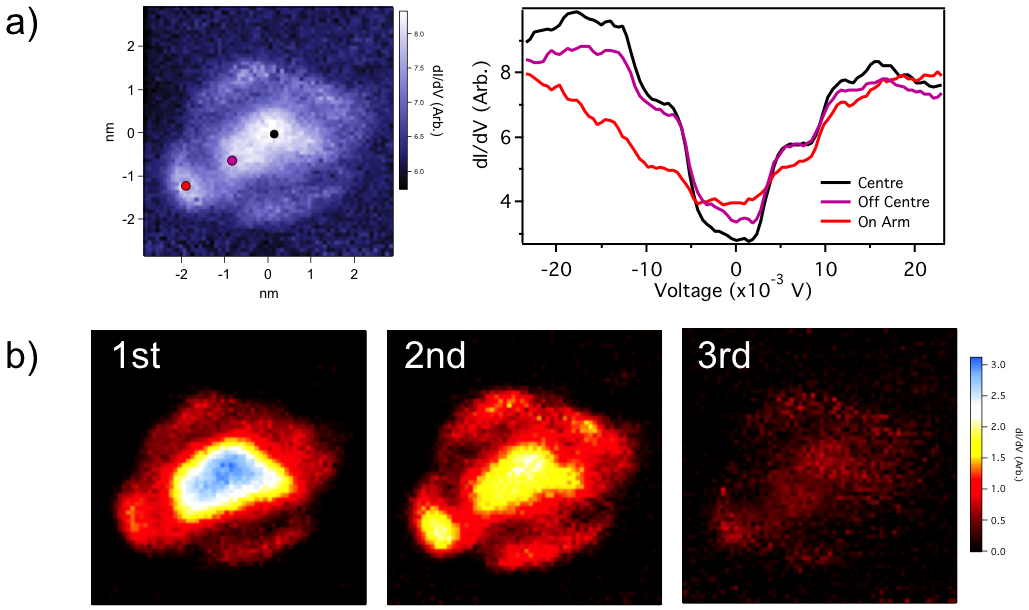

Figure 7.17: Spatial dependence of IETS steps. a) Spectra taken over the centre, the ligand and halfway between shows that the intensity varies, but the energy of the steps remain constant. b) Intensity of the steps across the molecule, the same spatial dependence is observed for each step. (V_{set} = 23mV, I_{set} = 1nA)

One possible explanation for the third step is the presence of a second spin such as a delocalised electron on the ligands of the Pc molecule. The Fe spin interacts with the spin and this interaction results in extra steps. Evidence of a ligand spin has been observed in the Kondo feature observed on CuPc on Ag(100) [157].

If the spin of the molecule on Cu_2N is not S=1 but S=2, we would expect three steps; S=3/2 can be ruled out as we would only see one transition at zero field field. As the addition of an electron would only create a half integer increase in spin, the most likely way for S=2 to occur is a reduction in the crystal field term. This effect has been observed for metal-porphyrins with axial ligands attached [158].

DFT calculations for FePc on Cu_2N (see appendix for details), do not support either of these explanations. For both Cu and N sites, and for the different binding angles the FePc is calculated to have S=1 and no ligand spin is observed. Calculations do suggest that there is another ground state with different spin that is very close energy. Therefore the excitation may change the total spin state by exciting into a higher manifold.

7.5 Conclusion

Here we have shown that the properties of FePc on Cu_2N are defined by the binding site of molecule. The change in properties between the Cu and N sites, is observed in both imaging and in spectroscopy data. Molecules bound on a Cu site show signs of both electronic and magnetic coupling to the surface. For FePc on a nitrogen site, we observe spin excitations suggesting the Fe is decoupled from the surface. That the atomic binding site plays a key role in defining the properties has large scale implications in the creation of devices on the atomic scale, as it shows the level of control that will prove necessary.

7.6 Future work

Through the use of DFT, we may be able to show the reason for the difference in high bias spectroscopy between FePc molecules on Cu and N sites.

In Fig 7.18, XAS and XMCD results are shown for submonolayer coverages of FePc on Cu_2N monolayers and Cu(001) taken at 6K. These measurements were taken in collaboration with Matteo Mannini from the group of Roberta Sessoli, on the ID08 beamline of the European Synchrotron Radiation Facility (ESRF) in Grenoble. We show XAS spectra at the iron $L_{2,3}$ edge, for 0° (sample normal to x-ray beam) and XMCD at both 0° and 45°. A difference in the spectra is observed between FePc molecules on Cu and Cu_2N, therefore with further analysis we may be able to explain the third step.

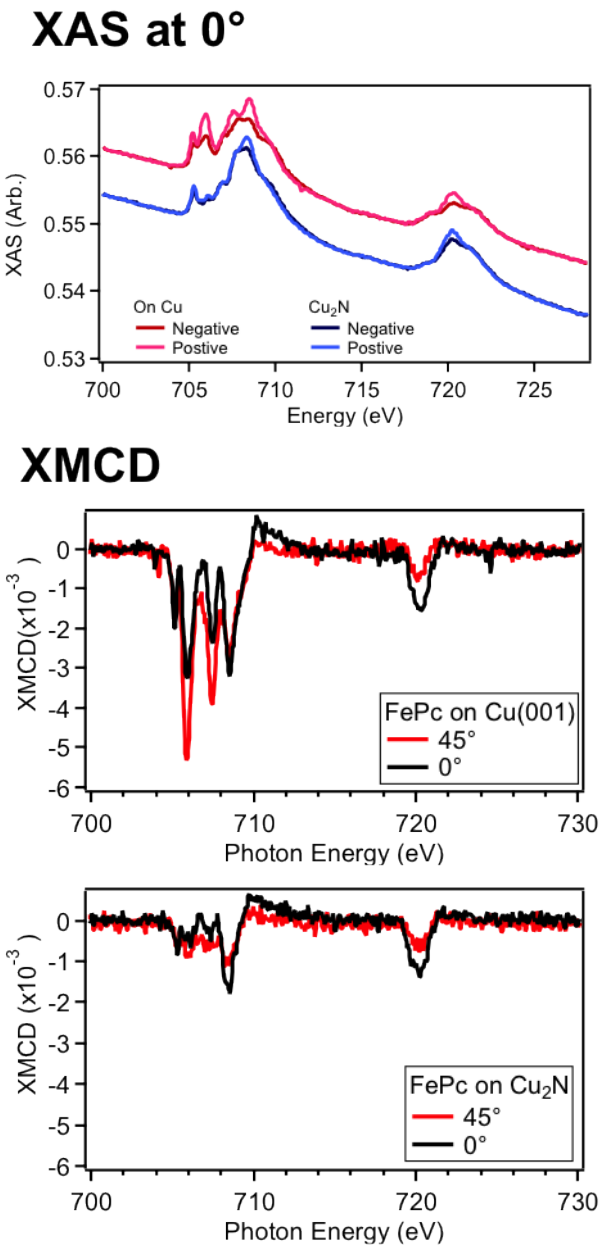

Figure 7.18: XAS and XMCD spectra taken for FePc on Cu(001) and FePc on Cu_2N. A clear difference is seen in the XMCD between FePc on Cu and Cu_2N and suggesting that a change in the Fe d shell is induced by the Cu_2N when compared with the Cu(001).

Chapter 8

Magnetically sensitive negative differential resistance

8.1 Abstract

Phenomena that exhibit a large sensitivity to magnetic fields, such as giant magnetoresistance (GMR), gained widespread prominence through their use in sensors and novel non-volatile memories [1]. There is considerable interest in scaling such spin sensitive phenomena down to the single molecule level [120, 159], particularly because this may enable novel single-molecule spintronic devices [4].

In this chapter we report magnetoresistance in an asymmetrically coupled single molecule junction arising from negative differential resistance (NDR) that shifts in a magnetic field at a rate that is two orders of magnitude larger than expected for simple electronic Zeeman shifts. This produces two voltage-tunable forms of magnetoresistance, which can be selected via the applied bias voltage. The NDR is caused by transient charging [109, 160, 161] of an iron phthalocyanine (FePc) molecule on a single layer of copper nitride (Cu_2N) on a Cu(001) surface at voltages corresponding to the alignment of sharp resonances in the filled (ionization) and empty (affinity) molecular states with the Fermi energy in the Cu(001). An asymmetric voltage divider effect in the junction, much larger than observed in other atomic-scale double-barrier systems [109, 161] because of the Cu_2N layer, enhances the apparent voltage shift of the NDR with magnetic field, which inherently is on the scale of the Zeeman

energy [162]. These results illustrate the impact that asymmetric coupling to nearby metallic electrodes can have on transport through individual molecules and highlight how this can be used to develop new molecular spintronic applications.

8.2 Introduction

Research into magnetoresistance has been driven by the widespread use of giant magnetoresistance (GMR) sensors in hard drives as well as other applications such as magnetoresistive random access memory (MRAM) [1]. GMR sensors are constructed from two ferromagnetic layers separated by a thin non-magnetic layer; in these junctions, large resistance changes occur in the presence of a magnetic field B [2]. This change in resistance can be further increased by replacing the non-magnetic layer with an insulating layer: in this case the effect is called tunnelling magneotresistance (TMR) [163]. To reach even higher storage densities, research has begun to concentrate on magnetoresistance at the atomic scale in both the TMR and GMR regimes [120, 159, 164]. At the scale of a single molecule, however, the small area for enclosing flux and modest energy scales associated with electronic Zeeman shifts typically are thought to make it difficult to tune magnetoresistive phenomena with an external magnetic field.

Another electron transport phenomenon with technological relevance that occurs at the atomic scale is NDR [160, 161, 165–172], in which an increase in voltage causes a decrease in current. Commercial devices, such as the resonant tunnelling diode, utilise these regions in specialised applications where very high speed oscillation [173] or switching [174] is required. A number of different mechanisms have been shown to give rise to NDR at the atomic scale [160, 161, 165–172], though none is expected to have a magnetic field dependence that would cause a shift of the NDR at a scale larger than the Zeeman energy.

8.3 Magnetically sensitive NDR

We observe an NDR effect for FePc molecules placed in a vacuum junction on top of a Cu(001) surface capped with a single layer of Cu_2N. Remarkably, as seen in Fig

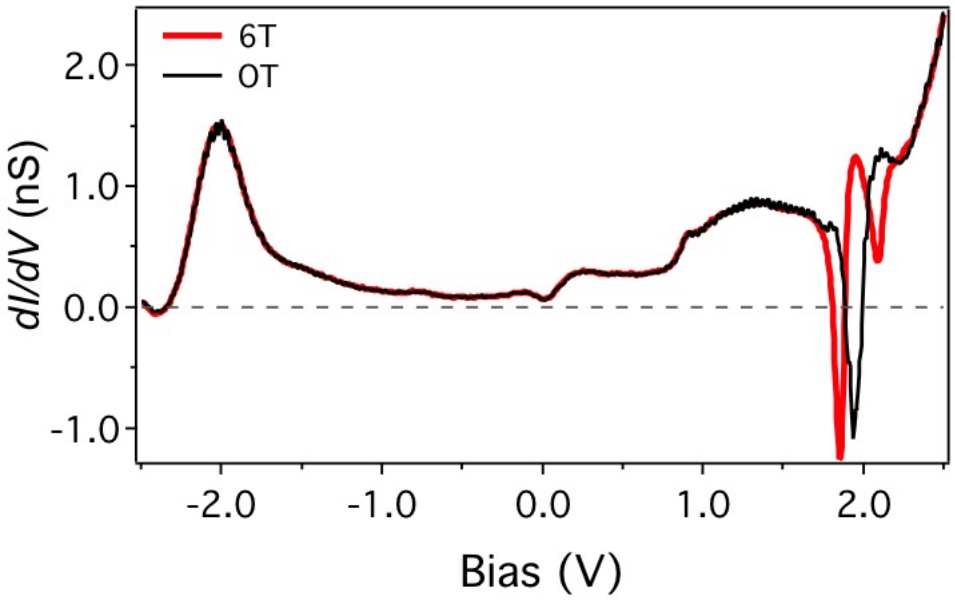

Figure 8.1: Magnetically sensitive NDR observed on FePc on $Cu_2N/Cu(001)$. dI/dV spectroscopy measurements taken above the centre of a FePc molecule (V_{set}=-2.5V, I_{set}=0.8nA). A clear NDR feature is observed, which can shift by up to -15 mV/T, as seen in spectra taken at 0 T (light red) and 6 T (dark red). The magnetic field only moves features in the NDR region: other features in the spectrum remain constant.

8.1, when a magnetic field is applied the NDR minimum can shift by a large amount, in this case almost 0.1 V for an applied field of 6 T: this is two orders of magnitude larger than the electronic Zeeman effect. To our knowledge such magnetic sensitivity has previously not been observed for other systems exhibiting NDR.

The NDR effect is observed in 12.5% of the molecules (23 out of 184), at both positive and negative bias, and at a variety of voltages; examples are shown in Fig 8.2. NDR is observed on molecules bound at various angles and on both Cu and N sites.

NDR is always and most strongly observed at the centre of these molecules (Fig 8.3). In rare instances, it has been observed on the ligand when the molecule is close to defects, suggesting local defects play a small role. For consistency, measurements reported here are taken above the centre of the molecule. We do not observe a difference in topography between molecules that show NDR and those that do not.

A more detailed perpendicular field dependence for the NDR spectra in Fig 8.1 is

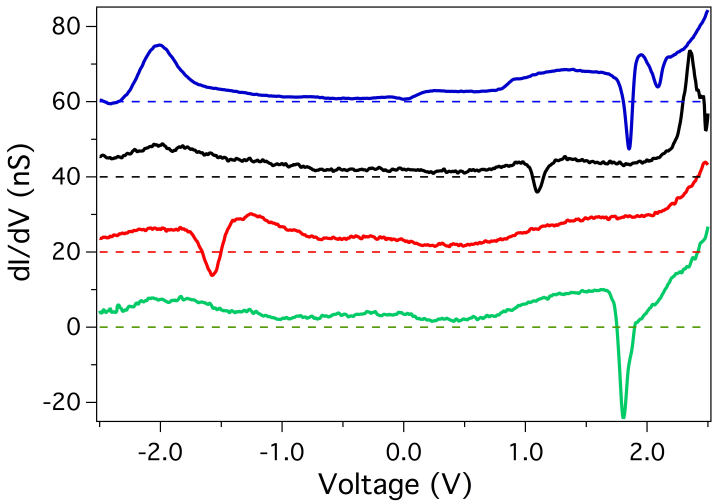

Figure 8.2: Differential conductance spectra (V_{set} = -2.5 V, I_{set} = 1 nA) exhibiting NDR taken on four different molecules. NDR is observed at both polarities and over a range of voltages. Traces have been offset for clarity; dI/dV = 0 is indicated by a dashed line for each trace.

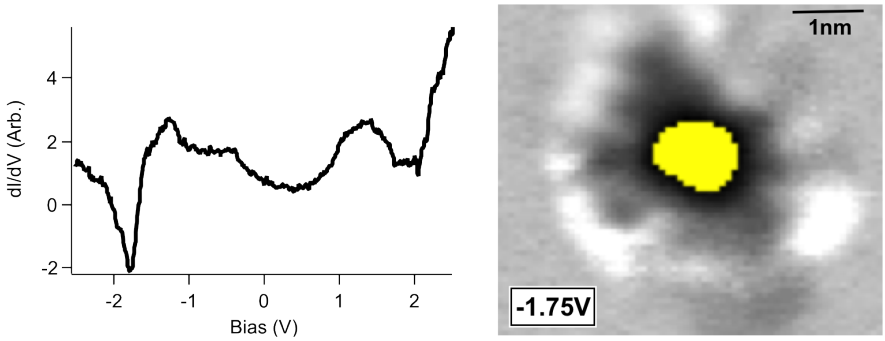

Figure 8.3: Spatial dependence of NDR showing the NDR is observed only on the centre of the molecule. The dI/dV spectra is shown and the dI/dV energy cut at the voltage of the NDR min (V_{set}=-1.75V, I_{set}=1nA), negative conductance is shown in yellow.

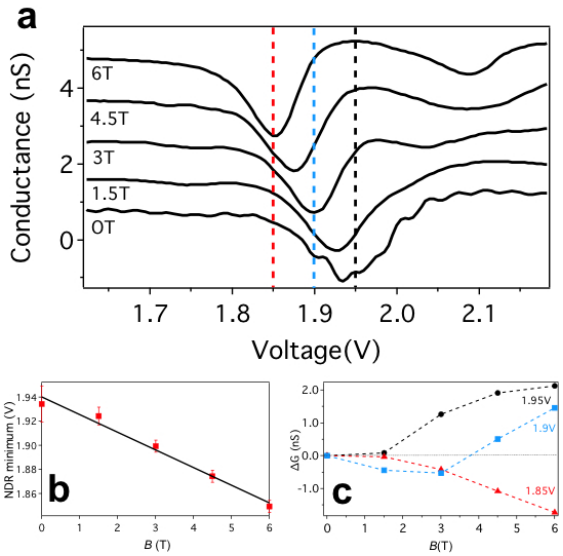

Figure 8.4: Differential conductance changes caused by magnetic field sensitive NDR. a) Differential conductance spectra (V_{set}=-2.5V, I_{set}=0.8 nA) acquired above the centre of an FePc molecule displaying NDR at B=0T, 1.5 T, 3.0 T, 4.5 T, and 6.0 T (as labelled). The NDR region moves to more negative voltages with increasing B. Spectra are offset for clarity. Vertical dashed lines indicate 1.85 V (red), 1.90 V (blue), and 1.95 V (black). b) NDR minimum vs. B, with the solid line showing a gradient of -15mV/T. c) ΔG versus B at 1.95 V (black), 1.9 V (blue), and 1.85 V (red).

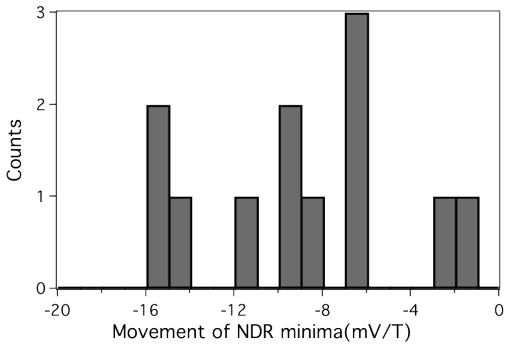

Figure 8.5: Histogram of the sensitivity of the NDR minima to field, field sensitivity is observed from -2mV/T up to -15mV/T.

shown in Fig 8.4a. As seen in Fig 8.4b, we find that the voltage of the NDR minimum shifts approximately linearly with a slope of -15 mV/T. The field sensitivity varies from molecule to molecule, ranging from -2 mV/T up to -15 mV/T as shown in the histogram in Fig 8.5. The shift is always to more negative voltages with higher field regardless of the voltage at which the NDR occurs. Furthermore, our measurements suggest that the shift of the NDR may depend only on the magnitude of the field component perpendicular to the plane, with an in-plane field of 1 T and a reversal of the sign of the magnetic field having no impact. Additionally, on rare occasions we have observed sharp peaks in the conductance spectra in similar voltage ranges that exhibit a similar dependance on B (see Fig 8.6).

To further characterise this novel field-sensitive NDR, we also examine its behaviour with temperature. As seen in Fig 8.7a, the NDR minimum becomes dramatically more shallow and more broad with increasing temperature. The full width at half maximum (FWHM) is shown in Fig 8.7b and is found to increase linearly but at a rate of approximately $225 \pm 11 k_B/e$, where e is the magnitude of the electron charge; this rate is nearly two orders of magnitude larger than the expected 3.5 k_B/e for broadening caused by thermal smearing from the Fermi seas in the tip and the sample. Furthermore, as seen in Fig 8.7c, we find that the depth of the NDR minimum decreases with a $\frac{1}{T}$ dependence, which is the expected dependence of a feature which is broadened by the Fermi distribution, as seen in Chap 3.

Figure 8.8 shows dI/dV spectra taken at different set point currents. As the set point in STM measurements defines the height of a tip, by increasing the setpoint current we move the tip closer to the surface. As shown in Fig 8.8a as the set point

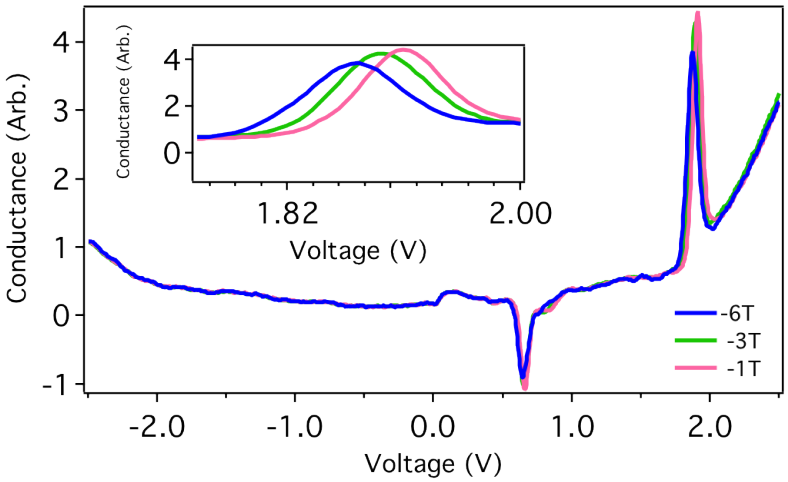

Figure 8.6: Differential conductance spectra (V_{set} = -2.5 V, I_{set} = 1 nA) of a molecule exhibiting both NDR and a sharp peak. Spectra were taken at -6 T, -3 T and -1 T on the centre of the molecule. The inset is a zoom in on the sharp peak, which moves to more negative voltages with increased field.

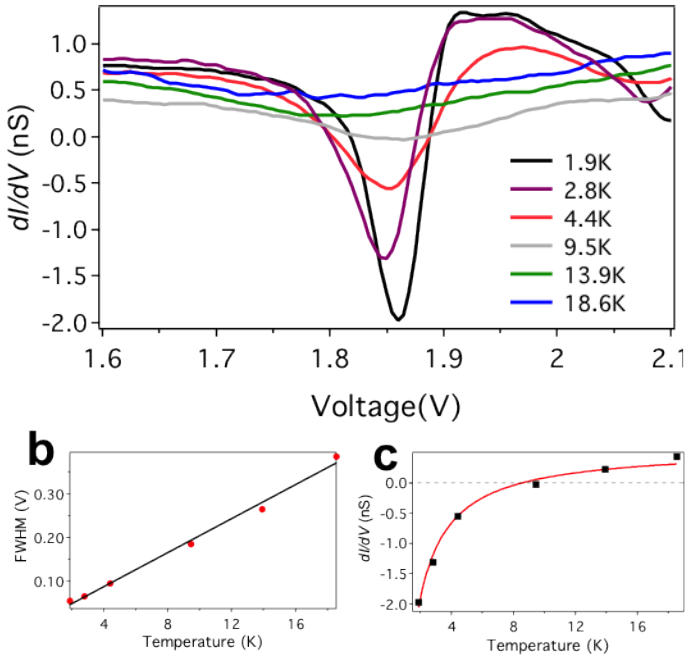

Figure 8.7: Temperature dependence of NDR. a) Zoom-in of the NDR minimum in differential conductance (V_{set}=-2.5V, I_{set}=0.8 nA) at different temperatures; the minimum remains positive above approximately 10 K. b) FWHM of the NDR minimum (with the baseline taken as the value at 1.6 V) vs. temperature. Black line highlights the linear trend, with FWHM $225k_BT/e$. c) Differential conductance at the NDR minimum vs. temperature. Solid red line is a guide to the eye for $\frac{1}{T}$.

is increases the NDR minima moves towards the Fermi energy. In Fig 8.8b, the energy of the NDR minimum is plotted against the change in tip height; a linear dependence is observed.

Of the currently known NDR mechanisms at the atomic scale [160,165–167,169,171], none have a magnetic field dependence that would cause a shift at a scale larger than the Zeeman energy. DFT calculations indicate that the FePc retains its free spin of $S = 1$ on Cu_2N. In Chap 7 we show spin excitation spectroscopy [8, 69] on the molecules that do not exhibit a Fano-like feature at zero bias and find that the shift in the excitation energy is less than 1meV for $B = 6$T, ruling out the possibility of an anomalously large g-factor.

The magnetic flux through the Pc ring is small compared to a quantum of magnetic flux, suggesting that the field dependence is not the result of a Abramov-Bohm type effect. The field could deform the shape of the molecule and therefore modify the coupling to the surface to create the field dependence. While only a small distortion of the molecule may be enough to significantly change its coupling to the surface, we are unable to resolve any change in the size of the molecule with field (down to approximately 10 pm).

Interference effects between two tunneling pathways from the tip to the surface, one directly through the central Fe atom and another also passing through the Pc ring, could also lead to a anti-resonance; however, this mechanism would not produce a negative conductance.

Therefore to explain this novel manifestation of magnetically sensitive NDR, we suggest a mechanism based on transient charging that arises from the occupation of molecular resonances [175]. The transient charging of the molecule results in a change in the tunneling rates through the molecule; this can either increase or decrease the differential conductance, with the latter resulting in NDR. Sharp states corresponding to a two-step resonant tunnelling process between the tip, the molecule, and the substrate have been observed in studies of individual molecules on thin insulators [109]. In the resonant tunneling process, voltage is dropped in each of the two barriers (vacuum and Cu_2N) in the tunnel junction, with most of the drop expected to occur in the vacuum between the tip and the molecule; see Fig 8.9 for a schematic. The small fraction of the applied bias voltage that is dropped across the thin insulator therefore shifts the molecular orbitals with respect to the

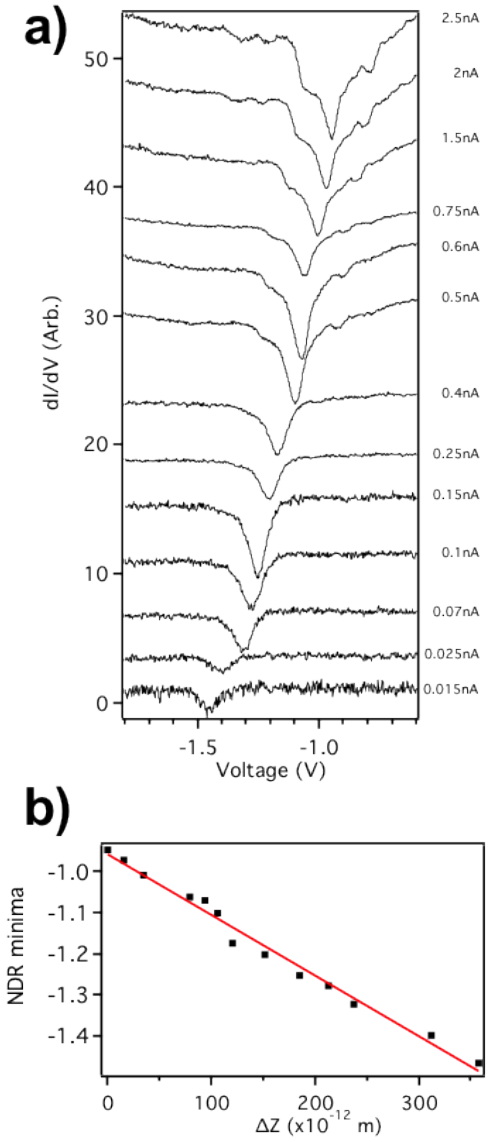

Figure 8.8: Impedance dependance of NDR. a) Zoom-in of the NDR minimum in differential conductance (V_{set}=-1.8V) at different current set points; as the set point is increased (i.e tip moved closer to the sample) the minimum moves towards the Fermi energy. The set point of each measurement is shown, and the spectra have been offset for clarity. b) Voltage of NDR minima plotted against height; a straight line has been fitted to the data. The tip height is measured by carrying out I(z) spectroscopy.

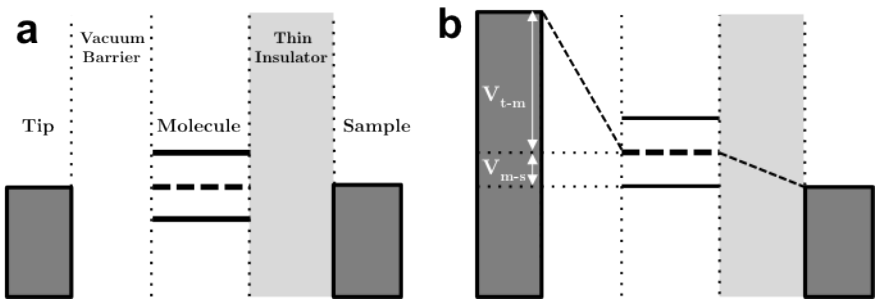

Figure 8.9: Schematic of a double barrier junction. a) Junction at $V = 0$, with the Fermi levels of the tip and sample aligned. Solid horizontal lines indicate the filled and empty states of the molecule; light dashed line is a reference between these levels. b) Junction at $V = V_{res}$, when the voltage, V_{m-s}, dropped across the thin insulator (i.e. between the molecule and the underlying Cu surface) aligns the molecular orbital with the Fermi level of the sample. The remaining voltage, V_{t-m}, is dropped across the vacuum barrier (i.e. between the tip and the molecule), allowing the molecular levels to shift with respect to the sample Fermi level.

sample Fermi energy. DFT calculations in which an electric field has been added to the system also show that a finite potential drop exists between the molecule and the substrate.

We note that these resonances would be expected to shift towards lower magnitudes of voltage as the STM tip is moved closer to the molecule, making the double-barrier junction more symmetric [109, 161]; the NDR features we observe manifest this same behaviour, for NDR features at both positive and negative bias. Also, the broader continuum of states, which arises from simple elastic tunneling through the molecule, is unaffected by this double barrier behaviour in the junction. The sharp peaks which are observed also exhibit a similar dependence on z (see Fig 8.10).

In these asymmetric, double-barrier tunnel junctions, the strongest resonance occurs when one of the molecular orbitals aligns with the Fermi energy in the sample (Fig 8.9b); this is because the molecule is more strongly coupled to the sample than to the tip [175]. Depending on whether the alignment occurs with an empty or filled orbital, the molecule can be transiently negatively or positively charged respectively during the transport process; since this occurs at negative and positive bias respectively [109] and can result in either increased and decreased differential conductance [161], it is natural to expect the NDR to occur in either polarity of bias voltage for different molecules. Note that this charging is a consequence of the

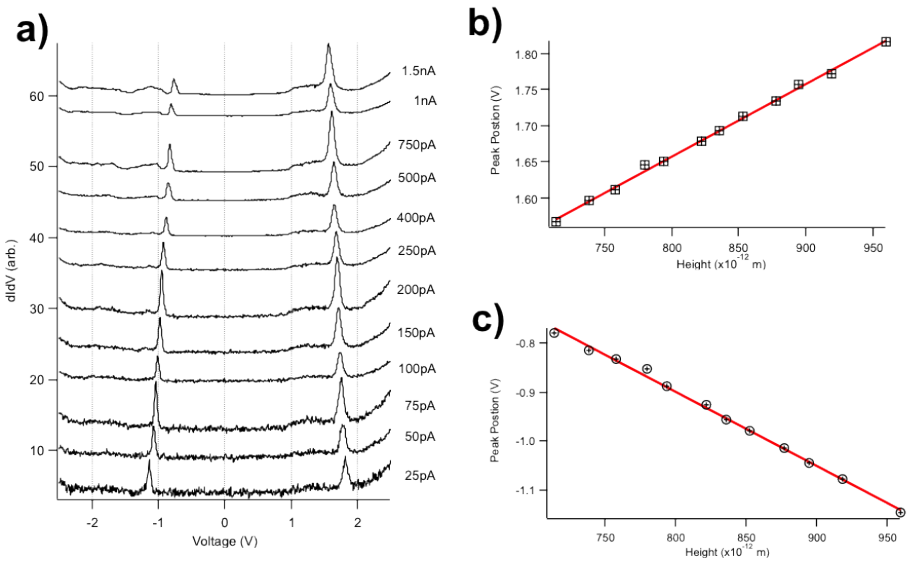

Figure 8.10: Impedance dependance of sharp peaks. a) Differential conductance (V_{set}=2.5V) at different current set points; as the set point is increased (i.e tip moved closer to the sample) the peaks at both positive and negative bias move towards the Fermi energy. b) Positive peak and c) negative peak value plotted against height; a straight line has been fitted to the data.

extended lifetime of the tunnelling electron on the molecule: if the tip were moved away then the molecule would quickly return to its neutral state.

Because the molecular levels shift with respect to the Fermi energy by much less than the applied bias voltage, the apparent voltage scale of the resonance is enhanced [109, 161]. This can be quantified by considering the unexpectedly large linear dependence of the NDR's FWHM with temperature. For the molecule whose spectra are shown in Fig 8.7, this enhancement is the ratio of the prefactors: $225/3.5 \sim 65$. This enhancement value is equal to the fraction of the voltage that is dropped across the Cu_2N: $\alpha = d^*/(d^* + z)$, where $d = d^*\epsilon$, d is the distance between the molecule and the underlying metal, ϵ is the effective dielectric constant of the Cu_2N monolayer, and z is the distance between the molecule and the tip.

Although there are no existing direct measurements of the effective dielectric constant ϵ for Cu_2N, we can estimate the value ϵ for the Cu_2N monolayer using a simple parallel-plate capacitor model with the distance between the molecule and the underlying metal d as well as the z, the distance between the molecule and the tip. The value of d can be estimated from the DFT calculations as the distance from the

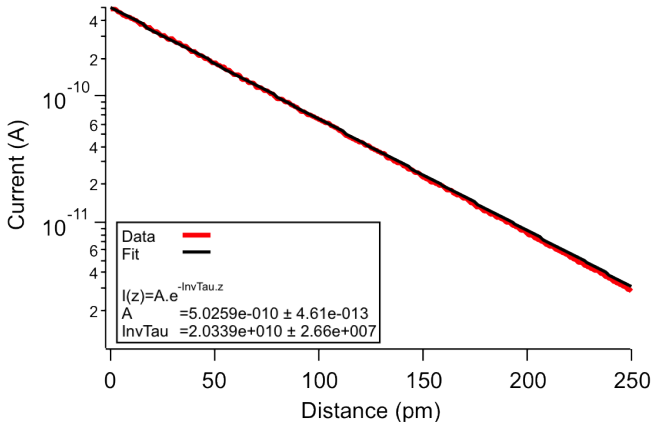

Figure 8.11: I(z) measurement. We observe an order of magnitude change in current for every 0.114nm change in z. (V_{set}=0.5V, I_{set}=0.5nA)

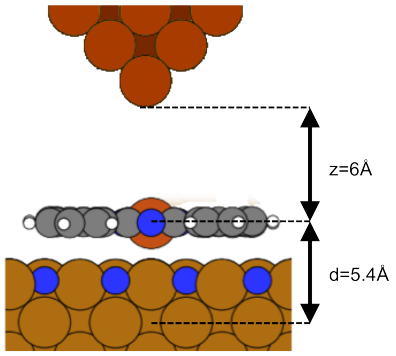

Figure 8.12: Height estimates for estimation of dielectric constant FePc on Cu_2N. Estimate of tip height is from comparison of I(z) measurement with a quanta of conductance. Estimation of thickness of Cu_2N is from DFT calculations, details of which are included in the appendix

Fe atom to the Cu(001) layer, which is roughly 0.54 ± 0.05 nm.

An estimate for the tip-molecule distance can be made from the setpoint conductance of the junction for the spectroscopic measurements shown in Fig 8.7 by assuming that contact $z = 0$ corresponds to an impedance of the order of 10 kΩ (i.e. the quantum of conductance) and that this increases by approximately one order of magnitude for every 1.14 Å change in z, which is the observed current decay over an FePc molecule, as shown in Fig 8.11. This gives a value of $z \sim 0.6 \pm 0.10$ nm

With the estimates $d \sim 0.54 \pm 0.05$nm and $z \sim 0.6 \pm 0.10$nm, we obtain a value for $\epsilon \sim 60 \pm 20\%$, which is approximately an order of magnitude greater than for

other thin insulators. Therefore, using the simple model shown here, both the high effective dielectric constant and the thinness of the Cu_2N play a role in creating an enhancement value that is much higher than that observed on other thin insulators [109].

The large enhancement factor provides a possible explanation for the low number of molecules for which NDR is observed. Cu_2N is no longer a thin insulator above 2.5V, as the junction is no longer a double barrier. Therefore only levels above -40mV ($\frac{2.5}{65}$) of the Fermi level can be observed. At negative voltage, we find that above -3.0V, the molecules are sometimes picked up by the tip. This therefore restricts us to levels below 50mV. The result of these two limits is that these measurements are only sensitive to levels within approximately 40mV of the Fermi energy. As shown in Chap 7 and in DFT calculations, the energy levels for each molecule are slightly different and therefore we believe their low number of NDR observations is a result of the narrow spectroscopic window, rather than a physical difference between molecules where it is observed and those where it is not.

In the double barrier model, two resonances can occur. One resonance occurs when the energy of the molecular state is equal to the voltage dropped between the tip and the molecule.

$$V_b = E_s - \alpha V_b \tag{8.1}$$

Here 'α' is the fraction dropped across the vacuum, depends on the ratio of the vacuum gap to thin insulator.

The second resonance occurs when the energy of the molecular state (E_s) is equal to the voltage dropped across the thin insulator.

$$E_s - \alpha V_b = 0 \tag{8.2}$$

It is this resonance that creates the NDR effect, and NDR is observed when

$$V_b = -E_s(1 + \frac{z}{d^*}) \tag{8.3}$$

However, the energy of the the state of the molecule also depends on the magnetic field, $E(B)$,

$$V_b = -[E_0 + E(B)][1 + \frac{z}{d^*}] \tag{8.4}$$

where E_0 is the energy of the molecular state at zero field.

From Eqn 8.4, it is clear that the voltage at which the NDR occurs can be manipulated by modifying both the amplification factor (by changing the height of the tip as shown in Fig. 8.8), and the field (as shown in 8.4).

Owing to the enhancement factor, the levels responsible for the NDR minimum shift with magnetic field at a much smaller intrinsic rate than the observed movement of the mimima; for the spectra shown in Fig 8.4, this would correspond to an intrinsic shift of 231μeV/T, which is of the order of the Zeeman energy. Zeeman splitting of such sharp molecular resonances into doublets has been observed in the presence of a magnetic field [162]. This shows that an asymmetric junction can not only significantly influence the electronic properties of the junction [157] but also allow for the enhancement of energy scales, causing small shifts in energy to be magnified to large-scale changes.

In order to explain the magnetic dependence observed, it is necessary to consider the d levels in FePc. In Fig 8.13, a cartoon of the energy levels of FePc is shown; the cartoon is based on the square planar crystal field in which occurs in FePc. The $d_{x^2-y^2}$ orbital is heavily disfavoured due to the N atoms and remains unfilled. As Fe^{2+} has six electrons, four are placed in the 4 remaining spin up levels, and two are placed in the spin down. As the two spin down levels will be higher in energy due to the coulomb repulsion term, the highest filled state levels will be spin down. The closest two empty states to the Fermi level will be the remaining non-disfavoured d-level spin down states. This therefore suggests that the states close to the Fermi level will all have the same spin.

A caveat to this discussion is that it is built upon a simple crystal field argument. However as the exact crystal field splitting is not know, we have assigned it to match the NDR effect. In DFT calculations the situation is shown to be more complicated. The orbitals of FePc are mixed, and the $d_{x^2-y^2}$ orbital can be close to the Fermi energy depending for some binding geometries due to the change in the crystal field

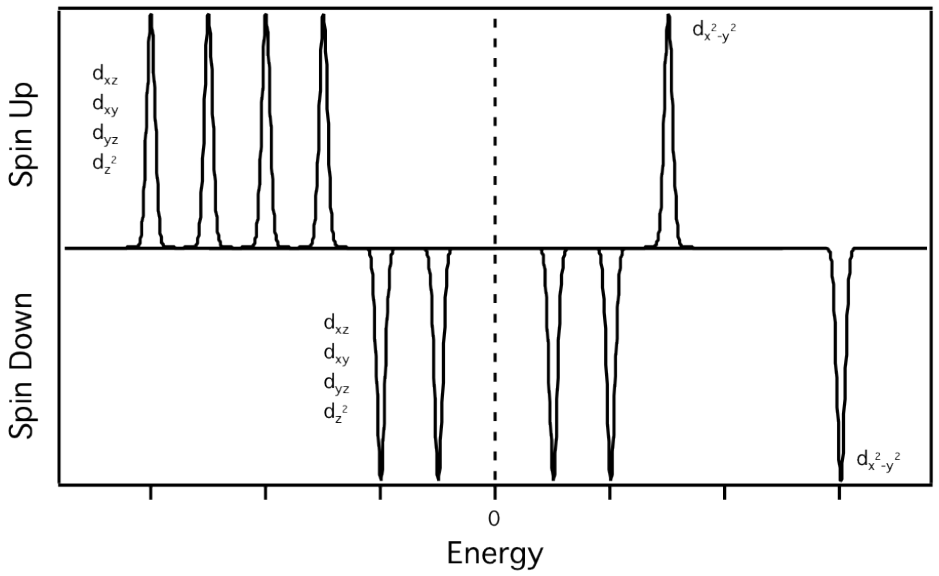

Figure 8.13: Cartoon based on a square planar crystal field. As the $d_{x^2-y^2}$ orbital is disfavoured it remains unfilled. 6 electrons are placed in the four remaining levels, resulting in spin down states being closest to the fermi energy both at filled and empty states.

term.

Using the simple model where the spin states close to the Fermi energy have the same spin explains the behaviour of the NDR minima with field. When we increase the field, we observe a movement, not a splitting, as the levels are already spilt by the Coulomb repulsion term. The NDR minima moves to negative bias with increasing field when the resonance is created by filled states and empty states. This is expected as the levels close to the Fermi energy in both filled and empty states have the same spin and therefore move with field in the same direction. The levels of FePc thus are act as a spin filter in the junction [176].

8.4 Cross-over Magnetoresistance

The ability to manipulate NDR with a magnetic field not only enables tuning of the voltage of the NDR minimum [177] but also results in the creation of a junction that exhibits two novel magnetoresistance effects. Figure 8.14 shows a phenomenological model of the NDR where the differential conductance line shape

$G(V, B)$ is represented by a Lorentzian dip that shifts linearly with $|B|$ on top of a constant differential conductance background. For voltages that are more positive than the voltage of the NDR minimum, the change in differential conductance $\Delta G(V, B) = G(V, B) - G(V, 0)$ is always positive and increases with $|B|$ until it saturates. Remarkably, however, the magnetoresistance ratio $\frac{\Delta G(V,B)}{G(V,0)}$ can become arbitrarily large as V approaches the value at which $G(V, 0) = 0$. Furthermore, its sign is positive or negative depending on the sign of $G(V, 0)$; we therefore label these the MR+ and MR- regions respectively. In practice, of course, the arbitrarily large magnetoresistance that occurs near the boundary of these two regions would be limited by experimental constraints. The second magnetoresistance effect, which we refer to as "cross-over magnetoresistance" (XMR), is manifested at voltages that are more negative than the NDR minimum. In this regime, as seen in Fig 8.14, $\Delta G(V, B)$ initially becomes increasingly negative with $|B|$ until it reaches a minimum value; after this, it becomes more positive, crosses zero, and then saturates at a limiting value. The magnetic field at which the polarity of the differential conductance "crosses over" varies with voltage, creating a magnetic-field sensitive switch that is tunable with voltage. As seen in Fig 8.4c, both of these effects are observed for FePc on Cu_2N.

8.5 Conclusion

We observe magnetically sensitive NDR in a single-molecule junction arising from resonant tunnelling producing charging in the molecule. The effective shift of the NDR with magnetic field is enhanced by the inherent voltage division across the two asymmetric tunnelling barriers; this allows for the creation of novel magnetoresistance phenomena. Similar enhancement of the effective energy scale for other multi-step tunnelling phenomena, both magnetic and non-magnetic in origin, should be possible. Furthermore, the size of the enhancement can be controlled by tuning the asymmetry of the tunnelling barriers, which can be modified by making physical or chemical changes to the junction by using different thin insulators or molecules [8, 18, 40, 75, 161] . This highlights the prominent role that the junction itself can play in defining the properties of the smallest possible electronic and spintronic device architectures.

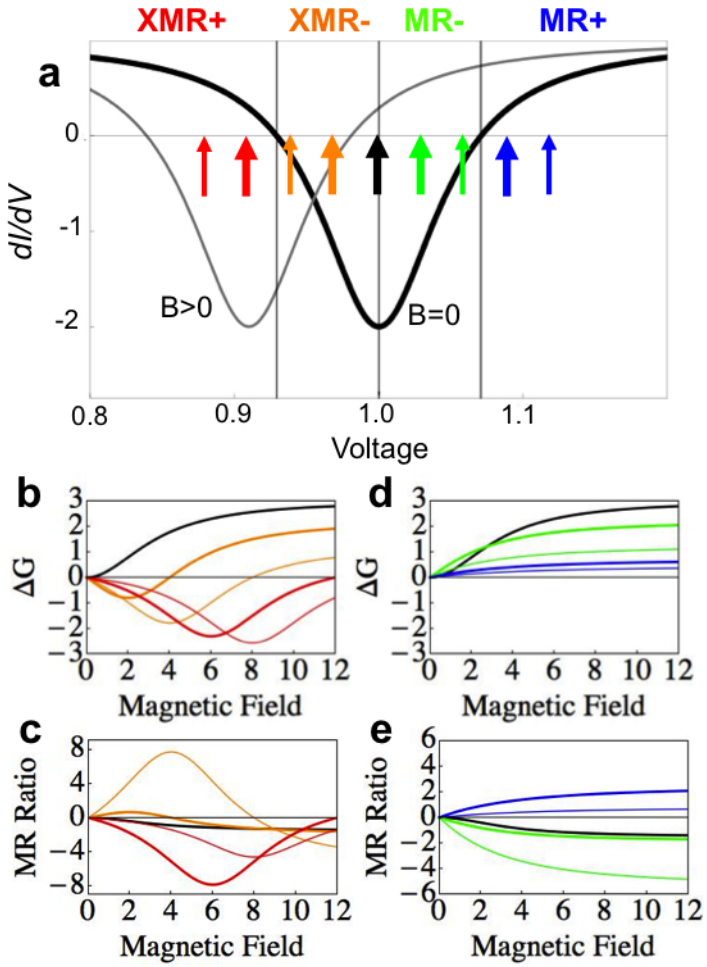

Figure 8.14: Model of magnetically sensitive NDR. a) Differential conductance versus voltage for constant differential conductance background with an NDR feature that shifts linearly with $|B|$; two values of B, $B = 0$ (thick black curve) and $|B| > 0$ (thin grey curve), are shown. Arrows mark voltages shown in panels below. All units have arbitrary dimensions. b) ΔG vs. B in XMR+ and XMR- regime. c) Corresponding magnetoresistance ratio from panel b. d) ΔG vs. B in MR+ and MR- regime. e) Corresponding magnetoresistance ratio from panel d.

Chapter 9

Charge transport through a 4f magnetic moment in a SMM

9.1 Abstract

In order to capitalise on the current advances in controlling a single spin, it will be necessary to contact the spin while regulating the atomic environment. Placing magnetic atoms in a molecule provides a way to reproducibly control this environment. Therefore it is of great interest to investigate how electrical transport through a molecule interacts with the spin it contains and how this can be controlled. There may be advantages in utilising magnetism produced by f-shell states [16, 81], especially in molecules [4]. Recently, it has been shown that charge transport through a molecule can access f-shell states despite their localisation [142].

Here we show that for charge transport through a bis(phthalocyaninato)Dy(III) complex ($DyPc_2$) that is strongly coupled to a metal surface it is possible to directly access the 4f magnetic moment. Spatially resolved scanning tunnelling spectroscopy shows a variation in the amplitude of a Fano line shape near the Fermi energy, indicative of a Kondo effect due to screening of a localised magnetic moment coupled to a metallic continuum. The localised moment is shown to occur due to the 4f states rather than the delocalised spin of an electron on the ligand, which has been observed in previous work where $TbPc_2$ is coupled more weakly to the surface. This work demonstrates that the coupling to the surface can be used to control which spins are

present on a molecule as well as whether they can be accessed in transport.

9.2 Introduction

Accessing spins via electric transport is a necessary prerequisite for the creation of many of the new paradigms on which it is hoped future-computing technology will be based, such as quantum computing and spintronics. Single molecule magnets (SMM) could have applications in both of these areas due to their high spin and long spin relaxation time [4,13,16]. It has been shown that these magnetic properties can survive placement onto the surface [89] and that the spin can be electrically contacted in the case of a d shell [4,18]. Recently SMM have been created with higher blocking temperatures and anisotropies by using f-shell magnetic moments [16].

$LnPc_2$ molecules have been shown to be SMMs with high blocking temperatures [17], and due to their thermal stability can easily be studied as single molecules in ultra high vacuum [16]. The free $LnPc_2$ molecule consists of two phthalocyanine (Pc) rings with a lanthanide metal atom in the centre, with two distinct spins: one arising from an unpaired electron shared between the two Pc ligands and another from the central lanthanide atom's 4f spin [20].

Atomic scale studies of $TbPc_2$ and YPc_2 on Au(111) have shown clear evidence of the ligand spin state that is strongly screened by the Kondo effect [53]. Measurements $NdPc_2$ on the more reactive Cu(001) surface show that despite the tightly confined nature of the f shell, it is possible to access the 4f states of the molecule in electronic transport [142]; for this case it is calculated that $NdPc_2$ does not have a ligand spin.

Gas phase $LnPc_2$ molecules are symmetric, but recent work has shown that chirality, where two forms cannot be superimposed, can occur to due to the binding angle breaking the symmetry of the system creating a possible method for controlling chirality [108, 140]. Chiral molecules include important molecules such as amino acids and sugar. The Nobel prize in Chemistry in 2001 was awarded for 'work on chirally catalysed hydrogenation reactions' [178]. Here the press release highlights the importance of chirality in biological processes stating 'the difference between the two forms can be a matter of life and death' [178].

In this chapter we explore the interplay between $DyPc_2$ and the underlying Cu(001) surface. The molecule is shown to be chiral due to the coupling to the surface. This asymmetry is utilised to show that 4f magnetic moment is interacting with the conduction electrons of the surface, creating a Kondo effect. This result demonstrates that the 4f magnetic moment in a SMM can be accessed in electric transport.

9.3 Asymmetric molecule substrate coupling

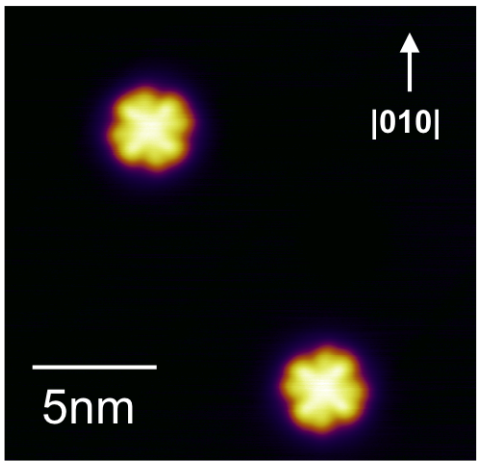

Figure 9.1: STM image of $DyPc_2$ on Cu(001) (V_{set}=0.1V, I_{set} = 0.1nA)

In Fig 9.1, an STM image of two $DyPc_2$ molecules is shown. Details of the sample preparation can be found in Chap 6. We observe that $DyPc_2$ binds at $\pm 27°$ to the |100|, as shown in Fig 9.2. If a 45° rotation is assumed between the top ring and the bottom ring, as has been observed in previous measurements [140], the bottom ring would bind at $\pm 18°$ to the |100| axis [179]. This agrees with previous results of Pc molecules on surfaces with a (001) crystal face [108, 144]. The small distribution of angles suggests that the lower ring is strongly coupled to the Cu surface.

In Fig 9.3, the full bias dependence of $DyPc_2$ is shown. At -1V, an eight lobe structure is resolved, which is characteristic of double decker molecules on surfaces [20]. As the voltage is reduced to less negative voltages, a fourfold symmetry becomes more distinct; this matches the previously published results for $NdPc_2$ on Cu(001) [142].

The $DyPc_2$ molecules show a distinct change in topography between +0.1V and

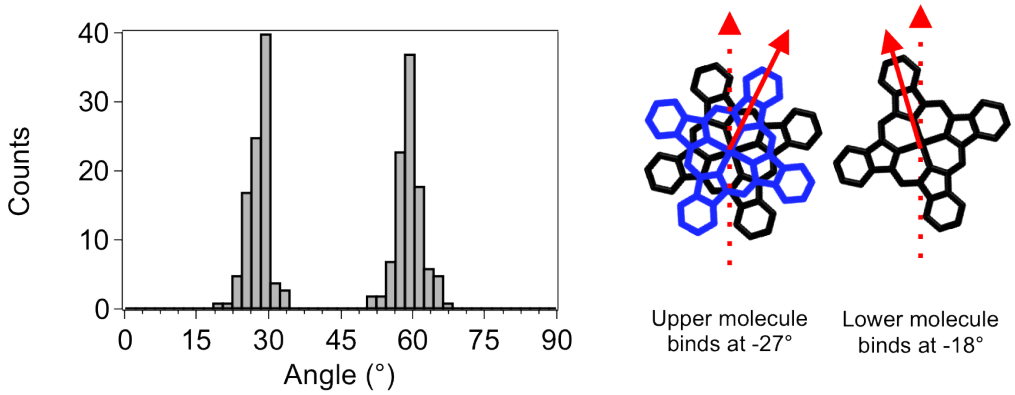

Figure 9.2: Binding angle of $DyPc_2$. Histogram of binding angle shows that $DyPc_2$ binds at $27 \pm 2°$ and $59 \pm 3°$ to the |100| axis [179]. As shown in the cartoon when the top molecule (blue) binds at $\pm 27°$ to the |001| axis, given a 45° rotation between the upper and lower ring, the lower molecule (black) binds to the surface at $\pm 18°$ to the |001| axis.

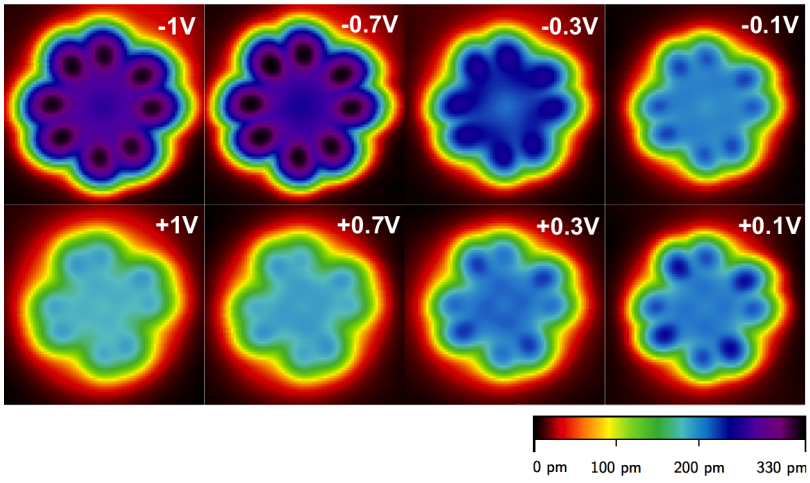

Figure 9.3: Bias dependent STM images of $DyPc_2$. At both -1.0V and -0.7V, the molecule show an eight lobe structure; a four fold symmetry becomes more evident as 0V is approached. Above 0V a clear asymmetry can be seen in the ligands which persists in positive bias (2.5 nm×2.5 nm, $I_{set} = 0.1$nA).

−0.1V. At -0.1V, the lobes of each arm are symmetric; at +0.1V, the lobes become asymmetric and this persists at higher positive biases. As the asymmetry occurs only at positive bias this suggests the effect is electronic and not a physical deformation of the molecule. Fig 9.4 shows two molecules of opposite binding angle; the asymmetry is observed to switch depending on the binding angle of the molecule.

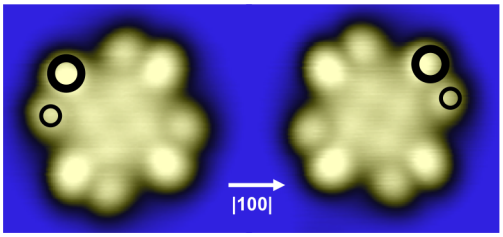

Figure 9.4: Images of $DyPc_2$ at opposite binding angle, where the asymmetry has been emphasised on one ligand. It is clear the asymmetry is mirrored between the two binding angles. ($V_{set} = 0.1V$, $I_{set} = 0.1nA$)

For previous work on CuPc on Ag(001), a similar effect is observed [108]. This was shown to be due to asymmetrical charge transfer between the surface and the molecule due to the binding angle [108, 140]. For $DyPc_2$ on Cu(001), the characteristics of the observed chirality match those of CuPc, suggesting that the asymmetry results from a similar effect. However, DyPc2 is asymmetric at positive bias, while CuPc is asymmetric at negative bias.

Therefore the symmetry of the system is broken by the binding angle of the lower ring to the surface. Due to this there is asymmetrical coupling between the lower molecule and surface and this asymmetry transfers into the top ring. This demonstrates that chirality created by the interaction with the surface can be transferred through the molecule.

Spectroscopy data, taken from -1.5V to +1.5V are seen in Fig 9.5; for spectra taken over the centre a peak at -0.7V is observed. Over the ligand we observe a peak at -0.6V. This an almost exact match to the data taken on $NdPc_2$ which is shown in Fig 9.6 a) [142]. Therefore it is reasonable to assume that the LDOS will be similar for both molecules, despite the different rare earth metal. In this framework, the lower Pc ring is strongly coupled to the surface resulting in hybridisation and charge transfer between the surface and the molecule. This causes the disappearance of the spin on the ligand. The peak on the centre at -0.6V is created due to states of mainly 4f character. From the $NdPc_2$ calculations shown in Fig 9.6 b) [142], the peak at

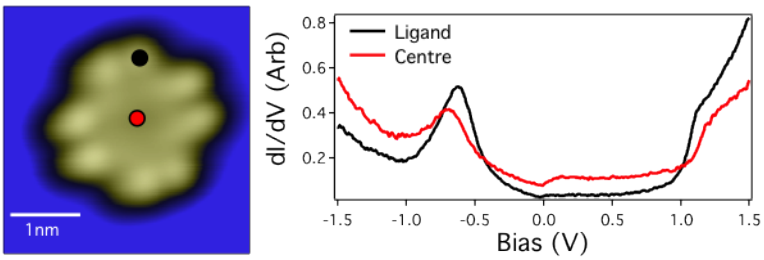

Figure 9.5: High voltage spectroscopy over the ligand and the centre of a $DyPc_2$ molecule. The results look very similar to those taken on $NdPc_2$ which are shown in Fig 9.6. (V_{set}=-1.5V I_{set} =0.1nA)

-0.6V for spectra taken over a ligand is created from the ligand states shifting due to the electric field produced between the tip and sample until the states become pinned due to hybridisation with the 4f states.

9.4 Accessing the 4f magnetic moment of $DyPc_2$

dI/dV spectra taken over both the ligand and the centre of the $DyPc_2$ are shown in Fig. 9.7. A Fano line shape is observed at the Fermi energy and additionally a peak around 40mV. As described in Chap 3, a Fano line shape is created when two coherent paths interfere with each other, where one path is into a sharp resonance and the second into a broad continuum [42]. It is often observed for STM studies of magnetic impurities on a metal surface where the Kondo effect produces the resonance [26, 48, 180]. A Kondo effect is observed on both $TbPc_2$ and YPc_2 on Au(111) where it is created due to the spin of the delocalised electron on the top ring [53].

The close match in high voltage spectroscopy and imaging between $DyPc_2$ and $NdPc_2$ on Cu(001) suggests their properties are similar. As $NdPc_2$ is calculated to not have a ligand spin, this suggests $DyPc_2$ on Cu(001) also does not have a delocalised electron on the top ligand. Also in contrast to measurements of $TbPc_2$ and YPc_2 on Au(111), the Fano line shape is also observed over the centre and is asymmetric.

The spectra shown in Fig. 9.7 has been fitted with the formula

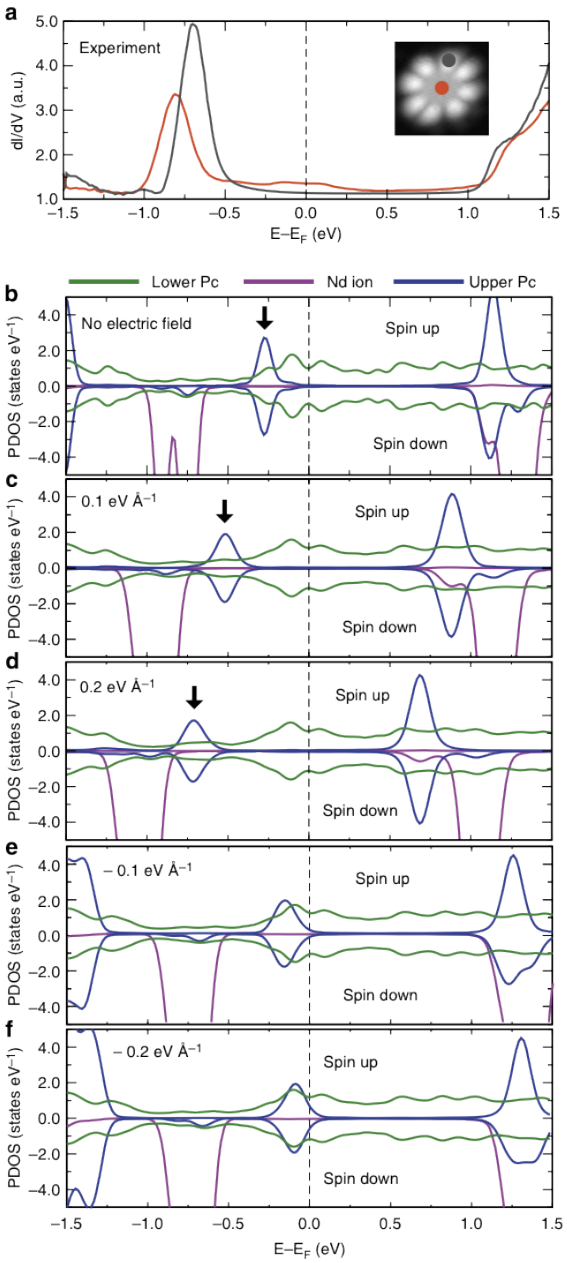

Figure 9.6: Measurements and DFT on $NdPc_2$ from Fahrendorf et al. [142]. Panel a) shows spectra taken on the ligand and centre of the molecule. For spectra taken on the centre a peak is seen at -0.7V due to the 4f states. For spectra taken on the ligand a peak is is observed at -0.6V. This is due to the electrostatic field between the tip and the sample pushing the ligand states to higher voltages until they are pinned by hybridisation with the 4f states. Evidence for this effect is shown in the DFT calculations detailed in Panel b)

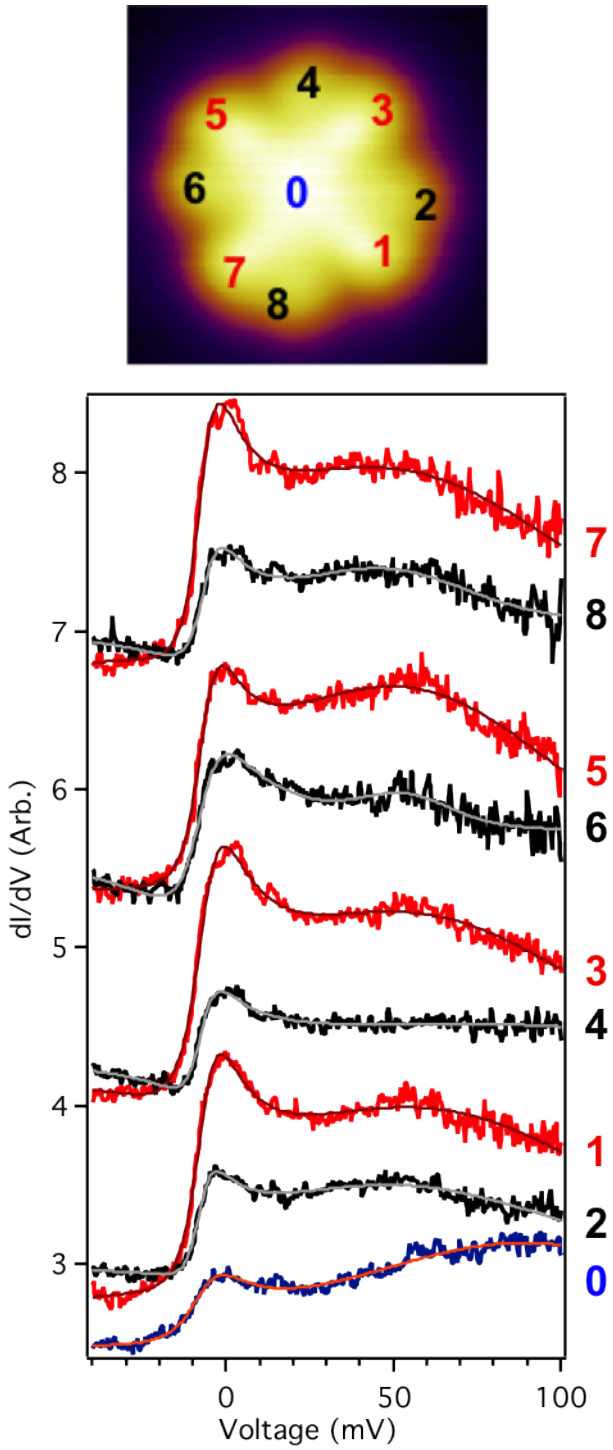

Figure 9.7: dI/dV spectroscopy over $DyPc_2$. On the ligands a clear difference in amplitude is observed on alternating ligands. A fano feature is observed near 0V and a peak around 40mV. The data has been fitted with Eqn 9.1. (V_{set}=-0.1V, I_{set}=0.5nA)

$$\frac{dI}{dV} = C + \frac{A_{Fano}}{(1+q^2)} \frac{(q + \frac{V-E_k}{\Gamma})^2}{(1 + (\frac{V-E_k}{\Gamma})^2} + A_{Gauss} e^{(\frac{V-x_0}{W})^2} \tag{9.1}$$

This formula contains three terms, the offset of the spectra (C), the Fano line shape (as described in Chap 3), and the Gaussian line shape which is composed of the amplitude 'A_{Gauss}', the offset from Fermi energy 'x_0' and width 'W'. The gaussian is fitted to account for the peak observed at positive bias, this has been observed before on $TbPc_2$ [53], and for MnPc on Ag(001) [181]. Here it was ascribed to the formation of a many-body singlet state between the $d_{xy/yz}$ orbitals and the states of the Pc ring.

The clearest feature of the data is that the amplitude of each spectrum varies significantly between the lobes of each arm of the molecule. This variance in amplitude is seen for both the Fano line shape and the peak. The amplitude of the Fano line shape physically represents the coupling of the tip to the unscreened continuum. Figure 9.8 shows a dI/dV slice at -3mV and the calculated ligand states for $NdPc_2$. Comparing both point spectroscopy and dI/dV slices with those calculated for $NdPc_2$, we see that the variation in amplitude is a match to the calculated density of states of the ligand at low bias [142]. This therefore suggests that the continuum is also formed by the ligand states present in the top Pc ring of the molecule.

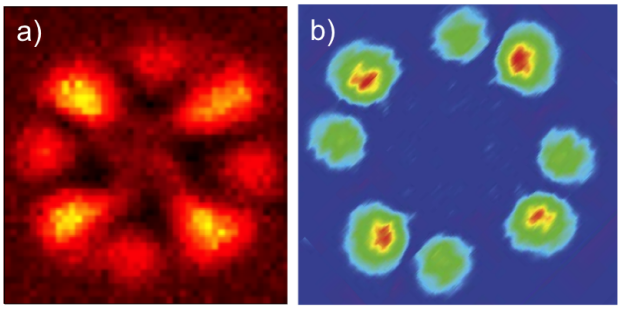

Figure 9.8: a) dI/dV cut at -3mV. b) Calculation of ligand states of $NdPc_2$ at -0.2V [142]. The asymmetry in each arm is the same in both. The calculation has been rotated to align crystal axis and reflected to match binding angle of dI/dV cut, details of this manipulation is shown in the appendix. (V_{set}=-0.1V, I_{set}=0.4nA)

As the 4f states of the Dy ion is the only magnetic moment in the system, it must be the screening of these states that creates the Kondo resonance. That the Kondo resonance is created through the 4f states explains the difference between previous

results on $LnPc_2$ molecules for which Kondo is seen due to a delocalised electron on the ligand.

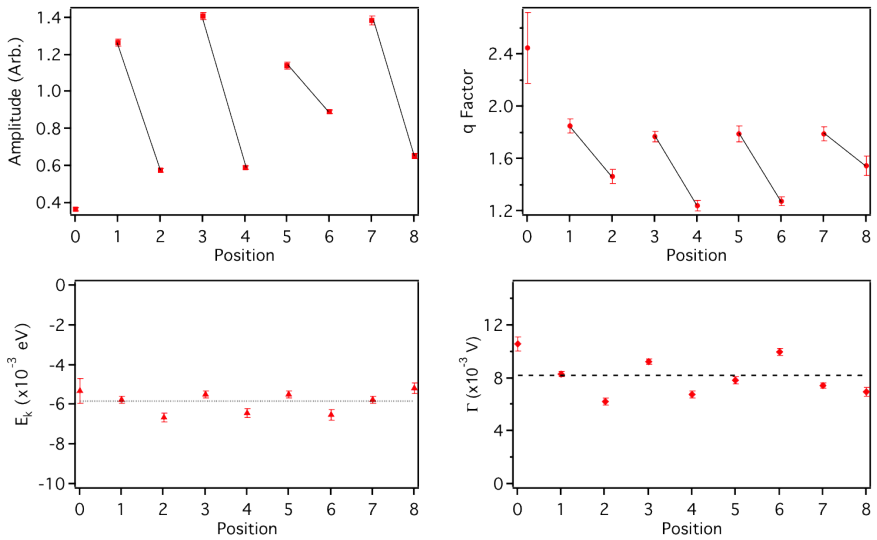

Figure 9.9: The Fano fit parameters of the spectra shown in Fig 9.7 (positions are the same, with 0 being the centre). Γ and E_k show little variation across the molecule, the dotted line represents the mean value. The amplitude and the q factor show a big/small behaviour, however in the case of the q factor this difference is not observed on other molecules

The fit parameter Γ does not vary significantly across the molecule, with average value of 8.2 ± 1.5mV. This suggests that the coupling of the resonance to the continuum remains constant across the molecule. The energy can converted to T_k through using the formula for the Kondo temperature, based on Fermi liquid theory [43].

$$\Gamma = 2\sqrt{(\pi k_b T)^2 + 2(k_b T_k)^2} \tag{9.2}$$

This gives a temperature of 33.2K, which is higher than might be expected for a Kondo effect created by 4f state of a single atom [26]. However as the continuum involves the ligand states of the molecule, which surround the atom, the appropriate energy comparison is not to a metal atom on a surface but to a subsurface metal atom. This has been seen to significantly increase the Kondo temperature of a single dopant [182].

As seen in Fig 9.9, we find that the energy of the Kondo resonance $E_k = -5.6 \pm$

0.5mV. The occupancy of the Kondo resonance can be estimated from E_k and Γ by using the simple single orbital Anderson model [145, 183],

$$< n >= \frac{1}{2} - \frac{1}{\pi} \arctan\left(\frac{E_k}{\Gamma}\right) \tag{9.3}$$

where $< n >$ is the occupancy of the level. The occupancy of the level is calculated to be 0.7, for Dy^{+3} the f-shell has an occupancy of 0.64 ($\frac{9}{14}$). This adds further evidence that the Kondo resonance is created due to the interaction of the conduction electrons with the f-shell magnetic moment. However a necessary caveat is that the simple Anderson model cannot explain the full Kondo physics of the Dy ion, and therefore this result should not be considered conclusive.

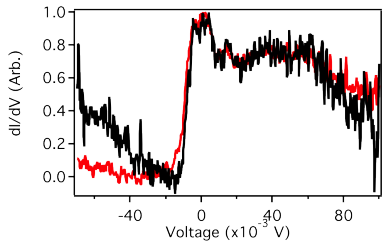

Figure 9.10: Two spectra (7, 8) from Fig 9.7 which have been scaled to have equal amplitude. The variance in q factor appears to be due to the different background conductance at negative bias. (V_{set}=-0.1V, I_{set}=0.5nA)

The q factor of the Fano physically represents the ratio of tunnelling from the tip to the resonance to the tunnelling from the tip to the continuum and is symmetric across the molecule.The q factor is approximately 1.5 which suggests that a slightly larger proportion of the tunnelling is through the resonance than the continuum, agreeing with the conclusion from Fahrendorf et.al. that the coupling between rings is through the 4f states.

From the fits, the q factor shows a similar asymmetrical behaviour between the lobes of each arm as the amplitude. In Fig 9.10, the spectra have been normalised to remove the variation in amplitude. We see that features at positive bias for each lobe match closely, and the difference in q factor is due to the small differences at negative bias. It is therefore likely the variance in q is due to the difference in the background conductance at negative bias.

The variation in the amplitude shows that tunnelling into the continuum varies, and

the q factor (the ratio) is constant. Therefore the tunnelling into the resonance must also vary across the molecule. This suggests that the amount of tunnelling through the 4f states can be controlled by tunnelling through the molecule in different locations.

9.5 Conclusion

Here we show that the binding angle of the molecule breaks the symmetry of the system, and this creates an asymmetry in the top ligand states. A Fano line shape is observed, which is indicative of a Kondo effect. Through mapping the variance in amplitude we show the ligand states create the continuum and that the Kondo resonance is created via the 4f states. This is made possible due to the greater hybridisation between the surface and the molecule than in previous experiments where coupling to the ligand spin was measured. This work not only demonstrates the importance that coupling to the surface plays on the properties of molecules but also shows that by controlling the coupling of the leads, the accessibility of spins can be controlled.

9.6 Future Work

A complementary experiment to confirm our analysis that the increased coupling on Cu creates the observed effect is to to measure $DyPc_2$ on Au. We would expect the Fano line shape to disappear and a peak to occur on the ligand as seen in previous work on $TbPc_2$.

The magnetic moment can also be explored using using x-ray measurements. In Fig 9.11, XMCD measurements are shown for a submonolayer of $DyPc_2$ on Cu(001) at 2K. These results were taken in SOLEIL, France in collaboration with Matteo Mannini from the group of Roberta Sessoli. The top graph shows XAS spectra taken at the Dy edge for both left handed and right handed polarised x-rays. The bottom graph shows the XMCD spectra. The clear XMCD signal shows that the Dy atom retains its magnetic moment on Cu(001). Similar results have also been observed for $TbPc_2$ [91]. In collaboration with the Sessoli group, we are currently

exploring whether any changes in the x-ray data would be expected due to the Kondo physics.

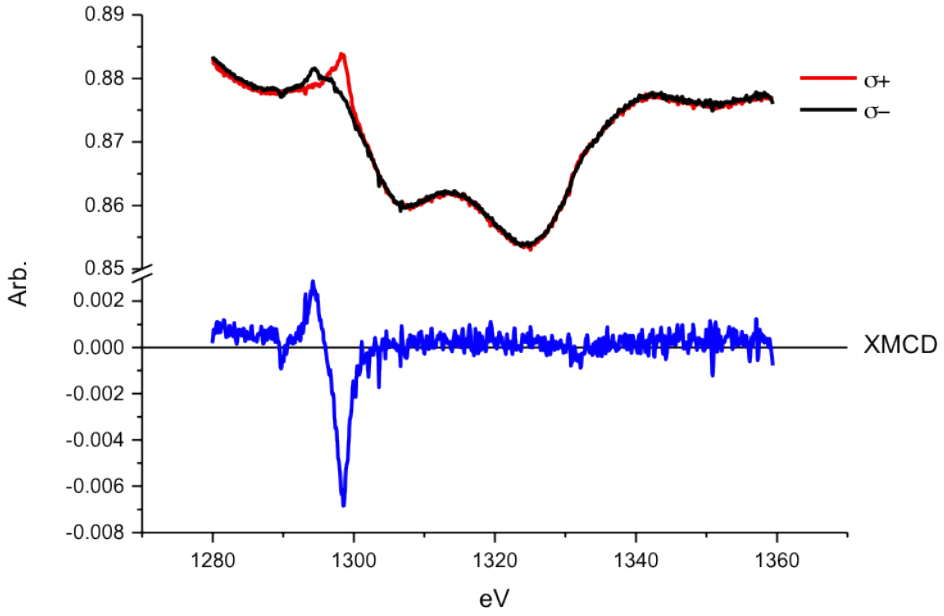

Figure 9.11: XAS and XMCD measurements on a submonolayer of $DyPc_2$ on Cu(001) at 2K. A clear XMCD signal is measured, showing the Dy ion retains its magnetic moment on the Cu(001) surface. The data shown is taken with the sample normal to the x-ray beam and for both right (σ^+) and left (σ^-) circularly polarised x-rays.

Chapter 10

Conclusion

10.1 Summary

In this thesis we have investigated the interaction of molecules with the surface through the use of STM. We have shown that the position of magnetic molecules on a surface can be controlled through their interaction with Cu_2N islands. It is then shown that when FePc is placed on a Cu_2N monolayer, the properties of the molecule are defined by the binding site of the central atom. We showed evidence that both the electronic and magnetic properties are greatly affected.

We observed negative differential resistance (NDR) in electrical transport through FePc molecule on a Cu_2N monolayer. NDR is created due to transient charging of the molecule when the molecular levels align with the Fermi level of Cu. The asymmetry of the junction creates an enhancement of energy scale; this results in the NDR showing a field dependence two orders of magnitude larger than the intrinsic Zeeman shift. These findings represent a new basis for making magnetoresistance devices at the single molecule scale and show that asymmetric coupling could allow for investigations of effects with energy scales which otherwise could not be measured.

We demonstrated that it is possible to interact directly with the f-shell magnetic moment when the $DyPc_2$ is strongly coupled to the surface. A Fano line shape is observed at the Fermi energy, which is caused by the interference between tunnelling into the continuum and into a resonance caused by the Kondo effect. This is in

contrast to previous measurements on a less reactive substrate, where Kondo was observed due to spin on the ligand. This suggests that by controlling the coupling of the leads it is possible to control which molecules are accessed during electrical transport.

We demonstrated how engineering the coupling to the surface allows for the measurement of novel properties, be that in the low coupling regime (NDR), or the strongly coupled regime (transport through the 4f magnetic moment). This thesis demonstrates the importance of interaction in the defining the properties of a molecule on a surface. This suggests that in single molecule devices, controlling the coupling of leads to molecule may provide a route to attaining the required attributes.

10.2 Future Work

In this work we have studied magnetic molecules on metals and thin insulators. An interesting new direction to take this work would be to place molecules onto a surface which has spin properties. A simple example of this would be to place the molecule on ferromagnets, however more complicated systems exist as well. In topological insulators, spin orbit interaction replace the external magnetic field in the quantum hall effect, creating quantum Hall-like effects on the surface of the materials. These surface states are immune to back scattering as only one direction is allowed on each edge of the sample due to time reversal symmetry. The time reversal symmetry of the surface state can be broken via a magnetic field or a magnetic impurity. The advantage of using a magnetic impurity is that not only can the disruption to the surface state be measured, but also it is possible to measure how the surface state affects the magnetic impurity. This may cause the loss of topological protection and open a gap in the surface states. Therefore one way to expand the area of study is to place magnetic molecules onto topological insulators.

Chapter 11

Appendix

DFT calculations of FePc on Cu_2N.

Information provided by Mats Persson

The electronic and geometric structure of FePc on Cu_2N/Cu(001) has been investigated by density functional theory (DFT) calculations using the Vienna ab-initio simulation program (VASP) [184]. The electron-ion-core interactions were handled using the projected augmented wave (PAW) method [185]. The exchange-correlation effects were treated using the optB86B version of the van der Waals density functional [186] and by introducing an intra Coulomb U term according to Dudarev's scheme [187]. The Cu(001) surface is represented in a super cell by a six layer slab with a c(12x12) surface unit cell and a 16.2Å vacuum region. The atoms in the bottom two layers were constrained at their bulk positions with a calculated lattice constant of 3.60 Å during the relaxations and geometries were relaxed until all forces were less than 0.02 eVÅ^{-1}. The same super cell was used for the isolated molecule. A plane-wave, kinetic energy cut-off of 400 eV was used and the Brillouin zone was sampled at the Gamma point.

The employed DFT+U scheme combined with the used van der Waals potential was found to give an adequate description of the electronic structure of the isolated molecule when using the bulk value of 3.2 eV for U-J [188]. The calculated spin magnetic moment is $2\mu_B$B and the density of states of different partial waves around

the Fe atom (Fig 11.1) indicates that the electronic configuration of the Fe d block corresponds to the configuration of $(d_{z2})^1$,$(d_\pi)^3$, $(d_{xy})^2$. The calculated spin moment and electronic configuration are in agreement with experiments of FePc thin films [189] and bulk FePc [190].

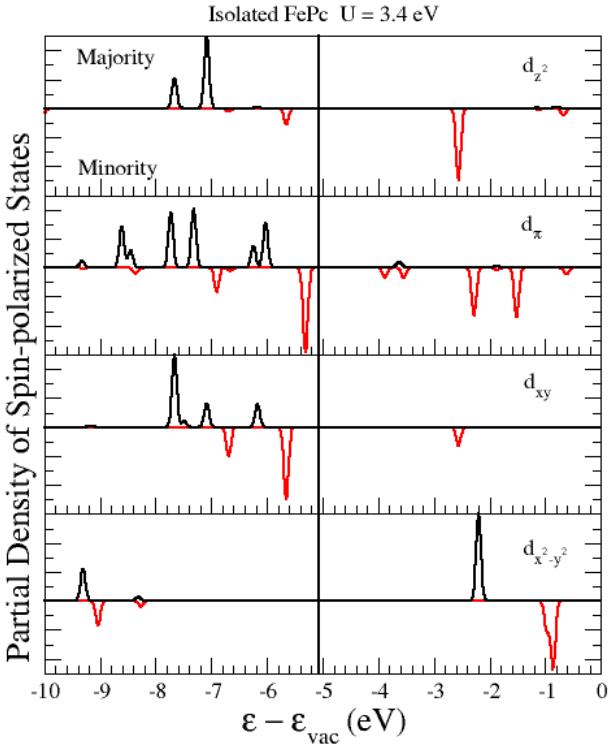

Figure 11.1: Calculated spin-polarized density of states for various majority (black) and minority (red) d partial waves around the Fe atom as indicated. The d_π block includes the d_{xz} and d_{yz} states, where x is along a Fe-N direction and z is perpendicular to the molecular plane..

Two different adsorption sites and for each site four different orientations of the molecule were calculated. The resulting adsorption energies and spin magnetic moments are shown in Table 11.1. The binding angles ϕ refer to the initial orientation of one of the inner N atoms of the molecule with respect to the [100] direction of Cu substrate and this angle changes with less than 0.40 during the structural relaxation. Note that the C_{4v} symmetry of the FePc molecule makes the system periodic over ϕ with a period of 90°. Furthermore, the C_{4v} symmetry of the N and the C_{2v} symmetry of the Cu site make the systems corresponding to ϕ and 90° - ϕ equivalent by symmetry and it is sufficient to restrict the interval of ϕ to [0°,45°].

N site	0 °	15 °	30 °	45 °
E_{ads} (eV)	-3.59	-3.65	-3.60	-3.67
μ (μ_B)	2.06	2.02	1.98	1.79

Cu site	0 °	15 °	30 °	45 °
E_{ads} (eV)	-3.48	-3.33	-3.40	-3.36
μ (μ_B)	2.00	2.00	1.98	1.98

Table 11.1: Calculated adsorption energies and spin magnetic moments. The N and Cu sites corresponds to the Fe atom being on-top of a N and Cu atom, respectively; the N site corresponds to a fourfold hollow site in the Cu(001) surface.

These results shows that the adsorption energy varies relatively weakly by both the adsorption site and the binding angle and that the spin moment of the isolated molecule is essentially kept. The spin moment is found to be localised at the Fe atom for all adsorption sites and binding angles. The angular dependence of the adsorption energy suggests there are shallow minima for binding angles. Thus these results support the observation that the adsorbed molecule is found in a large distribution of binding angles and sites.

On the N site, the surface N atom is displaced out from the surface by about 0.5 and the Fe atom is displaced towards the surface by about 0.3 from the molecular plane, resulting in Fe-N bonding distance of 2.02 . This relatively short bonding distance indicates the formation of a chemical bond. In contrast to the N site, the N surface atoms and the Fe atom for the Cu shows only minor displacements and the molecule surface distance is relatively large about 3.1- 3.2 and is more characteristic of a physisorption bond. The molecular plane is only slightly distorted at most with about 0.2 for the various sites and orientations.

Synthetic procedure for synthesising $Dy(Pc)_2$

Information provided by Joris van Slageren

Synthesis of Dysprosium (bis)phthalocyanine anion compound [$DyPc_2$] $(NBu4)^+$. 2 dmf [191]

Dysprosium acetate hydrate ($Dy(OAc)_3.4H_2O$) (2.09g, 5.62 mmol) and phthalodinitrile (PDN) (6.40g, 49.9 mmol) were mixed together and heated to 140°C under atmospheric conditions with stirring. After the water had evaporated from the reaction mixture, KOMe (1.15g, 16.4 mmol) was added slowly to the solution. This caused a dark green solid to form. After all the KOMe was added the reaction was left for 10 minutes to react, after which there was only a small amount of solution. Ethylene glycol diethyl ether (5.7 ml) was added and the reaction mixture was left to reflux for 10 minutes and then allowed to cool to room temperature.

The crude product was heated at 140°C under vacuum for 3 hours to remove excess ethylene glycol diethyl ether and unreacted PDN. The dark green/blue crude product was then converted to the anion species (blue) by being dissolved in the minimum amount of DMF, adding a few drops of hydrazine monohydrate to reduce any neutral species to the anion species and a 1.1 equivalent of NBu_4Br (1.46g, 4.53 mmol) to act as a counter cation.

This solution was then concentrated by removing excess DMF by rotary evaporation and eluted through a column of DMF and neutral alumina (deactivated to grade III, 50-200 micron size, 7cm column length). Product was obtained by slow evaporation of the solvent.

MALDI-TOF MS m/z: 1188.3 (negative ionisation) IR (KBr): 728, 809, 883, 1060, 1078, 1113, 1159, 1329, 1384, 1481, 1608cm^{-1} 1H NMR $\delta(CD_3CN)$: -17.9, -41.4ppm UV/Vis (DMF): 332, 621, 682nm

Synthesis of Dysprosium (bis)phthalocyanine anion compound $[DyPc_2]$. CH_2Cl_2

An electrolysis cell was set up with dry dichloromethane (passed over alumina). On one side was the cathode working electrode where $[DyPc_2]^-[NBu_4]^+$ (7.7mg, 5.38 μmol) was dissolved in the dichloromethane (7cm^3). The working electrode was a flat platinum electrode with a 1cm2 surface area. On the other side of the cell was a reference electrode and an anode secondary electrode of Platinum/Rhodium gauze. The electrolyte was $[NBu_4]^+[BF_4]^-$ (0.2M). A constant current of $+5\mu A/cm^2$ was applied.

After about 24 hr the solution had gone from a blue colour to a green colour indicating that the product had been oxidised and dark green small needle like crystals had formed on the bottom of the cell that were very difficult to dissolve. These were found by UV/Vis to be the green neutral product of $[DyPc_2]^0.CH_2Cl_2$

MALDI-TOF MS m/z: 1188 (negative ionisation) IR (KBr): 729, 780, 883, 1060, 1083, 1113, 1319, 1384, 1447, 1485, 1501, 1606cm^{-1} UV/Vis (CH_2Cl_2): 319, 461, 599, 664, 910nm

Modifying figure from Fahrendorf et al.

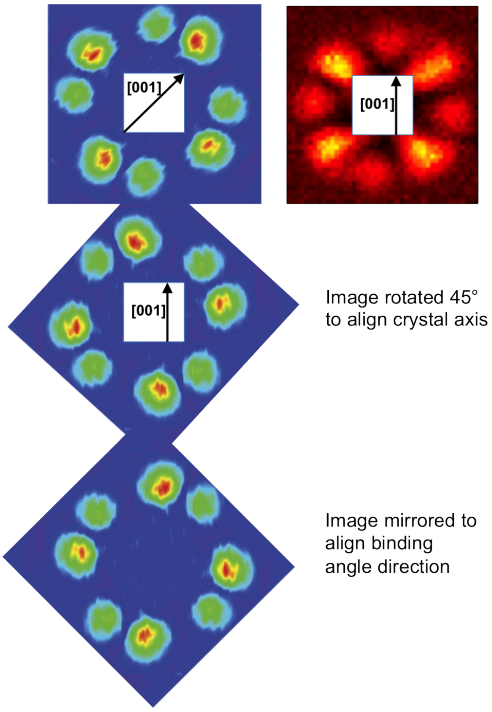

Figure 11.2: Manipulation of the calculation of ligand states in the Fahrendorf et al. [142] to match the measured data.

Weighing the Cryogenic STM

The weight of the Cryogenic STM was estimated by using the air legs that provide passive damping to the system. This was achieved by measuring the pressure required to lift the STM off the ground. To measure the pressures we started at 3 bar, and raised the pressure in steps of 0.5 bar. At each step we allowed the system time to settle and then checked to see if the STM was off the floor. Once all legs of the STM were off the ground, we reduced the pressure by 0.5 bar and moved up by steps of approximately 0.1 bar. This allowed us to find the pressure to an estimated accuracy of $\pm$0.1bar. In order to convert the pressure measurement to a weight, we placed known quantities of weight on the system and used this to calibrate the pressure. In this case we measured the pressure required to raise the STM with 920kg of additional mass, 480kg of additional mass and with no additional mass. The results are shown in the table below

Mass (kg)	Pressure (kPa)
920	370
480	480
0	570

By fitting a straight line through these points, plotting mass against pressure, we can calculate the weight of the system. The equation of the straight line is $y = mx + c$, Where y = pressure in units of Nm^{-2},m=gravitational constant/Area which has the unit Nm^{-2} and c= Mass of STM/m or c=(Mass of STM*Area)/G again with the units Nm^{-2}. In the fitting we get the values $m = 217.569$ and $c = 371801$. This gives us a resulting mass of the Cryogenic STM system of 1713$\pm$100kg.

As way of a proof of principle check we can also calculate the radius of the lifting area on one of the four air legs. On completing this calculation we get a value of 60mm. On visual inspection of the air legs this appears correct, suggesting our calculation of weight is approximately correct.

All readings were taken with the STM empty of cryogens. From the stated volumes of cryogens, LHe = 135L, LN_2 = 75L and densities, LHe = $0.125\mathrm{kgl}^{-1}$, LN_2 = $0.808\mathrm{kgl}^{-1}$, we can calculate the total of the cryogens weight. The total weight of cryogens is 77.5kg, and therefore play little role in the total weight of the system.

Bibliography

[1] S. Wolf, D. Awschalom, R. Buhrman, J. Daughton, S. Von Molnar, M. Roukes, A. Chtchelkanova, and D. Treger, "Spintronics: A spin-based electronics vision for the future," *Science*, vol. 294, no. 5546, p. 1488, 2001.

[2] G. Binasch, P. Grünberg, F. Saurenbach, and W. Zinn, "Enhanced magnetoresistance in layered magnetic structures with antiferromagnetic interlayer exchange," *Physical Review B*, vol. 39, no. 7, p. 4828, 1989.

[3] E. Lörtscher, "Wiring molecules into circuits," *Nature Nanotechnology*, vol. 8, no. 6, pp. 381–384, 2013.

[4] L. Bogani and W. Wernsdorfer, "Molecular spintronics using single-molecule magnets," *Nature Materials*, vol. 7, no. 3, pp. 179–186, 2008.

[5] G. Cook, "Dirty Data," *Greenpeace International*, pp. 1–36, 2011.

[6] C. Hirjibehedin, C. Lin, A. Otte, M. Ternes, C. Lutz, B. Jones, and A. Heinrich, "Large magnetic anisotropy of a single atomic spin embedded in a surface molecular network," *Science*, vol. 317, no. 5842, p. 1199, 2007.

[7] A. F. Otte, M. Ternes, K. v. Bergmann, S. Loth, H. Brune, C. P. Lutz, C. F. Hirjibehedin, and A. J. Heinrich, "The role of magnetic anisotropy in the Kondo effect," *Nature Physics*, vol. 4, p. 847, 2008.

[8] N. Tsukahara, K.-I. Noto, M. Ohara, S. Shiraki, N. Takagi, S. Shin, and M. Kawai, "Adsorption-Induced Switching of Magnetic Anisotropy in a Single Iron(II) Phthalocyanine Molecule on an Oxidized Cu(110) Surface," *Physical Review Letters*, vol. 102, p. 167203, 2009.

[9] P. Gütlich, Y. Garcia, and H. A. Goodwin, "Spin crossover phenomena in Fe(ii) complexes," *Chemical Society Reviews*, vol. 29, no. 6, pp. 419–427, 2000.

[10] P. Maestro and D. Huguenin, "Industrial applications of rare earths: which way for the end of the century," *Journal of Alloys and Compounds*, vol. 225, no. 1, pp. 520–528, 1995.

[11] J. Jensen and A. R. Mackintosh, "Rare earth magnetism," *Clarendon Press, Oxford*, 1991.

[12] D. Gatteschi, R. Sessoli, and J. Villain, "Molecular Nanomagnets," *Oxford University Press*, 2010.

[13] M. N. Leuenberger and D. Loss, "Quantum computing in molecular magnets," *Nature*, vol. 410, no. 6830, pp. 789–793, 2001.

[14] R. Sessoli, D. Gatteschi, A. Caneschi, and M. A. Novak, "Magnetic bistability in a metal-ion cluster," *Nature*, vol. 365, no. 6442, pp. 141–143, 1993.

[15] F. Neese and D. A. Pantazis, "What is not required to make a single molecule magnet," *Faraday Discussions*, vol. 148, p. 229, 2010.

[16] D. N. Woodruff, R. E. P. Winpenny, and R. A. Layfield, "Lanthanide Single-Molecule Magnets," *Chemical Reviews*, vol. 113, pp. 5110–5148, July 2013.

[17] N. Ishikawa, M. Sugita, T. Ishikawa, S. Koshihara, and Y. Kaizu, "Lanthanide double-decker complexes functioning as magnets at the single-molecular level," *Journal Of The American Chemical Society*, vol. 125, pp. 8694–8695, 2003.

[18] S. Kahle, Z. Deng, N. Malinowski, C. Tonnoir, A. Forment-Aliaga, N. Thontasen, G. Rinke, D. Le, V. Turkowski, T. S. Rahman, S. Rauschenbach, M. Ternes, and K. Kern, "The Quantum Magnetism of Individual Manganese-12-Acetate Molecular Magnets Anchored at Surfaces," *Nano Letters*, vol. 12, pp. 518–521, 2012.

[19] K. Sun, K. Park, J. Xie, J. Luo, H. Yuan, Z. Xiong, J. Wang, and Q. Xue, "Direct Observation of Molecular Orbitals in an Individual Single-Molecule Magnet Mn 12on Bi(111)," *ACS Nano*, vol. 7, pp. 6825–6830, 2013.

[20] K. Katoh, Y. Yoshida, M. Yamashita, H. Miyasaka, B. K. Breedlove, T. Kajiwara, S. Takaishi, N. Ishikawa, H. Isshiki, Y.-F. Zhang, T. Komeda, M. Yam-

agishi, and J. Takeya, "Direct observation of lanthanide(III)-phthalocyanine molecules on Au(111) by using scanning tunneling microscopy and scanning tunneling spectroscopy and thin-film field-effect transistor properties of Tb(III)- and Dy(III)-phthalocyanine molecules.," *Journal Of The American Chemical Society*, vol. 131, no. 29, pp. 9967–9976, 2009.

[21] Binney and Skinner, "The Physics of Quantum Mechanics," *Clarendon Press, Oxford*, 2009.

[22] R. White, "Quantum Theory Of Magnetism ," *Springer*, 2007.

[23] A. Bringer, "Heisenberg Model - Magnetic Interactions," *Magnetism goes nano, summer school*, 2005.

[24] G. D. Scott and D. Natelson, "Kondo Resonances in Molecular Devices," *ACS Nano*, vol. 4, pp. 3560–3579, 2010.

[25] J. Kondo, "Resistance Minimum in Dilute Magnetic Alloys," *Progress of Theoretical Physics*, vol. 32, p. 37, 1964.

[26] M. Ternes, A. J. Heinrich, and W. Schneider, "Spectroscopic manifestations of the Kondo effect on single adatoms," *J. Phys.: Condens. Matter*, vol. 21, no. 5, p.053001, 2009.

[27] H. Brune and P. Gambardella, "Magnetism of individual atoms adsorbed on surfaces," *Surface Science*, vol. 603, pp. 1812–1830, June 2009.

[28] H. Brune, "Probing magnetism at the nanoscale," *Nature Nano* , p.674, Oct. 2007.

[29] C. Julian Chen, "Introduction to scanning tunneling microscopy," *Oxford University Press* 1993.

[30] M. Ternes, "Scanning tunneling spectroscopy at the single atom scale," *Thesis*, TU Berlin, Feb. 2006.

[31] G. Binnig, H. Rohrer, C. Gerber, and E. Weibel, "7x7 reconstruction on Si (111) resolved in real space," *Physical Review Letters*, vol. 50, no. 2, p. 120, 1983.

[32] M. Crommie, C. Lutz, and D. Eigler, "Imaging standing waves in a two-dimensional electron gas," *Nature*, vol.363, p.524, 1993.

[33] A. Yakunin, A. Silov, P. Koenraad, J. Wolter, W. van Roy, J. de Boeck, J.-M. Tang, and M. Flatté, "Spatial Structure of an Individual Mn Acceptor in GaAs," *Physical Review Letters*, vol. 92, p. 216806, 2004.

[34] J. A. Stroscio, R. M. Feenstra, and A. P. Fein, "Electronic structure of the Si (111) 2 1 surface by scanning-tunneling microscopy," *Physical Review Letters*, vol. 57, no. 20, p. 2579, 1986.

[35] H. Hess, R. Robinson, , J. Valles, and J. Waszczak, "Scanning-Tunnelling-Microscope Oservation of the Abrikosov Flux Lattice and the Density of States near and inside a Fluoid ," *Physical Review Letters*, vol. 62, pp. 214–216, 2010.

[36] P. Mallet, W. Sacks, D. Roditchev, D. Defourneau, and J. Klein, "Spatial and energy variation of the local density of states in the charge density wave phase of 2H-NbSe2," *Journal Of Vacuum Science & Technology B*, vol. 14, pp. 1070–1074, 1996.

[37] H. J. Lee, W. Ho, and M. Persson, "Spin Splitting of s and p States in Single Atoms and Magnetic Coupling in Dimers on a Surface," *Physical Review Letters*, vol. 92, p. 186802, 2004.

[38] D. Kitchen, A. Richardella, J.-M. Tang, M. E. Flatté, and A. Yazdani, "Atom-by-atom substitution of Mn in GaAs and visualization of their hole-mediated interactions," *Nature*, vol. 442, pp. 436–439, 2006.

[39] M. Grobis, X. Lu, and M. Crommie, "Local electronic properties of a molecular monolayer:C60 on Ag(001)," *Physical Review B*, vol. 66, p. 161408, 2002.

[40] J. Repp, G. Meyer, S. Stojkovic, A. Gourdon, and C. Joachim, "Molecules on insulating films: Scanning-tunneling microscopy imaging of individual molecular orbitals," *Physical Review Letters*, vol. 94, p. 026803, 2005.

[41] V. Madhavan, W. Chen, T. Jamneala, M. Crommie, and N. Wingreen, "Tunneling into a single magnetic atom: Spectroscopic evidence of the Kondo resonance," *Science*, vol. 280, pp. 567–569, 1998.

[42] U. Fano, "Effects of configuration interaction on intensities and phase shifts," *Physical Review*, vol. 124, no. 6, p. 1866, 1961.

[43] K. Nagaoka, T. Jamneala, M. Grobis, and M. Crommie, "Temperature Dependence of a Single Kondo Impurity," *Physical Review Letters*, vol. 88, p. 077205, 2002.

[44] N. Knorr, M. Schneider, L. Diekhöner, P. Wahl, and K. Kern, "Kondo Effect of Single Co Adatoms on Cu Surfaces," *Physical Review Letters*, vol. 88, p. 096804, 2002.

[45] W. Chen, T. Jamneala, V. Madhavan, and M. F. Crommie, "Disappearance of the Kondo resonance for atomically fabricated cobalt dimers," *Physical Review B*, vol. 60, no. 12, p. R8529, 1999.

[46] J. Bork, Y.-h. Zhang, L. Diekhöner, L. Borda, P. Simon, J. Kroha, P. Wahl, and K. Kern, "A tunable two-impurity Kondo system in an atomic point contact," *Nature Physics*, vol. 7, pp. 901–906, 2011.

[47] P. Wahl, L. Diekhöner, G. Wittich, L. Vitali, M. A. Schneider, and K. Kern, "Kondo Effect of Molecular Complexes at Surfaces: Ligand Control of the Local Spin Coupling," *Physical Review Letters*, vol. 95, 2005.

[48] A. Zhao, Q. Li, L. Chen, H. Xiang, W. Wang, S. Pan, B. Wang, X. Xiao, J. Yang, J. G. Hou, and Q. Zhu, "Controlling the Kondo Effect of an Adsorbed Magnetic Ion Through Its Chemical Bonding," *Science*, vol. 309, p. 1542, 2005.

[49] E. Minamitani, N. Tsukahara, D. Matsunaka, Y. Kim, N. Takagi, and M. Kawai, "Symmetry-Driven Novel Kondo Effect in a Molecule," *Physical Review Letters*, vol. 109, p. 086602, 2012.

[50] I. Fernández-Torrente, K. J. Franke, and J. I. Pascual, "Vibrational Kondo effect in pure organic charge-transfer assemblies," *Physical Review Letters*, vol. 101, no. 21, p. 217203, 2008.

[51] Y.-h. Zhang, S. Kahle, T. Herden, C. Stroh, M. Mayor, U. Schlickum, M. Ternes, P. Wahl, and K. Kern, "Temperature and magnetic field dependence of a Kondo system in the weak coupling regime," *Nature Communications*, vol. 4, 2013.

[52] L. Gao, W. Ji, Y. B. Hu, Z. H. Cheng, Z. T. Deng, Q. Liu, N. Jiang, X. Lin, W. Guo, S. X. Du, W. A. Hofer, X. C. Xie, and H.-J. Gao, "Site-Specific Kondo Effect at Ambient Temperatures in Iron-Based Molecules," *Physical Review Letters*, vol. 99, 2007.

[53] T. Komeda, H. Isshiki, J. Liu, Y.-F. Zhang, N. a. s. Lorente, K. Katoh, B. K. Breedlove, and M. Yamashita, "Observation and electric current control of a local spin in a single-molecule magnet," *Nature Communications*, vol. 2, pp. 217–217, 2011.

[54] R. Wiesendanger, H.-J. Güntherodt, G. Güntherodt, R. J. Gambino, and R. Ruf, "Observation of vacuum tunneling of spin-polarized electrons with the scanning tunneling microscope," *Physical Review Letters*, vol. 65, p. 247, 1990.

[55] R. Wiesendanger, "Spin mapping at the nanoscale and atomic scale," *Reviews of Modern Physics*, vol. 81, pp. 1495–1550, 2009.

[56] A. Kubetzka, M. Bode, O. Pietzsch, and R. Wiesendanger, "Spin-Polarized Scanning Tunneling Microscopy with Antiferromagnetic Probe Tips," *Physical Review Letters*, vol. 88, p. 057201, 2002.

[57] S. Loth, K. v. Bergmann, M. Ternes, A. F. Otte, C. P. Lutz, and A. J. Heinrich, "Controlling the state of quantum spins with electric currents," *Nature Physics*, vol. 6, pp. 340–344, 2010.

[58] U. Schlickum, W. Wulfhekel, and J. Kirschner, "Spin-polarized scanning tunneling microscope for imaging the in-plane magnetization," *Applied Physics Letters*, vol. 83, p. 2016, 2003.

[59] S. Heinze, M. Bode, A. Kubetzka, O. Pietzsch, X. Nie, S. Blugel, and R. Wiesendanger, "Real-space imaging of two-dimensional antiferromagnetism on the atomic scale," *Science*, vol. 288, pp. 1805–1808, 2000.

[60] F. Meier, L. Zhou, J. Wiebe, and R. Wiesendanger, "Revealing Magnetic Interactions from Single-Atom Magnetization Curves," *Science*, vol. 320, p. 82, 2008.

[61] C. Iacovita, M. Rastei, B. Heinrich, T. Brumme, J. Kortus, L. Limot, and J. Bucher, "Visualizing the Spin of Individual Cobalt-Phthalocyanine Molecules," *Physical Review Letters*, vol. 101, p. 116602, 2008.

[62] D. Serrate, P. Ferriani, Y. Yoshida, S.-W. Hla, M. Menzel, K. von Bergmann, S. Heinze, A. Kubetzka, and R. Wiesendanger, "Imaging and manipulating the spin direction of individual atoms," *Nature Nanotechnology*, vol. 5, no. 5, pp. 350–353, 2010.

[63] B. Persson and A. Baratoff, "Inelastic electron tunneling from a metal tip: the contribution from resonant processes," *Physical Review Letters*, vol. 59, no. 3, p. 339, 1987.

[64] A. Kogan, S. Amasha, D. Goldhaber-Gordon, G. Granger, M. Kastner, and H. Shtrikman, "Measurements of Kondo and spin splitting in single-electron transistors," *Physical Review Letters*, vol. 93, p. 166602, 2004.

[65] J. Lambe and R. C. Jaklevic, "Molecular vibration spectra by inelastic electron tunneling," *Physical Review*, vol. 165, no. 3, p. 821, 1968.

[66] L. J. Lauhon and W. Ho, "Effects of temperature and other experimental variables on single molecule vibrational spectroscopy with the scanning tunneling microscope," *Review Of Scientific Instruments*, vol. 72, no. 1, p. 216, 2001.

[67] B. C. Stipe, M. A. Rezaei, and W. Ho, "Single-Molecule Vibrational Spectroscopy and Microscopy," *Science*, vol. 280, p. 1732, 1998.

[68] W. Ho, "Single-molecule chemistry," *The Journal of Chemical Physics*, vol. 117, p. 11033, 2002.

[69] A. Heinrich, J. Gupta, C. Lutz, and D. Eigler, "Single-atom spin-flip spectroscopy," *Science*, vol. 306, no. 5695, p. 466, 2004.

[70] C. Hirjibehedin, C. Lutz, and A. Heinrich, "Spin coupling in engineered atomic structures," *Science*, vol. 312, pp. 1021–1024, 2006.

[71] T. Choi, C. D. Ruggiero, and J. A. Gupta, "Tunneling spectroscopy of ultrathin insulating Cu2N films, and single Co adatoms," *Journal Of Vacuum Science & Technology B*, vol. 27, pp. 887–890, 2009.

[72] A. Otte, M. Ternes, S. Loth, C. Lutz, C. Hirjibehedin, and A. Heinrich, "Spin Excitations of a Kondo-Screened Atom Coupled to a Second Magnetic Atom," *Physical Review Letters*, vol. 103, p. 107203, 2009.

[73] A. A. Khajetoorians, B. Chilian, J. Wiebe, S. Schuwalow, F. Lechermann, and R. Wiesendanger, "Detecting excitation and magnetization of individual dopants in a semiconductor," *Nature*, vol. 467, pp. 1084–1087, 2010.

[74] A. Khajetoorians, S. Lounis, B. Chilian, A. Costa, L. Zhou, D. Mills, J. Wiebe, and R. Wiesendanger, "Itinerant Nature of Atom-Magnetization Excitation by Tunneling Electrons," *Physical Review Letters*, vol. 106, 2011.

[75] X. Chen, Y.-S. Fu, S.-H. Ji, T. Zhang, P. Cheng, X.-C. Ma, X.-L. Zou, W.-H. Duan, J.-F. Jia, and Q.-K. Xue, "Probing Superexchange Interaction in Molecular Magnets by Spin-Flip Spectroscopy and Microscopy," *Physical Review Letters*, vol. 101, p. 197208, 2008.

[76] Y.-S. Fu, T. Zhang, S.-H. Ji, X. Chen, X.-C. Ma, J.-F. Jia, and Q.-K. Xue, "Identifying Charge States of Molecules with Spin-Flip Spectroscopy," *Physical Review Letters*, vol. 103, p. 257202, 2009.

[77] B. Chilian, A. Khajetoorians, S. Lounis, A. Costa, D. Mills, J. Wiebe, and R. Wiesendanger, "Anomalously large g factor of single atoms adsorbed on a metal substrate," *Physical Review B*, vol. 84, p. 212401, 2011.

[78] T. Schuh, T. Balashov, T. Miyamachi, A. F. Takács, S. Suga, and W. Wulfhekel, "Lifetimes of magnetic excitations in Fe and Co atoms and clusters on Pt(111)," *Journal of Applied Physics*, vol. 107, no. 9, p. 09E156, 2010.

[79] S. Loth, M. Etzkorn, C. P. Lutz, D. M. Eigler, and A. J. Heinrich, "Measurement of Fast Electron Spin Relaxation Times with Atomic Resolution," *Science*, vol. 329, pp. 1628–1630, 2010.

[80] S. Loth, S. Baumann, C. P. Lutz, D. M. Eigler, and A. J. Heinrich, "Bistability in Atomic-Scale Antiferromagnets," *Science*, vol. 335, pp. 196–199, 2012.

[81] T. Miyamachi, T. Schuh, T. Märkl, C. Bresch, T. Balashov, A. Stöhr, C. Karlewski, S. André, M. Marthaler, and M. Hoffmann, "Stabilizing the magnetic

moment of single holmium atoms by symmetry," *Nature*, vol. 503, no. 7475, pp. 242–246, 2013.

[82] A. A. Khajetoorians, B. Baxevanis, C. Hubner, T. Schlenk, S. Krause, T. O. Wehling, S. Lounis, A. Lichtenstein, D. Pfannkuche, J. Wiebe, and R. Wiesendanger, "Current-Driven Spin Dynamics of Artificially Constructed Quantum Magnets," *Science*, vol. 339, pp. 55–59, 2013.

[83] F. U. Hillebrecht, "X-Ray Magnetic Dichroism," *Magnetism goes nano, summer school*, 2005.

[84] H. Ebert, "Magneto-optical effects in transition metal systems," *Reports on Progress in Physics*, vol. 59, no. 12, p. 1665, 1996.

[85] A. Cornia, M. Mannini, P. Sainctavit, and R. Sessoli, "Chemical strategies and characterization tools for the organization of single molecule magnets on surfaces," *Chemical Society Reviews*, vol. 40, no. 6, p. 3076, 2011.

[86] P. Gambardella, S. Dhesi, S. Gardonio, C. Grazioli, P. Ohresser, and C. Carbone, "Localized Magnetic States of Fe, Co, and Ni Impurities on Alkali Metal Films," *Physical Review Letters*, vol. 88, p. 047202, 2002.

[87] P. Gambardella, A. Dallmeyer, K. Maiti, M. C. Malagoli, W. Eberhardt, K. Kern, and C. Carbone, "Ferromagnetism in one-dimensional monatomic metal chains," *Nature*, vol. 416, p. 301, 2002.

[88] S. Stepanow, A. Mugarza, G. Ceballos, P. Moras, J. C. Cezar, C. Carbone, and P. Gambardella, "Giant spin and orbital moment anisotropies of a Cu-phthalocyanine monolayer," *Physical Review B*, vol. 82, p. 014405, 2010.

[89] M. Mannini, F. Pineider, P. Sainctavit, C. Danieli, E. Otero, C. Sciancalepore, A. M. Talarico, M.-A. Arrio, A. Cornia, D. Gatteschi, and R. Sessoli, "Magnetic memory of a single-molecule quantum magnet wired to a gold surface," *Nature Materials*, vol. 8, pp. 194–197, 2009.

[90] M. Mannini, F. Pineider, C. Danieli, F. Totti, L. Sorace, P. Sainctavit, M. A. Arrio, E. Otero, L. Joly, J. C. Cezar, A. Cornia, and R. Sessoli, "Quantum tunnelling of the magnetization in a monolayer of oriented single-molecule magnets," *Nature*, vol. 468, pp. 417–421, 2010.

[91] S. Stepanow, J. Honolka, P. Gambardella, L. Vitali, N. Abdurakhmanova, T.-C. Tseng, S. Rauschenbach, S. L. Tait, V. Sessi, S. Klyatskaya, M. Ruben, and K. Kern, "Spin and Orbital Magnetic Moment Anisotropies of Monodispersed Bis(Phthalocyaninato)Terbium on a Copper Surface," *Journal Of The American Chemical Society*, vol. 132, pp. 11900–11901, 2010.

[92] L. Margheriti, D. Chiappe, M. Mannini, P.-E. Car, P. Sainctavit, M.-A. Arrio, F. B. de Mongeot, J. C. Cezar, F. M. Piras, A. Magnani, E. Otero, A. Caneschi, and R. Sessoli, "X-Ray Detected Magnetic Hysteresis of Thermally Evaporated Terbium Double-Decker Oriented Films," *Advanced Materials*, vol. 22, pp. 5488–5493, 2010.

[93] A. L. Rizzini, C. Krull, T. Balashov, J. J. Kavich, A. Mugarza, P. S. Miedema, P. K. Thakur, V. Sessi, S. Klyatskaya, M. Ruben, S. Stepanow, and P. Gambardella, "Coupling single molecule magnets to ferromagnetic substrates," *Physical Review Letters*, vol. 107, no. 17, p. 177205, 2011.

[94] L. Malavolti, L. Poggini, L. Margheriti, D. Chiappe, P. Graziosi, B. Cortigiani, V. Lanzilotto, F. B. de Mongeot, P. Ohresser, E. Otero, F. Choueikani, P. Sainctavit, I. Bergenti, V. A. Dediu, M. Mannini, and R. Sessoli, "Magnetism of TbPc2 SMMs on ferromagnetic electrodes used in organic spintronics," *Chemical Communications*, 2013.

[95] T. G. Gopakumar, F. Matino, H. Naggert, A. Bannwarth, F. Tuczek, and R. Berndt, "Electron-Induced Spin Crossover of Single Molecules in a Bilayer on Gold," *Angewandte Chemie-International Edition*, vol. 51, pp. 6262–6266, 2012.

[96] T. Miyamachi, M. Gruber, V. Davesne, M. Bowen, S. Boukari, L. Joly, F. Scheurer, G. Rogez, T. K. Yamada, P. Ohresser, E. Beaurepaire, and W. Wulfhekel, "Robust spin crossover and memristance across a single molecule," *Nature Communications*, vol. 3, pp. 938–6, 2012.

[97] B. Warner, J. C. Oberg, T. G. Gill, F. el Hallak, C. F. Hirjibehedin, M. Serri, S. Heutz, M.-A. Arrio, P. Sainctavit, M. Mannini, G. Poneti, R. Sessoli, and P. Rosa, "Temperature- and Light-Induced Spin Crossover Observed by X-ray Spectroscopy on Isolated Fe(II) Complexes on Gold," *The Journal of Physical Chemistry Letters*, pp. 1546–1552, 2013.

[98] J.-F. Létard, "Photomagnetism of iron (II) spin crossover complexes—the T (LIESST) approach," *Journal of Materials Chemistry*, vol. 16, no. 26, pp. 2550–2559, 2006.

[99] T. Palamarciuc, J. C. Oberg, F. el Hallak, C. F. Hirjibehedin, M. Serri, S. Heutz, J.-F. Létard, and P. Rosa, "Spin crossover materials evaporated under clean high vacuum and ultra-high vacuum conditions: from thin films to single molecules," *Journal of Materials Chemistry*, vol. 22, no. 19, p. 9690, 2012.

[100] A. Nitzan, M. A. Ratner "Electron Transport in Molecular Wire Junctions," *Science*, vol. 300, pp. 1384–1389, 2003.

[101] J. Parks, A. Champagne, G. Hutchison, S. Flores-Torres, H. Abruña, and D. Ralph, "Tuning the Kondo Effect with a Mechanically Controllable Break Junction," *Physical Review Letters*, vol. 99, 2007.

[102] L. Yu, Z. Keane, J. Ciszek, L. Cheng, M. Stewart, J. Tour, and D. Natelson, "Inelastic Electron Tunneling via Molecular Vibrations in Single-Molecule Transistors," *Physical Review Letters*, vol. 93, 2004.

[103] W. Liang, M. P. Shores, M. Bockrath, J. R. Long, and H. Park, "Kondo resonance in a single-molecule transistor," *Nature*, vol. 417, no. 6890, pp. 725–729, 2002.

[104] J. J. Parks, A. R. Champagne, T. A. Costi, W. W. Shum, A. N. Pasupathy, E. Neuscamman, S. Flores-Torres, P. S. Cornaglia, A. A. Aligia, C. A. Balseiro, G. K. L. Chan, H. D. Abruña, and D. C. Ralph, "Mechanical Control of Spin States in Spin-1 Molecules and the Underscreened Kondo Effect," *Science*, vol. 328, pp. 1370–1373, 2010.

[105] E. A. Osorio, K. Moth-Poulsen, H. S. J. van der Zant, J. Paaske, P. Hedegård, K. Flensberg, J. Bendix, and T. Bjørnholm, "Electrical Manipulation of Spin States in a Single Electrostatically Gated Transition-Metal Complex," *Nano Letters*, vol. 10, pp. 105–110, 2010.

[106] M.-H. Jo, J. E. Grose, K. Baheti, M. M. Deshmukh, J. J. Sokol, E. M. Rumberger, D. N. Hendrickson, J. R. Long, H. Park, and D. C. Ralph, "Signatures

of Molecular Magnetism in Single-Molecule Transport Spectroscopy," *Nano Letters*, vol. 6, pp. 2014–2020, 2006.

[107] H. Heersche, Z. de Groot, J. Folk, H. van der Zant, C. Romeike, M. Wegewijs, L. Zobbi, D. Barreca, E. Tondello, and A. Cornia, "Electron Transport through Single Mn12 Molecular Magnets," *Physical Review Letters*, vol. 96, p. 206801, 2006.

[108] A. Mugarza, N. Lorente, P. Ordejón, C. Krull, S. Stepanow, M. L. Bocquet, J. Fraxedas, G. Ceballos, and P. Gambardella, "Orbital specific chirality and homochiral self-assembly of achiral molecules induced by charge transfer and spontaneous symmetry breaking," *Physical Review Letters*, vol. 105, no. 11, p. 115702, 2010.

[109] S. W. Wu, G. V. Nazin, X. Chen, X. H. Qiu, and W. Ho, "Control of Relative Tunneling Rates in Single Molecule Bipolar Electron Transport," *Physical Review Letters*, vol. 93, p. 236802, 2004.

[110] F. M. Leibsle, C. Flipse, and A. W. Robinson, "Structure of the Cu 100-c (2) N surface: a scanning-tunneling-microscopy study," *Physical Review B*, vol. 47, no. 23, p. 15865, 1993.

[111] T. Parker, L. Wilson, and N. Condon, "Epitaxy controlled by self-assembled nanometer-scale structures," *Physical Review*, 1997.

[112] D. Écija, M. Trelka, C. Urban, P. de Mendoza, A. Echavarren, R. Otero, J. M. Gallego, and R. Miranda, "Templated growth of an ordered array of organic bidimensional mesopores," *Applied Physics Letters*, vol. 92, no. 22, p. 223117, 2008.

[113] B. Lu, T. Iimori, K. Sakamoto, K. Nakatsuji, F. Rosei, and F. Komori, "Fullerene on Nitrogen-Adsorbed Cu(001) Nanopatterned Surfaces: From Preferential Nucleation to Layer-by-Layer Growth," *Journal Of Physical Chemistry C*, vol. 112, pp. 10187–10192, 2008.

[114] T. Choi, C. D. Ruggiero, and J. A. Gupta, "Incommensurability and atomic structure of Cu2N/Cu(100): A scanning tunneling microscopy study," *Physical Review B*, vol. 78, p. 035430, 2008.

[115] M. Yamada, S.-y. Ohno, Y. Iwasaki, K. Yagyu, K. Nakatsuji, and F. Komori, "Boundaries between square-shaped, nitrogen-adsorbed islands on Cu(001): Two relief mechanisms of the stress induced by atomic adsorbates," *Surface Science*, vol. 604, pp. 1961–1971, 2010.

[116] M. Corso, W. Auwärter, M. Muntwiler, A. Tamai, T. Greber, and J. Osterwalder, "Boron nitride nanomesh," *Science*, vol. 303, no. 5655, pp. 217–220, 2004.

[117] H. Dil, J. Lobo-Checa, R. Laskowski, P. Blaha, S. Berner, J. Osterwalder, and T. Greber, "Surface Trapping of Atoms and Molecules with Dipole Rings," *Science*, vol. 319, pp. 1824–1826, 2008.

[118] G. de la Torre, C. G. Claessens, and T. s. Torres, "Phthalocyanines: old dyes, new materials. Putting color in nanotechnology," *Chemical Communications*, no. 20, p. 2000, 2007.

[119] N. Sekkat, H. v. d. Bergh, T. Nyokong, and N. Lange, "Like a Bolt from the Blue: Phthalocyanines in Biomedical Optics," *Molecules*, vol. 17, pp. 98–144, 2012.

[120] S. Schmaus, A. Bagrets, Y. Nahas, T. K. Yamada, A. Bork, M. Bowen, E. Beaurepaire, F. Evers, and W. Wulfhekel, "Giant magnetoresistance through a single molecule," *Nature Nanotechnology*, vol. 6, no. 3, pp. 185–189, 2011.

[121] M. Warner, S. Din, I. S. Tupitsyn, G. W. Morley, A. M. Stoneham, J. A. Gardener, Z. Wu, A. J. Fisher, S. Heutz, and C. W. Kay, "Potential for spin-based information processing in a thin-film molecular semiconductor," *Nature*,vol. 0, p.1, pp. 98–144 2013.

[122] P. Liljeroth, J. Repp, and G. Meyer, "Current-induced hydrogen tautomerization and conductance switching of naphthalocyanine molecules," *Science*, vol. 317, pp. 1203–1206, 2007.

[123] N. Ishikawa, M. Sugita, N. Tanaka, T. Ishikawa, S. Koshihara, and Y. Kaizu, "Upward temperature shift of the intrinsic phase lag of the magnetization of bis(phthalocyaninato)terbium by ligand oxidation creating an S = 1/2 spin," *Inorganic Chemistry*, vol. 43, pp. 5498–5500, 2004.

[124] J. K. Gimzewski, E. Stoll, and R. R. Schlittler, "Scanning tunneling microscopy of individual molecules of copper phthalocyanine adsorbed on polycrystalline silver surfaces," *Surface Science*, vol. 181, no. 1, pp. 267–277, 1987.

[125] Y. Wang, K. Wu, J. Kröger, and R. Berndt, "Review Article: Structures of phthalocyanine molecules on surfaces studied by STM," *AIP Advances*, vol. 2, no. 4, p. 041402, 2012.

[126] Z. Li, B. Li, J. Yang, and J. G. Hou, "Single-Molecule Chemistry of Metal Phthalocyanine on Noble Metal Surfaces," *Accounts of Chemical Research*, vol. 43, pp. 954–962, 2010.

[127] J. F. Kirner, W. Dow, and W. R. Scheidt, "Molecular stereochemistry of two intermediate-spin complexes. Iron (II) phthalocyanine and manganese (II) phthalocyanine," *Inorganic Chemistry*, vol. 15, no. 7, pp. 1685–1690, 1976.

[128] K. Katoh, T. Komeda, and M. Yamashita, "Surface morphologies, electronic structures, and Kondo effect of lanthanide (iii)-phthalocyanine molecules on Au (111) by using STM, STS and FET properties for next generation devices," *Dalton Transactions*, vol. 39, no. 20, pp. 4708–4723, 2010.

[129] M. Kuz'min, R. Hayn, and V. Oison, "Ab initio calculated XANES and XMCD spectra of Fe(II) phthalocyanine," *Physical Review B*, vol. 79, p. 024413, 2009.

[130] F. Roth, A. König, R. Kraus, M. Grobosch, T. Kroll, and M. Knupfer, "Probing the molecular orbitals of FePc near the chemical potential using electron energy-loss spectroscopy," *The European Physical Journal B*, vol. 74, pp. 339–344, 2010.

[131] M. D. Kuz'min, A. Savoyant, and R. Hayn, "Ligand field parameters and the ground state of Fe(II) phthalocyanine," *The Journal of Chemical Physics*, vol. 138, no. 24, p. 244308, 2013.

[132] A. Scarfato, S.-H. Chang, S. Kuck, J. Brede, G. Hoffmann, and R. Wiesendanger, "Scanning tunneling microscope study of iron(II) phthalocyanine growth on metals and insulating surfaces," *Surface Science*, vol. 602, pp. 677–683, 2008.

[133] A. Mugarza, R. Robles, C. Krull, R. Korytár, N. Lorente, and P. Gambardella, "Electronic and magnetic properties of molecule-metal interfaces: Transition-metal phthalocyanines adsorbed on Ag(100)," *Physical Review B*, vol. 85, 2012.

[134] B. W. Dale, "Spin State of Divalent Iron. I. Magnetic Properties of Phthalocyanine Iron (II)," *The Journal of Chemical Physics*, vol. 49, no. 8, p. 3441, 1968.

[135] M. Abel, S. Clair, O. Ourdjini, M. Mossoyan, and L. Porte, "Single Layer of Polymeric Fe-Phthalocyanine: An Organometallic Sheet on Metal and Thin Insulating Film," *Journal Of The American Chemical Society*, vol. 133, pp. 1203–1205, 2011.

[136] Z. H. Cheng, S. X. Du, N. Jiang, Y. Y. Zhang, W. Guo, W. A. Hofer, and H.-J. Gao, "High resolution scanning-tunneling-microscopy imaging of individual molecular orbitals by eliminating the effect of surface charge," *Surface Science*, vol. 605, pp. 415–418, 2011.

[137] T. G. Gopakumar, T. Brumme, J. Kröger, C. Toher, G. Cuniberti, and R. Berndt, "Coverage-Driven Electronic Decoupling of Fe-Phthalocyanine from a Ag(111) Substrate," *Journal Of Physical Chemistry C*, vol. 115, pp. 12173–12179, 2011.

[138] N. Ishikawa, M. Sugita, T. Ishikawa, S. Koshihara, and Y. Kaizu, "Mononuclear lanthanide complexes with a long magnetization relaxation time at high temperatures: A new category of magnets at the single-molecular level," *Journal Of Physical Chemistry B*, vol. 108, pp. 11265–11271, 2004.

[139] J. D. Rinehart and J. R. Long, "Exploiting single-ion anisotropy in the design of f-element single-molecule magnets," *Chemical Science*, vol. 2, no. 11, p. 2078, 2011.

[140] Y.-S. Fu, J. o. r. Schwobel, S.-W. Hla, A. Dilullo, G. Hoffmann, S. Klyatskaya, M. Ruben, and R. Wiesendanger, "Reversible Chiral Switching of Bis(phthalocyaninato) Terbium(III) on a Metal Surface.," *Nano Letters*, vol. 12, pp. 3931–3935, 2012.

[141] L. Vitali, S. Fabris, A. M. Conte, S. Brink, M. Ruben, S. Baroni, and K. Kern, "Electronic Structure of Surface-supported Bis(phthalocyaninato)

terbium(III) Single Molecular Magnets," *Nano Letters*, vol. 8, pp. 3364–3368, 2008.

[142] S. Fahrendorf, N. Atodiresei, C. Besson, and V. Caciuc, "Accessing 4f-states in single-molecule spintronics," *Nat. Commun.*, vol. 4, pp. 2425, 2013.

[143] P. Lippel, R. Wilson, M. Miller, C. Wöll, and S. Chiang, "High-resolution imaging of copper-phthalocyanine by scanning-tunneling microscopy," *Physical Review Letters*, vol. 62, no. 2, pp. 171–174, 1989.

[144] S.-H. Chang, S. Kuck, J. Brede, L. Lichtenstein, G. Hoffmann, and R. Wiesendanger, "Symmetry reduction of metal phthalocyanines on metals," *Physical Review B*, vol. 78, p. 233409, 2008.

[145] P. Wahl, L. Diekhöner, M. Schneider, L. Vitali, G. Wittich, and K. Kern, "Kondo Temperature of Magnetic Impurities at Surfaces," *Physical Review Letters*, vol. 93, p. 176603, 2004.

[146] C. D. Ruggiero, T. Choi, and J. A. Gupta, "Tunneling spectroscopy of ultrathin insulating films: CuN on Cu(100)," *Applied Physics Letters*, vol. 91, p. 253106, 2007.

[147] B. J. Albers, T. C. Schwendemann, M. Z. Baykara, N. Pilet, M. Liebmann, E. I. Altman, and U. D. Schwarz, "Three-dimensional imaging of short-range chemical forces with picometre resolution," *Nature Nanotechnology*, vol. 4, no. 5, pp. 307–310, 2009.

[148] F. J. Giessibl, "Atomic resolution on Si(111)-(77) by noncontact atomic force microscopy with a force sensor based on a quartz tuning fork," *Applied Physics Letters*, vol. 76, no. 11, p. 1470, 2000.

[149] F. Giessibl, "Forces and frequency shifts in atomic-resolution dynamic-force microscopy," *Physical Review B*, vol. 56, no. 24, p. 16010, 1997.

[150] T. G. Gill, "Copper Nitride: A Nanoscale Template for Magnetic Molecules," *Masters thesis*, pp. 1–52, 2013.

[151] M. Ternes, C. P. Lutz, C. F. Hirjibehedin, F. J. Giessibl, and A. J. Heinrich, "The force needed to move an atom on a surface," *Science*, vol. 319, pp. 1066–1069, Feb. 2008.

[152] K. Franke, G. Schulze, N. Henningsen, I. Fernández-Torrente, J. Pascual, S. Zarwell, K. Rück-Braun, M. Cobian, and N. Lorente, "Reducing the Molecule-Substrate Coupling in C60-Based Nanostructures by Molecular Interactions," *Physical Review Letters*, vol. 100, Jan. 2008.

[153] M. Gruyters, T. Pingel, T. G. Gopakumar, N. Néel, C. Schütt, F. Köhler, R. Herges, and R. Berndt, "Electronic Ground-State and Orbital Ordering of Iron Phthalocyanine on H/Si(111) Unraveled by Spatially Resolved Tunneling Spectroscopy," *Journal Of Physical Chemistry C*, vol. 116, pp. 20882–20886, 2012.

[154] J. C. Oberg, M. R. Calvo, F. Delgado, M. Moro-Lagares, D. Serrate, D. Jacob, J. Fernández-Rossier, and C. F. Hirjibehedin," *Nature Nano.*, vol. 9, pp. 64–68, 2013.

[155] S. Li, A. Yu, F. Toledo, Z. Han, H. Wang, H. Y. He, R. Wu, and W. Ho, "Rotational and Vibrational Excitations of a Hydrogen Molecule Trapped within a Nanocavity of Tunable Dimension," *Physical Review Letters*, vol. 111, p. 146102, 2013.

[156] F. D. Natterer, F. Patthey, and H. Brune, "Distinction of Nuclear Spin States with the Scanning Tunneling Microscope," *Physical Review Letters*, vol. 111, p. 175303, 2013.

[157] A. Mugarza, C. Krull, R. Robles, S. Stepanow, G. Ceballos, and P. Gambardella, "Spin coupling and relaxation inside molecule–metal contacts," *Nature Communications*, vol. 2, p. 490, 2011.

[158] C. Wäckerlin, K. Tarafder, D. Siewert, J. Girovsky, T. Hählen, C. Iacovita, A. Kleibert, F. Nolting, T. A. Jung, P. M. Oppeneer, and N. Ballav, "On-surface coordination chemistry of planar molecular spin systems: novel magnetochemical effects induced by axial ligands," *Chemical Science*, vol. 3, no. 11, p. 3154, 2012.

[159] S. L. Kawahara, J. Lagoute, V. Repain, C. Chacon, Y. Girard, S. Rousset, A. Smogunov, and C. Barreteau, "Large Magnetoresistance through a Single Molecule due to a Spin-Split Hybridized Orbital," *Nano Letters*, vol. 12, pp. 4558–4563, 2012.

[160] J. Chen, "Large On-Off Ratios and Negative Differential Resistance in a Molecular Electronic Device," *Science*, vol. 286, pp. 1550–1552, 1999.

[161] I. Fernández-Torrente, D. Kreikemeyer-Lorenzo, A. Stróżecka, K. Franke, and J. Pascual, "Gating the Charge State of Single Molecules by Local Electric Fields," *Physical Review Letters*, vol. 108, p. 036801, 2012.

[162] U. Ham and W. Ho, "Spin Splitting Unconstrained by Electron Pairing: The Spin-Vibronic States," *Physical Review Letters*, vol. 108, p. 106803, 2012.

[163] J. S. Moodera, L. R. Kinder, T. M. Wong, and R. Meservey, "Large magnetoresistance at room temperature in ferromagnetic thin film tunnel junctions," *Physical Review Letters*, vol. 74, no. 16, pp. 3273–3276, 1995.

[164] M. Urdampilleta, "Supramolecular spin valves," *Nature Materials*, vol. 10, pp. 502–506, 2011.

[165] I. Lyo and P. Avouris, "Negative differential resistance on the atomic scale: Implications for atomic scale devices," *Science*, vol. 245, no. 4924, pp. 1369–1371, 1989.

[166] L. Chen, Z. Hu, A. Zhao, B. Wang, Y. Luo, J. Yang, and J. G. Hou, "Mechanism for Negative Differential Resistance in Molecular Electronic Devices: Local Orbital Symmetry Matching," *Physical Review Letters*, vol. 99, Oct. 2007.

[167] Y. Xue, S. Datta, S. Hong, R. Reifenberger, J. Henderson, and C. Kubiak, "Negative differential resistance in the scanning-tunneling spectroscopy of organic molecules," *Physical Review B*, vol. 59, no. 12, pp. R7852–R7855, 1999.

[168] B. Wang, K. Wang, W. Lu, H. Wang, Z. Li, J. Yang, and J. G. Hou, "Effects of discrete energy levels on single-electron tunneling in coupled metal particles," *Applied Physics Letters*, vol. 82, no. 21, p. 3767, 2003.

[169] J. Gaudioso, L. J. Lauhon, and W. Ho, "Vibrationally Mediated Negative Differential Resistance in a Single Molecule," *Physical Review Letters*, vol. 85, p. 1918, 2000.

[170] M. Grobis, A. Wachowiak, R. Yamachika, and M. F. Crommie, "Tuning negative differential resistance in a molecular film," *Applied Physics Letters*, vol. 86, no. 20, p. 204102, 2005.

[171] X. Tu, G. Mikaelian, and W. Ho, "Controlling Single-Molecule Negative Differential Resistance in a Double-Barrier Tunnel Junction," *Physical Review Letters*, vol. 100, 2008.

[172] B. Heinrich, M. Rastei, D. J. Choi, T. Frederiksen, and L. Limot, "Engineering Negative Differential Conductance with the Cu(111) Surface State," *Physical Review Letters*, vol. 107, p. 246801, 2011.

[173] E. R. Brown, J. R. Soderstrom, C. D. Parker, L. J. Mahoney, K. M. Molvar, and T. C. McGill, "Oscillations up to 712 GHz in InAs/AlSb resonant-tunneling diodes," *Applied Physics Letters*, pp. 1–3, 1999.

[174] E. Ozbay and D. M. Bloom, "110-GHz monolithic resonant-tunneling-diode trigger circuit," *IEEE Electron Device Letters*, vol. 12, no. 9, pp. 480–482, 1991.

[175] G. Mikaelian, N. Ogawa, X. W. Tu, and W. Ho, "Atomic scale control of single molecule charging," *The Journal of Chemical Physics*, vol. 124, no. 13, p. 131101, 2006.

[176] J. Huang, K. Xu, S. Lei, H. Su, S. Yang, Q. Li, and J. Yang, "Iron-phthalocyanine molecular junction with high spin filter efficiency and negative differential resistance," *The Journal of Chemical Physics*, vol. 136, no. 6, p. 064707, 2012.

[177] H. Mizuta and T. Tanoue, *The Physics and Applications of Resonant Tunnelling Diodes*. Cambridge Studies in Semiconductor Physics and Microelectronic Engineering, Cambridge Univ Press, 1995.

[178] "Nobel Prize Chemistry 2001." Nobelprize.org. Nobel Media AB 2014.

[179] P. Seibt, "Investigating the interactions between a single-molecule magnet and a surface," *Masters thesis*, pp. 1–69, 2013.

[180] V. Madhavan, W. Chen, T. Jamneala, M. Crommie, and N. Wingreen, "Local spectroscopy of a Kondo impurity:Co on Au(111)," *Physical Review B*, vol. 64, p. 165412, 2001.

[181] J. Kügel, M. Karolak, J. Senkpiel, P.-J. Hsu, G. Sangiovanni, and M. Bode, "On the relevance of hybridization and filling of 3d orbitals for the Kondo effect in transition metal phthalocyanines," *Nano Letters*, vol. 14, p. 38953902, 2014.

[182] H. Prüser, M. Wenderoth, P. E. Dargel, A. Weismann, R. Peters, T. Pruschke, and R. G. Ulbrich, "Long-range Kondo signature of a single magnetic impurity," *Nature Physics*, vol. 7, pp. 203–206, Jan. 2011.

[183] A. Hewson, *The Kondo Problem to Heavy Fermions* . Cambridge University Press, 1993.

[184] G. Kresse and J. Furthmüller, "Efficient iterative schemes for ab initio total-energy calculations using a plane-wave basis set," *Physical Review B*, vol. 54, no. 16, p. 11169, 1996.

[185] G. Kresse and D. Joubert, "From ultrasoft pseudopotentials to the projector augmented-wave method," *Physical Review B*, vol. 59, no. 3, p. 1758, 1999.

[186] J. Klimeš, D. R. Bowler, and A. Michaelides, "Van der Waals density functionals applied to solids," *Physical Review B*, vol. 83, no. 19, p. 195131, 2011.

[187] S. L. Dudarev, G. A. Botton, S. Y. Savrasov, C. J. Humphreys, and A. P. Sutton, "Electron-energy-loss spectra and the structural stability of nickel oxide: An LSDA+ U study," *Physical Review B*, vol. 57, no. 3, p. 1505, 1998.

[188] M. Cococcioni and S. de Gironcoli, "Linear response approach to the calculation of the effective interaction parameters in the LDA+U method," *Physical Review B*, vol. 71, p. 035105, 2005.

[189] J. Bartolomé, F. Bartolomé, L. M. García, G. Filoti, T. Gredig, C. N. Colesniuc, I. K. Schuller, and J. C. Cezar, "Highly unquenched orbital moment in textured Fe-phthalocyanine thin films," *Physical Review B*, vol. 81, p. 195405, 2010.

[190] P. S. Miedema, S. Stepanow, P. Gambardella, and F. M. F. d. Groot, "2p x-ray absorption of iron-phthalocyanine," *Journal of Physics: Conference Series*, vol. 190, p. 012143, 2009.

[191] M. Haghighi and H. Homborg, "Darstellung und Eigenschaften von Bis (phthalocyaninato) lanthanaten und-ceraten," *Zeitschrift für Naturforschung. B, A journal of chemical sciences*, vol. 46, no. 12, pp. 1641–1649, 1991.